UNIVERSITÉ DU LUXEMBOURG

PhD-FSTM-2025-089
The Faculty of Science, Technology and Medicine

DISSERTATION

Defence held on 27/08/2025 in Luxembourg

to obtain the degree of

DOCTEUR DE L'UNIVERSITÉ DU LUXEMBOURG

EN *SCIENCES EXACTES ET NATURELLES*

by

Deniz Işınsu AVŞAR
Born on 6 May 1992 in Ankara, (Turkiye)

ENCODING INFORMATION AS UNOBTRUSIVE GRAPHICAL PATTERNS USING CHOLESTERIC SPHERICAL REFLECTORS: FROM OPTICAL AND MATERIALS CHALLENGES TO APPLICATION IN ROBOTICS

Dissertation defence committee

Dr. Jan P.F. Lagerwall, dissertation supervisor
Professor, Université du Luxembourg

Dr. Holger Voos, Chairman
Professor, Université du Luxembourg

Dr. Danqing Liu
Associate Professor, Eindhoven University of Technology

Dr. Irena Drevenšek-Olenik
Professor, University of Ljubljana

Dr. Mathew Schwartz
Associate Professor, New Jersey Institute of Technology

Acknowledgements

It may sound cliché, but the truth is, I genuinely do not know where to begin. This has been a chapter of my life unlike any other, a time filled with intensity, transformation, and growth. Over the past four years, I've experienced emotions in their rawest forms; it has been a journey marked by blood, sweat, tears, and relentless effort :). There were moments when I thought, "If I know anything, it's that I know nothing," and other times when I was comforted by the thought that "the larger the circle of what I know, the more it touches the unknown." I learned a great deal not just academically, but about myself. I struggled, evolved, and changed. Perhaps it is an unusual way to begin my "thanks", but one of the most important things I have learned is to thank myself. Thank you for not giving up. Thank you for having the courage to keep going, even in the darkness of uncertainty.

As someone coming from Turkiye, addressing my professor by their first name felt quite unfamiliar at first. However, beyond getting used to that, what I truly appreciate Jan is the way he chose not to act like a "boss" or distant authority figure, but rather treats the people in the group like teammates. Thank you for always being approachable, supportive, and willing to share your knowledge generously and enthusiastically to help us grow. Looking back, what I valued most in a supervisor went beyond academic success or project guidance. What truly mattered to me was open, honest communication, knowing that I could express concerns, even criticisms, and that you would truly listen, and that when you had feedback or criticism, it would come from a place of professional respect, not personal offense. Thank you for being a supervisor whose door I never hesitated to knock on.

As I approach the end of this journey, my heart is filled with gratitude. What I carry with me most are the people I met along the way, the support I received, the friendships I built, and the shared thoughts, feelings, and experiences that sustained me.

When I first arrived here, as an adult who had progressed in my academic journey and in my life, I never expected to make so many close friends, especially with people from such different languages and cultures. I am deeply grateful to my entire lab group and to all current and former ESMP members with whom my path crossed. Your friendship,

generosity, support, and solidarity made my time here truly unforgettable. With many of you, what started as collaboration became real friendship. From the very beginning, I was lucky to share my office with Manos and Hakam, I remember that time with a smile. Hakam boss, every group needs a cool person like you with positive energy and no stress! Rijeesh, thank you for all the parties, dinners, cold walks back to Belval, great conversations, and constant support. You were always there for me when I needed someone. To my fellow travelers on this journey, my “dobbies”, Xu and Najiya: you are my true support system. Without you, I’m sure my rollercoaster PhD ride would have derailed entirely. Yansoong, my kebab boss, thank you for all your help, and for patiently answering my never-ending questions at all hours. Yong, you taught me so much when I first joined, many thanks for your patience and kindness. Zory, thank you for always being present, running the show behind the scenes, and doing it all with warmth and care. Yosuke, my former office mate, you’re always hilarious and seeing you always lifts my mood! Larry, thank you for being the ultimate culture coordinator. And Alejandro, we met only in my final year when you joined the group, but you somehow arrived exactly at the right moment. Even though we met late, it felt as if you had been part of my PhD journey all along. During the most intense period of my thesis, you helped me precisely where I needed it the most. Your kindness, knowledge, and engineering mindset were invaluable, and thanks to you I managed to complete my final chapter! You truly deserve a heartfelt thank you, and thank you as well for being such a fun and supportive officemate.

To Katrino and Tabea, how we connected so deeply in such a short time, I will never know but I’m so glad we did. Alba, Andrea, and Ricardo: my dear friends, you brought life and fun into this campus and this country. You became more than friends, you became ”dost” to me. Finding all of you, here, at this point in my life, feels like a miracle! Thank you for your love and endless support. My Najiya, the best flatmate and little sister, we’ve been through so much, thank you for everything! Majdi, one of my first friends here, you’ll always be my habibi. Ali, my project partner, thank you for being such an amazing teammate and a friend. I don’t know how I would’ve made it through without your calm, clear-headed presence.

To my committee members, Holger, Danqing, and Mat: thank you for your thoughtful feedback and support throughout this journey. Danqing, thank you for hosting me in your lab, generously sharing your facilities, and making me feel welcomed. To the whole Eindhoven team, thank you for embracing me with open arms and making me feel like one of your own. Special thanks to Elif, Umut, Duygu, Alex, and Ruth: you almost made me forget I had another lab elsewhere! Mat, thank you for hosting us in the US, patiently walking me through Fusion360, and bringing so much agility and energy to this project.

I would also like to thank the Institute for Advanced Studies (IAS) for funding this research. And special thanks to Sylvie, thank you especially for your constant smile, kindness, incredible organizations, and the motivation you brought me everytime we connected. You truly felt like part of our team. Uli and Bob, thank you both for your technical support, but even more so for your patience and generosity. You always make things work in the best possible way, and for that I am so grateful.

To my dear friends from METU, Ankara (each of you on your own PhD journey), you are my chosen family. Friends like you are rare, and the way we continue to support each other across distance and time is something I cherish deeply. Science may not have always been my friend, but you were. Aslı, Selin, Elif, Ceren, Özge, and Burak: you're one of a kind! To my amazing friends Ozan and Sevgi, thank you for opening your home to me during my Eindhoven stay, and for your endless support in life. To my inner circle: Tutku, Deniz, Cansu, and Duygu, thank you for sharing in every moment, every low, every joy in this life. I love you more than words can say, and I am so lucky to have you by my side always. To my Luxembourg family, Julia and Anya, thank you for your unwavering support and for being my personal therapists. I'm so happy to have found you, and so sorry for all the emotional roller coasters I ragged you through. To all my friends: thank you for waiting patiently for me to come back to life.

To my beloved family, I know you jave waited patiently (and perhaps desperately :D) for me to "finally" finish my education and find that legendary *green elixir*. If I have become someone you can be proud of, then I have succeeded. I came so far in this academic journey thanks to

your support. Words will never be enough to describe your unconditional love and support. And my beloved one, Ahmet, thank you for being my partner in life, love, and hope. You held my hand through the tears, the joy, the chaos of this journey. Thank you for softening my stress and panic and being my calming shelter. I'm so grateful it's you.

Table of Contents

Chapter 1

Overview of the thesis

The starting point of this research lies in the unique optical properties of Cholesteric Spherical Reflectors (CSRs), particularly their ability to selectively reflect light at specific wavelengths, including those beyond the visible light spectrum, such as ultraviolet (UV) and infrared (IR) regions. This wavelength selectivity offers exciting opportunities to develop fiducial markers [1] that are effectively invisible to the human eye but detectable by machines. The possibility of creating such invisible tags, for example, on transparent surfaces like glass or windows—one of the major challenges in robotics—motivated the initiation of this project.

To harness the full potential of CSRs, especially those based on polymerized liquid crystal shells, it was necessary to first optimize their optical performance in the visible spectrum. Several technical challenges emerged: how to maximize the reflection intensity from micron-scale spherical particles while minimizing light scattering, how to arrange them as close-packed arrays, and how to develop scalable and automated fabrication methods that ensure robust and stable CSR-based patterns on a variety of surfaces.

Initially, standard strategies such as embedding CSRs in index-matching binders were pursued to enhance reflection. However, this raised new questions about the suitability of such binders for UV and IR applications and about the availability of compatible illumination and imaging systems. Central to the detection mechanism is the circular polarization selectivity

[1] QR-code-like binary rectangular patterns commonly used in robotics .

of CSRs, a property derived from their internal helical structure that enables them to reflect circularly polarized light with a specific handedness. This unique optical signature allows for precise, machine-readable detection, but it also demands specialized, cost-effective, and lightweight imaging tools adaptable to both visible and invisible spectral ranges.

This study, therefore, sits at the intersection of materials science, optics, robotics, and engineering. It addresses not only the fundamental physics of cholesteric reflection but also the practical considerations of material formulation, patterning, optical readout, and system integration. By overcoming these multidisciplinary challenges, the work aims to bring CSRs closer to real-world applications, from creating vivid, tunable structural colors to enabling robust, covert fiducial markers for advanced robotic sensing.

Chapter 2

Background

2.1 Liquid Crystals

Liquid crystals (LCs) are unique phases that combine some properties of their neighboring phases: isotropic liquids and crystalline solids. LCs exhibit fluidity like liquids and at the same time exhibit long-range orientational order, meaning their constituent molecules tend to align along a preferred direction over macroscopic distances. This unique intermediate behavior gives rise to anisotropic properties: LCs can respond to external stimuli such as light, mechanical stress, electric, or magnetic fields, depending on the direction in which the stimulus is applied [1].

The term ”liquid crystal” refers to a phase formed by many molecules collectively, just as a liquid or solid phase composed of many molecules rather than individual ones. The molecules that generate LC phases are called *mesogens*, referring to their ability to form mesophases (intermediate state). Mesogens are typically organic compounds anisotropic in shape, most commonly rod-like (calamitic) or disc-like (discotic), with a rigid core often connected to flexible side chains [2]. LCs are classified as *thermotropic* if the liquid crystalline behavior occurs within a certain temperature range [3]. Another main class, known as *lyotropic* LCs, is formed by aggregate suspension of amphiphilic molecules[1] or nanoparticles in a solvent (typically aqueous), with concentration determining the range of LC order they exhibit. There

[1] Molecules having both hydrophobic (water-repelling) and hydrophilic (water-loving) regions.

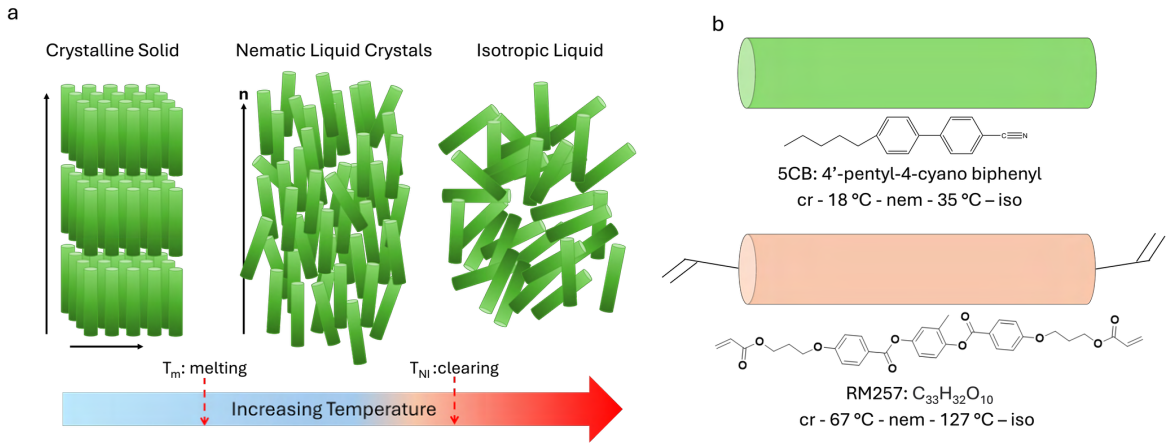

Figure 2.1: Schematic representation of (a) temperature-dependent phase transitions, observed in thermotropic liquid crystals, from crystalline solid to isotropic liquid with nematic liquid crystal phase in between. In the solid state, molecules are arranged in a fixed, orderly lattice, giving the material an orientational and a positional order. In the liquid state, molecules move freely with a disordered arrangement, allowing the material to flow and conform to the shape of its container. The liquid crystaline phase is shown as an intermediate state, combining fluidity with long-range molecular order. (b) Chemical structures of two common mesogens given along with the temperature range within they exhibit LC behavior: 4-pentyl-4'-cyanobiphenyl (5CB) as an example of a non-reactive mesogen, and RM257 as a representative reactive mesogen.

are many subclasses of liquid crystals with very different properties. In the scope of this thesis, I have only studied thermotropic LCs, specifically the chiral nematic (cholesteric) phase, which I will be describing in detail in the following sections.

In thermotropic LCs, the fact that temperature is the fundamental parameter controlling phase behavior brings two transition temperatures to define: the temperature determining the onset of LC order and the one at which this order disappears. As temperature increases, a crystalline solid melts into an LC phase at the *melting point* (T_m). Upon further heating, the system reaches the *clearing point* (T_c or T_{NI}), where orientational order is lost and the material becomes a conventional isotropic liquid. Figure 2.1a provides a simplified illustration of the temperature-dependent phase transitions observed in thermotropic LCs. While several LC phases can exist between the crystalline and isotropic states, only the nematic phase is shown here for simplicity. Figure 2.1b shows two common examples of compounds

that exhibit nematic behavior within specific temperature ranges together with their chemical structures: 4-pentyl-4'-cyanobiphenyl (5CB), a non-reactive mesogen, and RM257, a reactive mesogen that can be polymerized under UV light.

2.1.1 The Nematic Phase

The simplest and most widely studied thermotropic LC phase is the nematic phase. Among all LC phases, it is the least ordered where the mesogenic molecules have no long-range positional order of their center of mass but maintain long-range orientational order, aligning, on average, along a common direction described by the *director*, denoted **n**. Despite, as in this molecular perspective, the director defines the average orientation, individual molecules rarely align perfectly along **n** due to the thermal fluctuations. The director concept itself belongs to a continuum model. The director represents the principal symmetry axis, which may vary in space, forming a spatially dependent director field, **n(r)**, where **r** is the space coordinate. Importantly, the system is invariant upon rotation of **n**, meaning **n** and **-n** are physically indistinguishable, thus the director is a signless pseudo-vector [4].

The orientation of the director at an interface is determined by the surface conditions, a concept known as *surface alignment* or *anchoring*. Depending on the surface treatment or chemical properties, the director can typically adopt two different orientations relative to the interface. When the director aligns parallel to the substrate surface, this configuration is called *planar (tangential)* alignment, whereas when it orients perpendicular to the surface, it is referred to as *homeotropic (normal)* alignment. These boundary conditions strongly influence the optical and electro-optic behavior of LC devices and are essential for understanding director configurations under applied electric fields, as discussed later in this thesis. In practice, surface alignment can be controlled by applying specific surface coatings or treatments. For example, an aqueous solution of poly(vinyl alcohol) (PVA) promotes planar alignment, resulting in a tangential orientation of the director at the surface. In spherical geometries in the case of chiral nematics, this type of anchoring leads to a radial helix configuration, which is particularly relevant for the CSRs discussed later in this thesis.

The Orientational Order Parameter

The long-range orientational order is quantified by the *nematic order parameter, S*. This scalar parameter provides a measure of how well the mesogens are aligned along the director, being zero for complete random orientation, as found in isotropic phase and one for the perfect alignment along **n**, as in an idealized crystalline state [5]. *S* is defined by the following equation:

$$S = \frac{1}{2}\langle 3\cos^2\theta - 1\rangle \tag{2.1}$$

where the brackets represent an ensemble average in three dimensional space and θ is the angle defining the deviation in orientation from **n** as shown in Figure 2.2.

The value of S varies in the range $[-\frac{1}{2}\ ,\ 1]$. For most nematic liquid crystals at room temperature, S typically falls within the range of 0.4 to 0.6, reflecting a partially ordered but still highly anisotropic state [6, 7]. The negative lower limit, $-1/2$, represents the state where molecules are predominantly aligned orthogonal to the director and it is rare to find materials with negative order parameter [8, 9].

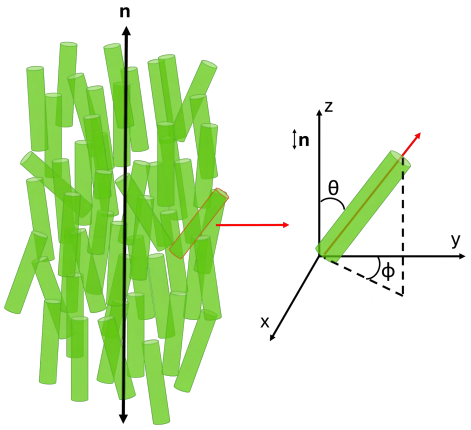

Figure 2.2: (Left) Schematic illustration of rod-like mesogens in a nematic LC phase, showing the average alignment along the director and (right) a single mesogen representation in the coordinate system, where its orientation deviates from **n** with angle θ in a direction ϕ. While ϕ does not appear in Equation 2.1, the bracket accounts for it through the ensemble average over three dimensions.

2.1.2 Cholesteric (Chiral Nematic) Liquid Crystals

Cholesteric liquid crystals (CLCs), also known as chiral nematics, represent a special case of the nematic phase where chirality is introduced into the system. The name “cholesteric” originates from early observations of this phase in derivatives of cholesterol [5]. Cholesteric phases are formed either by adding chiral dopants into an achiral nematic host or through inherently chiral mesogens.

Chirality is a property that defines an asymmetry of objects that cannot be superimposed onto their mirror image by any combination of rotations or translations. Geometries like spheres or cylinders are not chiral because they are identical to their mirror images. In contrast, a human hand, as a common example, is chiral: a right hand and a left hand are mirror images of each other but they are not identical. This difference brings the concept of handedness, a defining feature of chiral objects [7]. Until this section, I introduced non-chiral nematic phase which has a plane of mirror symmetry, director plane. However, when chirality is introduced the situation changes. The presence of chirality breaks mirror symmetry in the system, and the director **n** begins to rotate continuously in space, forming a twisted modulation.

This twist develops along an axis **m**, which is always orthogonal to the local director **n**. The resulting structure is periodic along **m**, and the periodicity is called the pitch length, denoted *p*. It is very common to resemble this twisted modulation of the director field to helical structures such as a spring or a screw winding. In fact, if one follow **n** in the so-called helically modulated cholesteric phase, one can never move up or down the helix, unlike the case for following the thread of the spiral. That said, for the sake of simplicity and consistency with common usage in the literature, I will use the expressions like the ’cholesteric helix’ and ’helix axis’ in this thesis. With **m** defined along $\hat{z}$, the director field of a CLC can be mathematically described as:

$$\mathbf{n}(z) = \left(\cos\left(\frac{2\pi z}{p}\right), \sin\left(\frac{2\pi z}{p}\right), 0\right) \tag{2.2}$$

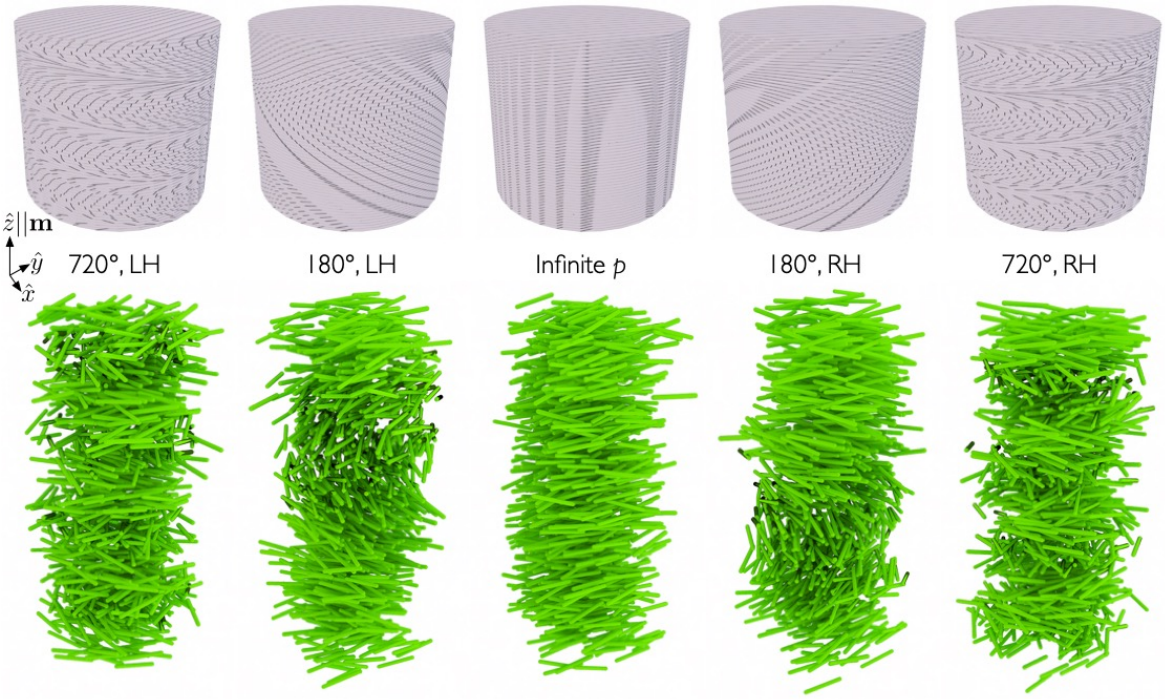

Figure 2.3: Schematic illustration of cholesteric liquid crystal phases that summarizes the structures, from left-handed tight twist on the left, gradually increasing to infinite pitch in the middle (representing the non-chiral nematic phase), to right-handed tight twist on the right. Top row represents a continuous director field, **n(r)**, picture and the bottom row is a molecular-scale representation. For clarity and simplicity, mesogenic molecules are considered as rigid rods. The z-axis represents the helical axis **m** around which the director twists. Figure prepared by Jan Lagerwall: used with permission.

This represents a right-handed twist [7, 10, 11]. For a left-handed twist, the sign of the second term is negative. At any given point along **m**, the director lies in the xy-plane and twists with constant pitch as one moves along $\hat{z}$.

It is important to remember that both the director and its twisted modulation are continuum concepts. Figure 2.3 illustrates the CLC phases from left-handed tight twist on the left to right-handed tight twist on the right. If p $\rightarrow \infty$ as pictured right in the middle, the cholesteric phase becomes indistinguishable from a conventional nematic, as the twist disappears. This continuous transition shows that a cholesteric phase is essentially a twisted version of the nematic phase. It is also critical to emphasize that the cholesteric phase lacks long-range

positional order, meaning that the molecules are not positioned as layers in space.

Although the full twist of the director occurs over a distance *p*, the effective periodicity of the structure is *p/2* due to the sign-invariant nature of the director **n**, meaning that $n = -n$. As a result, the director orientation repeats every half-pitch. The pitch in the structure depends on both the concentration and the twisting ability of the chiral dopant. The relationship is as follows:

$$p = \lim_{c \to 0} \frac{1}{[c] \cdot HTP} \tag{2.3}$$

where [c] is the concentration of a chiral dopant and HTP is the helical twisting power which quantifies the ability of the dopant to twist the achiral host. The value of HTP is different for different host-dopant pairs.

The periodic modulation in the cholesteric phase gives rise to distinctive optical properties. Combined with the birefringence, this periodicity allows cholesterics to selectively reflect circularly polarized light of a specific wavelength range. This optical behavior is a central focus of this thesis and is further discussed in detail in section 2.4.2.

2.1.3 Capturing Liquid Crystal Order in a Permanent Structure

The ability to freeze the order of liquid crystals into permanent structures is a powerful strategy for designing advanced functional materials that exhibit many of the unique properties of the LC phase, such as birefringence, selective Bragg reflection, and the ability to reflect circularly polarized light, etc., while combining with the mechanical stability of a solid. One effective method to preserve the molecular order of LCs in a solid polymer network is the photopolymerization of LC monomers. Figure 2.4 illustrates this process schematically. This process allows the alignment and anisotropic structure of an LC to be “locked” within a polymer network. Photopolymerization also helps to maintain the resulting shape in applications where LCs are confined in various geometries such as films, droplets, shells, fibers, etc. The major advantage is that photopolymerization proceeds rapidly (within seconds) such that it can prevent phase separation or phase transitions from occurring during curing.

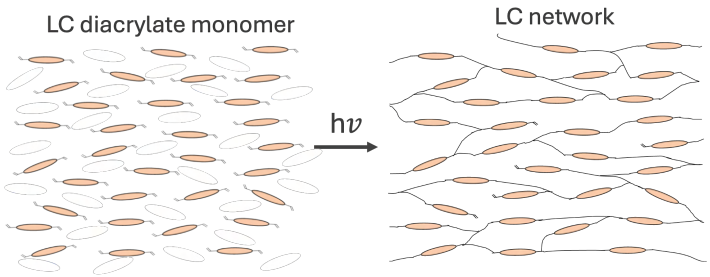

Figure 2.4: The photopolymerization of an LC network.

Typically, a mixture of LC monomers is used in the formation of an LC polymer network because a multi-component system allows tuning of physical properties such as the viscosity and the temperature window in which the system remains in the liquid crystalline phase. Reactive mesogens can be both mono- and di-functionalized and the ratio of these groups in the mixture directly affects the crosslinking density in the polymer network and thus the mechanical properties like glass transition temperature (T_g) and elasticity. The polymer precursor mixture also contains a photoinitiator, usually in low concentration (e.g. around 1 wt%) and responsive to the desired curing wavelength (typically UV or visible light), which generates free radicals to initiate photo-crosslinking. The wavelength and intensity of the light source should overlap with the absorption profile of the photoinitiator. For example, a common system containing 1 wt% Irgacure 651, can polymerize in seconds under 365 nm UV light with a light intensity of 5 mW/cm² [12]. While higher light intensities can increase the polymerization rate, care must be taken not to overheat the sample. Excessive temperatures can disrupt the LC order or cause a transition to the isotropic phase. It is crucial to obtain a homogeneous mixture before polymerization and this is achieved either by dissolving all components in a proper solvent such as tetrahydrofuran (THF), toluene, dichloromethane (DCM), etc. or by continuous stirring while heating to isotropic temperature. Proper alignment of the director is essential for achieving ordered polymer networks. A common approach to establish the alignment to produce polymerized LC films is using pre-treated substrates, e.g. glass slides coated with rubbed polyimide or polyvinyl alcohol (PVA) for planar orientation) [13].

Once the desired orientation is obtained, the precursor mixture is exposed to light to initiate photopolymerization. Oxygen inhibition is a common problem in free-radical (chain-growth) polymerization which is the case with acrylate-based LC mixture [14, 15]. To overcome this issue and ensure efficient and uniform curing, it is necessary to create an oxygen-free environment, which can typically be done by curing the material in an aqueous solution or placing it between pre-treated substrates, or most effectively by curing it under an inert atmosphere, such as a continuous flow of nitrogen while exposed to UV radiation.

2.2 What is Light? (Wave Picture of Light)

Light is one of the most fundamental and fascinating phenomena in nature. It plays a crucial role in our understanding of the universe and forms the basis of numerous technologies, from optical imaging to additive manufacturing. Light is a radiant energy that propagates in the form of waves, commonly defined as electromagnetic radiation [16]. Although the fact that light exhibits both wavelike and particle-like behavior, I will be focusing on the wave-like nature of light in the scope of this thesis, as this is most convenient for understanding its interaction with materials and optical phenomena such as reflection, refraction, polarization, and scattering, etc. In the following sections, I will give an overview of the nature of light and its fundamental properties. I will then continue with the interaction of light with different media, with particular emphasis on the principles that are relevant to the optical behavior of liquid crystalline materials.

2.2.1 Wavelike properties of light and electromagnetic spectrum

Light is a transverse wave composed of oscillating electric and magnetic fields, meaning that these oscillations are perpendicular to each other and to the direction of wave propagation. The fundamental properties that characterize a wave also apply to light. Amplitude can be defined as the maximum displacement of a transverse wave in the direction perpendicular to the propagation direction or simply as the height of the peak. The higher the amplitude, the more energy the wave carries. In the case of light, the amplitude correlates to the light

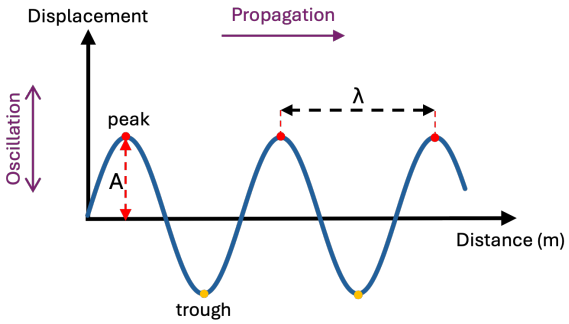

Figure 2.5: Transverse waves propagating from left to right and the oscillation directions are perpendicular and parallel, respectively, to the propagation direction.

intensity. One of the most well-known properties of waves is that they are periodic and the period in space is known as wavelength (λ). Wavelength is the length of one cycle of the wave, which is the distance between two successive peaks (or troughs)(see, Figure2.5). The time required for one wave cycle to pass a given point is called period (T). Frequency (f) describes the number of oscillations in a unit of time and is typically measured in Hertz (Hz), which is inverse seconds. Frequency and wavelength are inversely related and connected through the wave's speed (v) by the equation:

$$v = f \cdot \lambda \tag{2.4}$$

James Clerk Maxwell's equations provided the theoretical foundation for understanding these fields and showed that electromagnetic waves can travel through a vacuum at a finite speed, the speed of light, approximately $c = 3 \cdot 10^8$ meters per second (m/s). In vacuum, this relationship implies that as the wavelength increases, the frequency decreases, and vice versa. However, when light propagates through a material, the speed changes depending on the material's refractive index. In such cases, the frequency remains constant, while the wavelength adjusts to account for the change in speed [16, 17]. Electromagnetic radiation comes in a broad range of wavelengths and frequencies, although in vacuum all travel at the same speed. The electromagnetic spectrum contains the entire range of electromagnetic radia-

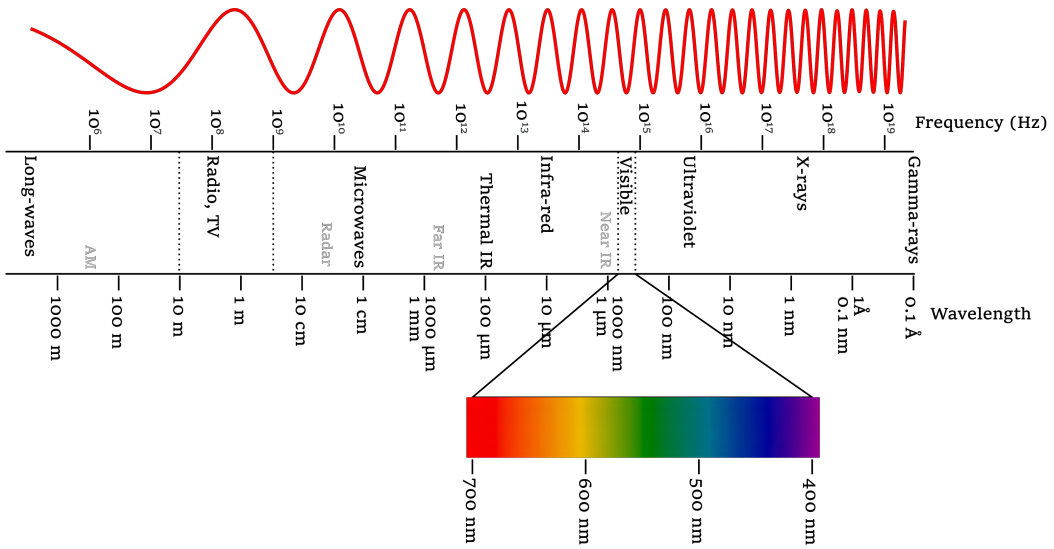

Figure 2.6: The electromagnetic spectrum. Adapted from Wikimedia Commons under CC-BY-SA 4.0 [18].

tion, organized by wavelength or frequency. It spans from short-wavelength, high-frequency gamma rays and X-rays, through ultraviolet (UV), visible light, and infrared (IR), to long-wavelength, low-frequency microwaves and radio waves. Visible light, which lies in a narrow band of this spectrum (approximately 400–700 nm), is the portion that our eyes can detect, with shorter wavelengths perceived as violet and longer ones as red.

2.2.2 The Polarization of Light

One of the fundamental properties of light is polarization, that is the orientation of the electric field vector as the wave propagates. In unpolarized light, such as sunlight or light from a typical bulb, the electric field oscillates randomly in all directions perpendicular to the direction of propagation. In contrast, polarized light has a well-defined orientation of the electric field.

Any state of polarized light can be described within the framework of elliptical polarization, where the tip of the electric field vector traces an ellipse in the plane perpendicular to propagation. Two special cases of this general form are linear and circular polarization. In linear

polarization, the electric field oscillates in a fixed plane perpendicular to the direction of propagation, corresponding to zero ellipticity. In circular polarization, the electric field rotates in a helical pattern as the wave travels. For right-handed circular polarization, the electric field rotates clockwise when viewed along the direction of propagation; for left-handed circular polarization, it rotates counterclockwise [16, 17]. Understanding polarization is essential for interpreting how light behaves in reflection, transmission, and scattering, especially when dealing with anisotropic materials such as LCs.

In 1808, the French physicist Étienne Malus made a groundbreaking discovery when he observed that light reflected from nonmetallic surfaces becomes polarized. While studying sunlight reflected from windows of the Luxembourg Palace through a calcite crystal, he noticed that the intensity of the transmitted light changed as he rotated the crystal [16]. Since calcite naturally splits light into two rays that respond differently to polarized light, this change in intensity revealed that the reflected light was no longer randomly oscillates but polarized. This observation provided the first clear evidence that reflection can generate polarized light. François Arago, drawing conclusions from his own experiments, mistakenly believed that the reflected and refracted light were always equally polarized at any angle of incidence [16]. However, it was Brewster's experiments that first revealed the complexity of light polarization, showing that reflected light is not always fully polarized and that its degree of polarization depends on the angle at which light hits the surface. He found that light becomes most polarized at a specific angle, now known as the Brewster angle [17].

In this context, it is useful to define the polarization components relative to the **plane of incidence**, which is the plane formed by the incoming light ray and the surface normal. If the electric field oscillates perpendicular to the plane of incidence, light is called s-polarized (senkrecht, a German word meaning perpendicular). And, if the electric field oscillates within the plane of incidence, it is p-polarized (parallel) [17].These definitions become particularly important when analyzing reflection and transmission using Fresnel's equations, as the reflectance and transmittance differ significantly for s- and p-polarized light, especially near the Brewster angle (further discussed in Chapter 6).

2.3 The Propagation of Light in Isotropic Media

When light encounters a boundary between two different media, several interactions may occur: it may be reflected, refracted, transmitted with or without absorption, and/or scattered. These interactions are governed by a set of physical laws and material properties that determine how much of the incident light is transmitted or reflected and how its direction and intensity change.

2.3.1 Reflection and Refraction

When light hits a surface, a portion of it is reflected back, meaning its direction of propagation undergoes a sudden change, into the original medium. This process is described by the law of reflection, which states that the angle of incidence is equal to the angle of reflection. These angles are measured with respect to the surface normal (the imaginary line perpendicular to the interface). In the case of smooth surfaces, this reflection is *specular*, meaning that incident parallel rays remain parallel after reflection. Specular reflection is in contrast to diffuse reflection, which occurs on rough surfaces where the reflected light is scattered in many directions.

The portion of light that is transmitted into the second medium undergoes refraction, which is the change in direction of the light that arises from the difference in the speed of light in the two media and is governed quantitatively by *Snell's Law*:

$$n_i \cdot \sin\theta_i = n_r \cdot \sin\theta_r \tag{2.5}$$

where n_i is the refractive index of the incident medium (usually air), n_r is the refractive index of the sample, θ_i is the incidence angle, and θ_r is the refracted angle.

The resulting deflection depends on the relative values of the refractive indices. The *refractive index* n of a medium is a dimensionless quantity that describes how light propagates through that medium. It is defined as the ratio of the speed of light in vacuum c to the phase

velocity v of light in the material:

$$n = \frac{c}{v}. \tag{2.6}$$

When light passes from a medium with a lower refractive index into one with a higher refractive index, its speed decreases, and the propagation direction shifts closer to the normal. Conversely, when light moves from a higher-index medium to a lower-index one, it speeds up and the propagation direction shifts away from the normal. An important consequence of this behavior arises when light attempts to move from a medium of higher refractive index to one of lower refractive index. In this scenario, there exists a *critical angle* beyond which no refracted light can emerge into the second medium. Instead, the incident light is entirely reflected back into the original medium, a phenomenon known as *total internal reflection*.

2.3.2 Mie scattering

Mie scattering describes the scattering of light by particles whose size is comparable to or larger than the wavelength of light. This phenomenon is relevant particularly when the particles are nearly spherical. The theoretical foundation for understanding how light scatters from spherical particles of comparable size to the wavelength of light was laid by Gustav Mie in 1908. His work remains foundational in optics, atmospheric science, and materials research.

Unlike Rayleigh scattering, which dominates when particles are much smaller than the wavelength of light and strongly scatters shorter (blue) wavelengths, Mie scattering does not have a wavelength dependence. Instead, it tends to scatter all visible wavelengths more uniformly, which is why white light remains white after being scattered by large particles. Moreover, Mie scattering is predominantly directed in the forward direction, especially as the particle size increases, and its intensity increases with particle size and refractive index contrast between the particle and the surrounding medium [19].

A well-known and relatable example of Mie scattering is the appearance of clouds and fog. The water droplets suspended in the atmosphere typically have diameters on the order of a few microns, similar to the wavelength of visible light, and are approximately spherical. As

a result, sunlight is scattered in many directions, making clouds and fog appear white. This scattering behavior is particularly relevant to the CLC shells studied in this thesis. These structures are spherical in shape and several microns in size, placing them firmly in the Mie scattering regime.

2.3.3 Transmission with Absorption (Beer-Lambert Law)

Not all transmitted light passes through a medium unaffected. Depending on the material properties and the wavelength of light, part of the incident light may be absorbed. Absorption occurs when photons interact with the electronic or vibrational states of the medium, transferring energy to the material and promoting electrons to higher energy levels. This process leads to a measurable decrease in the light's intensity as it travels through the absorbing medium.

The attenuation of light due to absorption is described quantitatively by the *Beer–Lambert Law*, which is widely used in optics and spectroscopy to relate the absorbance of light to the properties of the medium:

$$A = \epsilon \cdot c \cdot d \tag{2.7}$$

where A is the absorbance (a dimensionless quantity), ϵ ($L \cdot mol^{-1} \cdot cm^{-1}$) is the molar absorption coefficient (which depends on the absorbing species and the wavelength), c (mol/L) is the concentration of the absorbing species, and d (cm) is the optical path length through the medium.

This principle is essential for understanding how absorbing substances, such as dyes or pigments, affect the intensity and spectral composition of the incident light. In optical materials and thin films, absorption plays a key role in determining both color and optical functionality.

2.4 Light and Liquid Crystals (Light hitting anisotropic media)

2.4.1 Optical Anisotropy of LCs

LC phases are optically anisotropic materials originating from the long-range orientational order of anisometric mesogens. This means that unlike isotropic media where the optical properties are identical in all directions, the optical properties of LC depend on the direction of light propagation and polarization relative to the director **n**. The director defines the optic axis of the LC, and the refractive index measured along the optic axis **n** differs from the one measured perpendicular to the director. This directional dependence gives rise to birefringence, a measurable consequence of anisotropy, defined as the difference between the two principal refractive indices experienced by light striking the LC sample [4, 16, 20]:

$$\Delta n = n_e - n_o \tag{2.8}$$

These two indices define as the uniaxial optical indicatrix, represented as an ellipsoid of revolution (also called the index ellipsoid), where the long and short axes correspond to $n_{||}$ and $n_{\perp}$, respectively [21]. In typical nematic liquid crystals $n_{||} > n_{\perp}$, and such materials are referred to as optically positive. If $n_{||} < n_{\perp}$, the material is considered optically negative. When light propagates through a uniaxial anisotropic medium, such as an LC, at an arbitrary angle θ to the optic axis **n**, the incident light splits into two components: one polarized perpendicular to the optic axis and the other parallel to it. These are referred to as the ordinary and extraordinary rays, respectively. The ordinary ray (n_o) experiences a constant refractive index equal to $n_{\perp}$, regardless of its propagation direction. In contrast, the extraordinary ray (n_e) travels at a direction-dependent speed, experiencing a refractive index that depends on the angle θ between the propagation direction and the optic axis [20]. For uniaxial nematics, this variation is described by:

$$n_o = n_{\perp} \tag{2.9}$$

$$n_e = \frac{n_{||} n_{\perp}}{\sqrt{n_{||}^2 \cos^2\theta + n_{\perp}^2 \sin^2\theta}} \tag{2.10}$$

This expression reflects how n_e transitions between $n_{||}$ and $n_{\perp}$ depending on θ. When the light beam travels exactly along the optic axis (i.e., $\theta = 0$), both the ordinary and extraordinary components experience $n_{\perp}$, since light is a transverse wave and the electric field oscillates only in directions perpendicular to the propagation axis. Consequently, birefringence vanishes, and the material appears optically isotropic.

As a result of birefringence, the ordinary and extraordinary rays propagate at different velocities, causing a phase shift between them as they exit the LC material. This phase shift is called optical retardation (δ) and is defined as:

$$\delta = \frac{2\pi \cdot \Delta n \cdot d}{\lambda} \tag{2.11}$$

where *d* is the thickness of the sample, Δn is the birefringence and λ is the wavelength of light. The magnitude of Δn determines how strongly a piece of certain thickness of the material can manipulate the polarization and phase of transmitted light, which is essential for many optical applications.

This phase shift gives rise to the interference patterns and color changes often observed when anisotropic samples are viewed under polarized light. Polarized Optical Microscopy (POM) is a standard technique for observing liquid crystals. It uses two polarizers: a polarizer that polarizes the incoming light, and an analyzer, typically oriented at 90° to the polarizer, to analyze the polarization state. When an anisotropic LC sample is placed between crossed polarizers, as illustrated in Figure 2.7d, the birefringent nature alters the polarization state of the transmitted light, allowing part of it to pass through the analyzer. For instance, when the retardation corresponds to half the wavelength of light (a half-wave plate condition), the polarization remains linear but is mirrored with respect to the angle between the incident polarization and the optic axis.

The resulting image depends on the orientation of the director relative to the polarization direction of the incident light. Regions where the director is aligned parallel or perpendicular to either polarizer appear dark (extinction), because the birefringent sample does not

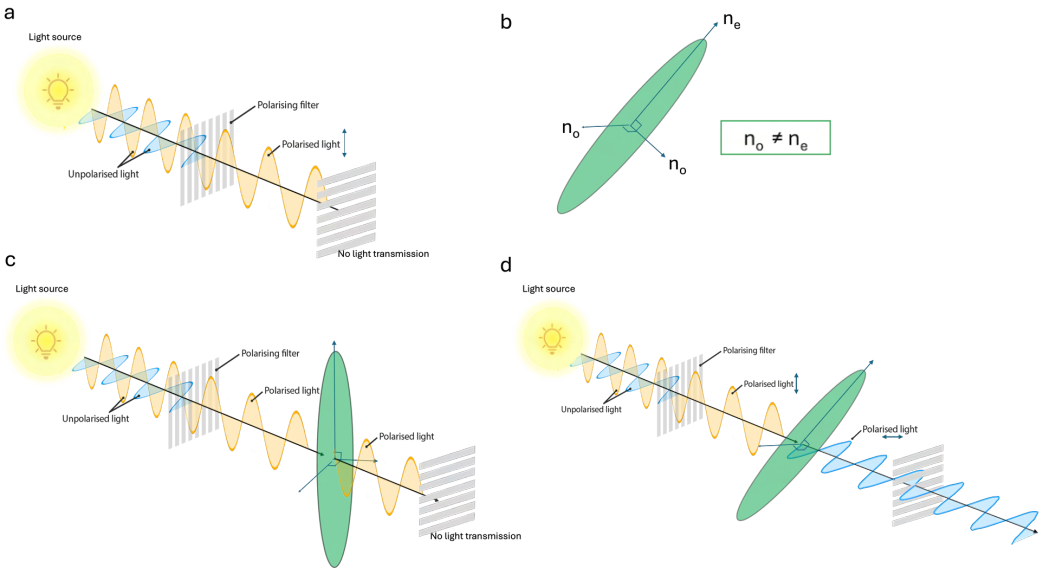

Figure 2.7: Schematic illustration showing (a) unpolarized light passing through the first polarizer, becoming linearly polarized but is blocked by the second polarizer (analyzer) placed at 90°, resulting in no light transmission. (b) A representative optical indicatrix with optic axis **n** and associated ordinary (n_o) and extraordinary (n_e) refractive indices. (c) When the optic axis is aligned parallel or perpendicular to one of the polarizers, the polarized light does not undergo any phase shift and is completely blocked by the analyzer. (d) When the optic axis is oriented at an angle different from 0 or 90° between the crossed polarizers, birefringence induces a phase shift between the ordinary and extraordinary rays. When the optical retardation equals half the wavelength, the birefringent medium acts as a half-wave plate ($\lambda/2$), mirroring the plane of polarization and allowing light to pass through the analyzer.

modify the polarization direction in these orientations, thus the analyzer, being crossed with the polarizer, completely blocks the light. In contrast, regions where the director is aligned at an angle to the polarizer introduce a phase difference between the ordinary and extraordinary components, changing the polarization state so that some light can pass through the analyzer, resulting in bright interference colors. These colors are often used qualitatively to assess LC alignment, defect structures, or sample uniformity.

2.4.2 The Selective Reflection in Cholesteric Liquid Crystals

The focus of everything discussed in this thesis is the remarkable optical feature of CLCs to selectively reflect light both in polarization and wavelength. But what exactly does it mean

that CLCs selectively reflect certain wavelengths of light? When the pitch of the cholesteric helix is on the order of visible wavelengths, the material appears in vivid, iridescent colors that are visible to the naked eye, especially when observed on a dark background. Moreover, the reflected color depends on both the pitch and the observation angle, often shifting toward shorter wavelengths (blue-shifting) when observed through tilted angles with respect to the sample normal, and the color can also vary with temperature and/or chiral dopant concentration due to changes in the pitch. The origin of these colors is selective reflection, where only a specific wavelength band of light is reflected.

This phenomenon arises from the periodic structure due to the helical modulation. This repeating structure enables us to apply a geometric approach similar to that used in X-

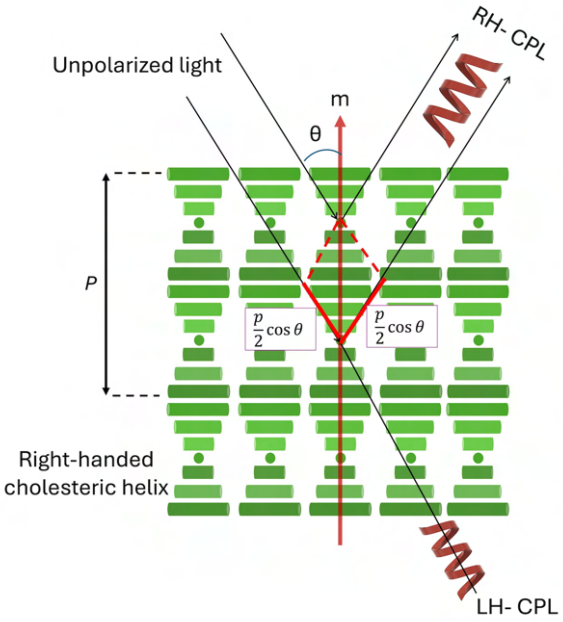

Figure 2.8: Schematic illustration of selective Bragg reflection in a cholesteric liquid crystal. The helical modulation of the director (represented by rods) leads to wavelength- and polarization-selective reflection. Depending on the pitch length *p*, and the refractive indices of the material, a cholesteric structure reflects circularly polarized light that matches the handedness of the helix within the selective reflection wavelength band, while allowing the opposite handedness to be transmitted. The angle of incidence further tunes the reflected wavelength, as described by Bragg's law.

ray diffraction from crystals, to determine a relationship between the reflected wavelength, periodicity and the viewing angle [22, 23, 24]. Figure 2.8 shows the schematic illustration of a cholesteric structure with its helical axis aligned vertically and the unpolarized light incident at an angle θ. When light hits the CLC, the effective refractive index experienced by it varies periodically, creating a structure analogous to a 1D photonic crystal, with the periodicity *p/2*, due to the 180° symmetry of the director field.

According to the law of reflection, the angle of incidence is equal the angle of reflection. It is emphasized by red lines in Figure 2.8 that the lower ray travels a longer distance than the upper one, with the path difference of *2·p/2·*cosθ. Constructive interference occurs when this optical path difference equals an integer number of the reflected wavelength, resulting in the Bragg condition [25, 26]:

$$\lambda = \bar{n} \cdot P \cdot \cos\theta \tag{2.12}$$

where λ is the reflected wavelength, $\bar{n}$ is the average refractive index of the CLC, and θ is the angle of incident light.In contrast to the conventional Bragg equation, derived for discrete atomic crystals, the cholesteric diffraction equation 2.12 does not contain any higher orders. This reflects the fact that the twisted structure is perfectly described by a single sine function, without any higher harmonics, hence no higher order diffraction is generated.

At normal incidence, i.e., light propagating directly along the helix axis), the center of the reflection band, λ_0 is given by:

$$\lambda_0 = \bar{n} \cdot P \tag{2.13}$$

The width of the reflection band is governed by the birefringence Δn of the material:

$$\Delta\lambda = P \cdot \Delta n \tag{2.14}$$

Observation of selective reflection depends critically on the orientation of the helix relative to the incident light. If the helix axis **m** lies entirely within the sample plane, light incident perpendicular to the plane will not encounter periodic modulation along its path, and no

reflection is observed. In contrast, when **m** is aligned with the direction of light propagation, the periodic structure effectively filters out a specific circular polarization band.

2.5 Color Creation Mechanisms (pigment coloration and structural coloring)

We humans often define beauty in colors; the azure of the sky, the deep navy blue of the oceans, the orange-red hues of sunrise and sunset, the colorful flowers that bloom everywhere with the arrival of spring... Colors have also been one of the ways of self-expression and communication for centuries, in art, fashion, and even politics. Colors play a significant role not only for humans but also for all living beings in making sense of the world and carrying out biologically essential activities, such as protection against predators, camouflage, mate selection, and social signaling, etc.

Ever since I was a child, I have been haunted by a simple but profound question about colors: What if the color I see isn't the same as what someone else sees? What if I have always called a color "blue" just because that's what I was taught, even though the experience of that color could be different for someone else? Could my blue be someone else's yellow? Although this is a deep topic related to both perception and philosophy, a clearer understanding begins with the physical principles of how color is created. From a material science perspective, understanding how color is generated and perceived is also critical for designing advanced optical systems and functional surfaces. Coloration in nature mostly arises from the physical interaction between light (absorption, reflection, and scattering) and micro- and nanosize structures. Here, I will explain the two main mechanisms of color generation: pigmentary and structural coloration.

Pigmentary colors arise from the selective absorption of specific wavelengths of light by the electrons of pigments or dyes [2]. When the incident light strikes a pigment molecule or particle, electrons are excited to a higher energy state as a result of energy exchange

[2] Dyes are organic and pigments are inorganic absorbers.

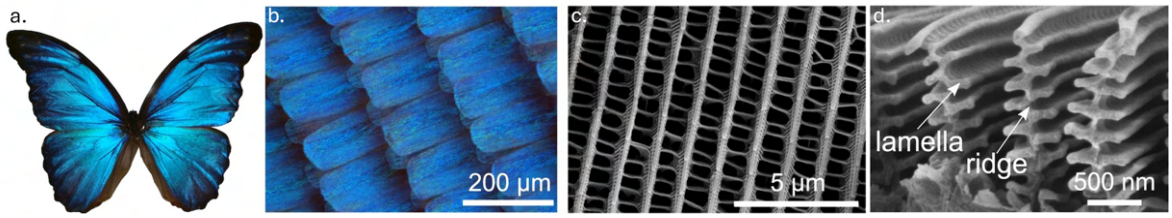

Figure 2.9: (a) Morpho didius butterfly exhibiting its characteristic blue structural coloration. (b) Close-up view of the wing scales. (c) Scanning electron microscope (SEM) image showing the top view of the parallel ridges on a single scale. (d) SEM cross-section of these ridges, revealing their layered 'Christmas tree'-like architecture composed of alternating lamellae of air and cuticle. Reprinted with permission from [28].

between the light and electrons. Thus, the selective wavelengths of light are absorbed while others are reflected or transmitted, and coloration is achieved [27]. In contrast, structural colors originate from the interaction of light with periodic micro- or nanostructures. These colors result from physical interaction of light such as interference, diffraction, and scattering, rather than absorption. Because the structural colors do not rely on electronic transitions, they are typically more efficient without an energy loss in the use of light. Moreover, the structural colors do not fade over time like pigments as long as the periodic structures exist. The brightest and most distinctive colors in nature are structural colors.

Over billions of years of evolution, fascinating microstructures were revealed in various species such as jewel beetles, Morpho butterflies, hummingbirds, and marble berries that exhibit vivid structural colors. These colors arise from periodic structures with length scales comparable to the visible light wavelengths [29, 30, 31, 32]. Figure 2.9 displays the striking blue color of a Morpho didius butterfly, a common example of structural coloration, together with the scanning electron microscope (SEM) images of its periodic nanostructures. The wing scales of the Morpho butterfly consist of rows of ridges, each formed by a multilayer lamella-air structure resembling a "Christmas tree" from the cross-section. The vivid blue color results from constructive interference of blue wavelengths, while other wavelengths are either canceled out or transmitted through the wing [28, 29, 30].

2.6 Liquid Crystals Confined in Curved Geometry

Owing to their liquid nature, LCs can easily change shape and adapt to a variety of geometric confinements, including not only standard flat geometries but also curved ones. When LCs are confined within curved geometries, such as spheres, the director field must adapt to the curvature, leading to deformations in the orientational order and often the formation of topological defects. Although these distortions increase complexity, they also give rise to new and interesting material behaviors that do not appear in flat systems. Two common examples of LCs in spherical confinement are droplets and shells. A droplet is a spherical volume enclosed by a single surface, while shells consist of a thin spherical layer confined between two surfaces, like an orange peel sits between the air and the orange pulp.

There are several advantages to using shells in this study instead of beads that are made by polymerizing droplets. First, shells can be larger and still have good optical quality. This is because droplets always have a defect in their center, while shells, with tangential alignment on both the inner and outer surfaces, support a more uniform radial orientation of the director field [33]. Curved confinement amplifies the optical features of cholesterics while the ability to independently tune both surfaces of the shell offers precise control over the final properties [34]. Second, as will be explained in Chapter 3, the process of polymerization of shells followed by swelling in acetone can create a small hole in each shell [35]. These holes allow further processing and give each CSR shell a distinct identity that will be explained in the next subsection.

Because the shells are hollow, they use less liquid crystal material, which is another advantage. In terms of environmental impact, a recent study in our group has also shown that it is possible to create more sustainable CSR shells using materials like cellulose nanocrystals (CNCs) [36]. In contrast, droplets made from CNC suspensions tend to collapse when dried, ruining their shape and reflective properties [37].

In this section, I will first discuss the unique optical properties of CSRs and then move on to how we produce and observe them experimentally.

2.6.1 Optics of Curved Cholesterics

As previously introduced in section 2.4.2, cholesteric liquid crystals are extraordinary self-assembled photonic materials known for their ability to selectively reflect light in the ultraviolet, visible, or infrared spectrum. This optical response arises from their helical director field and enables selective Bragg reflection of circularly polarized light. The reflected wavelength is determined by the pitch (p) of the cholesteric helix, and the handedness of the helix (right- or left-handed) dictates the polarization of the reflected light. Even though the shells are thinner compared to the droplets, they are still thick enough, typically around 10-15 μm, to ensure effective selective Bragg reflection. Given that green retroreflecting CSRs have a pitch of approximately 0.35 μm, this corresponds to more than 25 pitch lengths across the shell thickness, which is already above the minimum of ten pitches required for selective reflection in CLCs [25]. In contrast to conventional flat cholesteric films, which exhibit angle-dependent reflection and behave as retroreflectors only along their normal axis, cholesteric spherical reflectors (CSRs) exhibit omnidirectional retroreflectivity. This means that CSRs reflect the same color with equal intensity regardless of the viewing direction [33]. Figure 2.10 illustrates three films of CLC showing red, green, and blue retroreflection when illuminated and viewed normal to the sample placed next to a sample with three wells containing closely packed CSRs, designed for the same respective colors. As we look with an angle, inclining the light source in the same way, the flat samples darken at oblique angles, while the CSRs maintain their equally strong retroreflective color at all angles, highlighting their angular independence. We note, however, that the CSR sample that looks red under ambient light looks white in retroreflection conditions. In Chapter 5, I will present a new method that allows CSRs to generate strong and saturated color both under ambient light and in retroreflection.

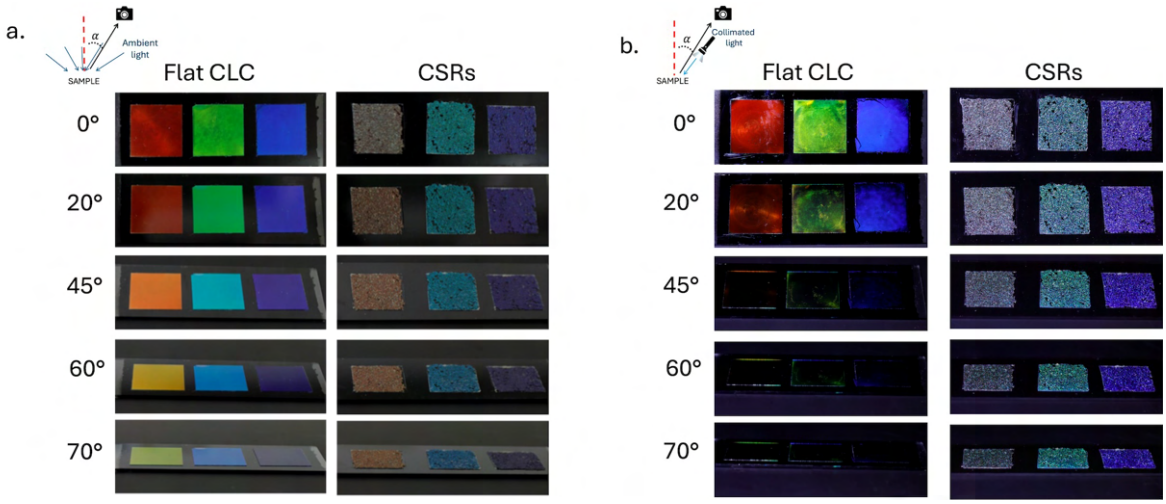

Figure 2.10: Comparison of reflection characteristics of flat cholesteric films and densely packed CSRs on a black background. Flat films of cholesteric liquid crystal with vertically aligned helices (in red, green, and blue retroreflection color) were compared with corresponding close-packed CSR samples embedded in NOA160 glue. Two white-light illumination conditions (a) diffuse ambient light on a cloudy day and (b) collimated light aligned with the viewing direction, as in the schematics above. For both conditions, five different viewing angles α are investigated without the use of polarizers. Reproduced from [33] on a CC-BY license.

A key feature of the cholesteric structure is its selective reflection of circularly polarized light. Because the helical director modulation of the molecules acts as a polarization-sensitive photonic mirror, CSRs only reflect circularly polarized light of the same handedness as their internal helix structure. For instance, a right-handed cholesteric shell reflects only right-handed circularly polarized light. This property can be directly visualized using circular polarizers: when observed through a left-handed polarizer, the CSR reflection disappears, whereas it remains visible through a right-handed one. This behavior is analogous to the operation of 3D cinema glasses, where each side transmits a different circular polarization to create stereoscopic depth, the 3D experience. Figure2.11 shows this polarization-selective reflection in CSRs through right- and left-handed circular polarizers.

Beyond their individual optical properties, CSRs also exhibit fascinating collective behavior when arranged into dense arrays. Recent studies have shown that the spherical geometry combined with Bragg reflection, enables photonic cross communication between CSRs. This

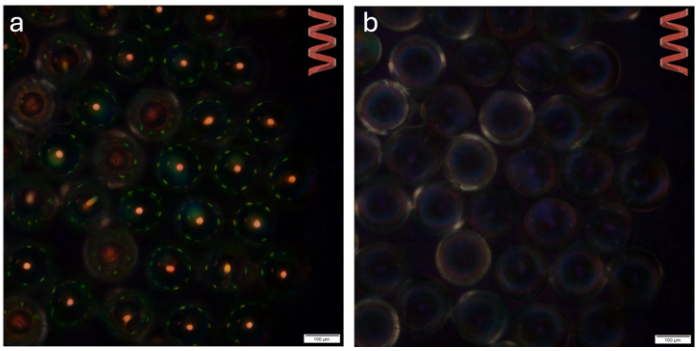

Figure 2.11: The microscope images showing the polarization-selective reflection of CSRs taken through left- and right-handed circular polarizers. Scale bars: 100μm.

phenomenon arises from light reflecting off one CSR and being redirected and hitting other neighboring CSRs, thus resulting in multicolored inter-shell interactions [38, 39, 40, 41]. Upon illumination with unpolarized white light, CSRs retroreflect light along their radial axis, producing a characteristic central reflection spot at the wavelength $\lambda_0 = \bar{n} \cdot P$ (from Eq. 2.12 with $\theta = 0$) with a bandwidth $\Delta\lambda$ as in Eq. 2.14. The off-axis cross communication interactions generate reflected light that is blue-shifted relative to the central retroreflection, due to the angular dependence of the Bragg diffraction via Eq. 2.12.

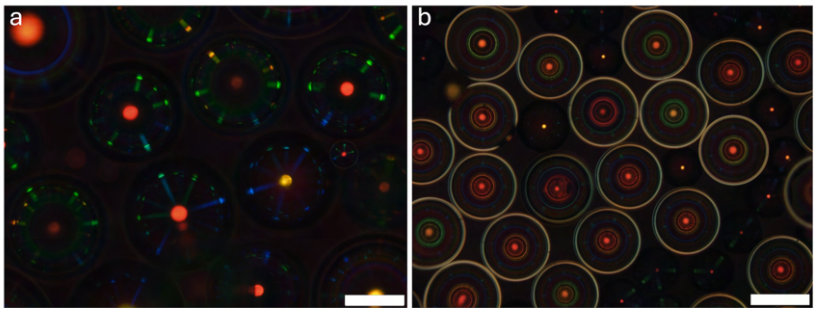

Figure 2.12: Polarizing microscopy images in reflection mode of a) randomly arranged CSRs with different sizes and pitch lengths, showing photonic cross-communication with different reflected wavelengths. (b) Asymmetric CSR shells with a thin top and thicker bottom, allowing light to enter and reflect internally, creating concentric rings. Thin-topped shells reflect in red or yellow, and appear alongside some CSR droplets. The shell asymmetry also causes wavelength-independent total internal reflection between the inner and outer phases, producing bright white rings. Scale bars: 100 μm. Reproduced from (a) [40] and (b) [42] on CC-BY licence.

Furthermore, the asymmetric geometry of CSR shells with a hole allows light entering through the hole and/or thinner part, undergoing multiple internal reflections within the shell[42, 43]. These internal trajectories allow light to interact repeatedly with the helical modulation, giving rise to concentric colored rings as shown in Figure 2.12b. The colors and spacing of the rings vary depending on the angle of incidence and the focusing depth during imaging[43]. These ring patterns are distinct from the peripheral dot-like reflections and provide an additional, dynamic optical signature. As a result of both light interactions between neighboring shells and through internal light guiding within the hole of CSRs, complex multicolored patterns are generated, which can be modulated dynamically by controlling the illumination area or direction [41, 42]. This cross communication opens new avenues for photonic sensing [44, 45, 46], encryption and authentication applications [47, 48, 49].

2.6.2 Microfluidic Production of Shells

While I have focused on the remarkable optical properties of CSRs so far, the questions remain: how they are actually made? How can we confine LCs within a spherical geometry? The typical method for producing LC droplets is simple emulsification, in which the liquid crystal is dispersed in an immiscible liquid by mechanical agitation. While this method is quick and low-cost, it offers little control over droplet size or uniformity, thus resulting in polydispersity. For example, in Humar and Musevic's study, where they presented CLC microdroplets as omnidirectional microlasers, a small amount of CLC was mixed into glycerol and stirred, generating an emulsion of randomly sized CLC droplets with diameters of 15–50μm [50]. This bulk emulsification method also requires multiple steps to obtain structures other than droplets. For example, core-shell type double emulsions, which are the precursors of CSR shells, are typically produced in a two-step process, and each emulsification step results in a highly polydisperse droplet distribution with poorly controlled structures. Today, microfluidic technology has become the widely used method for producing highly uniform and structurally consistent liquid crystal droplets and shells [4].

Microfluidics in a Nutshell

Microfluidics deals with the control and manipulation of fluids in channels with dimensions on the micrometers scale. As a more advanced alternative to the conventional bulk emulsification, the microfluidic method provides precise control over both size and uniformity, enabling the production of single, double and even multiple emulsions in a single step [51]. The development of soft lithography, pioneered by the Whitesides group as a method for producing prototype devices in polydimethylsiloxane (PDMS), an optically transparent soft elastomer, is one of the most significant contributions to the growth of microfluidics technology [52, 53]. Although soft lithography-based microfluidics offer many advantages, such as low cost and rapid prototyping for a wide range of flow geometries, they have limitations in terms of chemical and thermal stability [54]. In applications where such stability is critical—for example when working with organic solvents or under high-temperature conditions—glass or silica-based microfluidic systems are preferred.

In this thesis, I produce CSR shell precursors using a glass capillary-based microfluidics approach, following the design principles first demonstrated by Utada et al. that combines both coaxial flow and flow focusing [56]. This design consists of cylindrical glass capillaries with tapered ends, arranged so that the tapered tips face each other. These round capillaries are nested concentrically within a square glass capillary.

Figure2.13a shows a schematic illustration of a glass capillary device for generating double emulsions. The coaxial geometry is achieved by matching the outer diameter of the cylindrical capillaries with the inner width of the square capillary. In this setup, the inner fluid is introduced through the innermost tapered capillary (left), while the middle fluid, which is typically immiscible with the inner and outer phases, flows around it through the outer capillary in the same direction. This co-flow stream meets at the junction with the counter-flowing outermost fluid. The geometry of the device enables hydrodynamic focusing: the outer fluid squeezes the coaxial jet of inner and middle phases, guiding them into a collection capillary (right). Due to surface tension and interfacial instabilities between the immiscible fluids, the coaxial jet breaks up into droplets. This process is governed by the Plateau–Rayleigh

a.

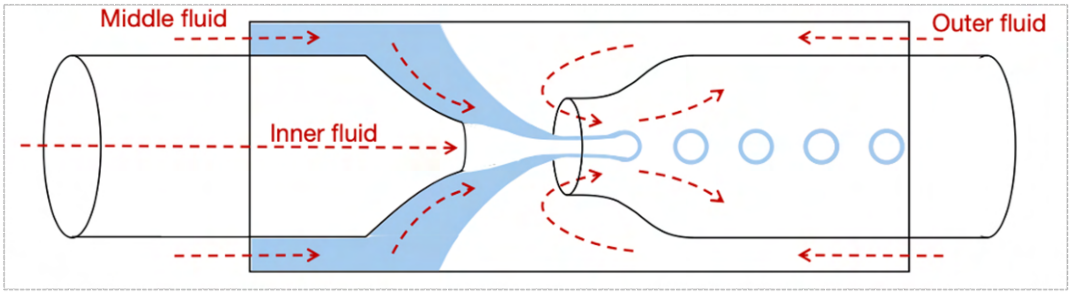

b.

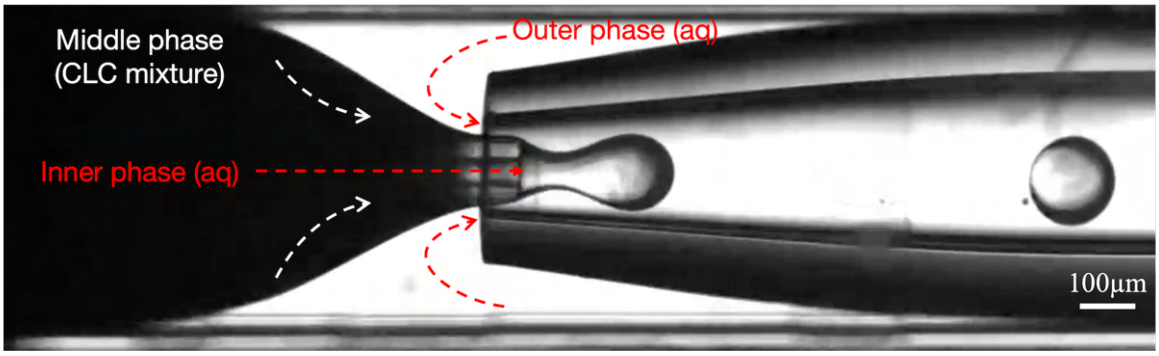

Figure 2.13: (a) Schematic drawing of the nested capillary set-up used for producing the CLC shells. The CLC is the middle fluid; the inner and outer fluids are isotropic aqueous solutions. Adapted with permission of [John Wiley & Sons], from [55]; permission conveyed through CCC, Inc. (b) Shell production process captured by highspeed video camera. Scale bar is 100 μm.

instability, where small disturbances grow until the cylindrical flow pinches off into droplets. It is the same principle seen when a thin stream of water from a tap breaks into drops. In our work, the CLC mixture serves as the middle phase, confined between two immiscible aqueous phases as shown in Figure2.13b. The shell diameter and thickness can be tuned by adjusting flow rates of the different fluids, as well as by varying the orifice size of the tapered capillary.

Chapter 3

Unobtrusive Fiducial Markers based on Cholesteric Spherical Reflectors

The unique optical properties of CSRs, in particular their selective reflection of circularly polarized light as mentioned in Section 2.6.1, indicate that there is significant potential for CSRs to be used to encode information on surfaces. The CSR-based patterns will then be highly distinguishable to imaging systems capable of detecting polarization contrast, even when placed in visually complex or textured backgrounds. This chapter introduces "CSR-Markers," an innovative version of fiducial markers that are unobtrusive to the human eye while remaining detectable by robots equipped with specialized sensors and detection algorithms.

3.1 Introduction to Fiducial Markers

Fiducial markers are artificial landmarks with specific geometric patterns, commonly used in robotics. A well-known example where fiducial markers appear is in QR-codes: each of the three corners with nested squares is a fiducial markers, that helps the device reading the QR-code to scale and orient the QR-code in order to properly decode it. A typical marker consists of a unique identification pattern, usually a black-and-white code that distinguishes it from other markers, and a border that separates/isolates the pattern from its surroundings.

Fiducial markers supports robotics operations as they facilitate the localization and orientation of robots and Augmented Reality (AR) devices. They also enable object recognition and scene understanding when specific objects are tagged or the environment is mapped out with these unique identifiers. Detection typically involves capturing video or images of the marker using a suitable camera, followed by image analysis to estimate the relative pose (the position and the orientation) between the camera and the marker. Then machine vision algorithms decode the embedded information. Although such markers offer significant benefits for robotics applications, the presence of multiple labeled objects in everyday environments can be aesthetically obtrusive and cause visual clutter as they are highly visible. For example, to ensure reliable detection in complex environments, printed markers must be relatively large, typically at least 10 cm × 10 cm [57]. Another limitation in deploying fiducial markers in human populated areas is the potential for false positives. As our everyday life is already visually dense with many tags, labels, posters and advertisements, certain patterns may unintentionally resemble reference marks.

These issues can be mitigated by designing markers using cholesteric spherical reflectors (CSRs), which allow for effective background subtraction [1] and thereby reduce the likelihood of false recognition. Furthermore, if the CSR reflections are designed to operate outside of the visible spectrum, the resulting markers can remain practically invisible to the human eye, enabling their integration into a wide range of environments with minimal aesthetic disruption.

3.2 State-of-the-Art of Fiducial Marker Technology Targeting Invisibility

Most fiducial markers have been developed focusing on technical performance, such as detection speed and accuracy. However, there is a growing interest in developing markers that are less visible or more aesthetically acceptable in everyday environments. Over the

[1] In this context, background subtraction refers to the optical isolation of CSRs from their environment by exploiting their polarization-selective reflectivity.

past decade, research in this direction has increased, motivated by the increasing presence of robots in human-populated areas, such as supermarkets and airports. As these technologies move out of robotics labs into real-world settings, there is also a need for markers that can be integrated without disturbing the visual appearance of objects or surroundings. Getschmann et. al conducted a survey study to evaluate how the existing marker designs are perceived by users and showed that commonly used black-and-white matrix design was unfavorable and described as ”ugly” and ”obtrusive” by participants [58]. In a more recent study [59] investigating the impact of fiducial marker visibility on task performance in a flight simulator, results showed that visible markers contribute to disruption in pilot's gaze behaviors. Several studies have shown that the unobtrusive markers can perform as effectively as traditional (printed) fiducial markers, and have been utilized in diverse robotic applications. Common strategies to develop unobtrusive markers are either to make the marker pattern more visually appealing by manipulating the shape and colors or to create hidden markers by targeting the infrared range for detection and/or integrating the marker into a target object.

Dogan et. al presented InfraredTags, 3D-printed markers using two types of filaments made out of polylactic acid (PLA): one that transmits IR light (IR PLA) and one that is opaque to IR light (regular PLA) [60]. This dual material approach provides a contrast upon detection by an IR camera under IR illumination. Although this approach provides an invisible pattern and rapid scanning of embedded markers, the fabrication of markers is limited to the IR range. The color of the filament itself prevents the printing of free standing markers to be labeled on already existing objects, as they would then be visible, and requires the integration of these markers within the 3D printed object. Similarly, BrightMarkers are 3D-printed fluorescent filaments embedded into objects and requires Near Infrared(NIR) cameras for detection [61]. Aircode introduced the concept of embedding markers directly into the fabrication of objects, enabling seamless integration for use cases such as robotic grasping [62]. Nevertheless, Aircode's significant drawback is its slow decoding process, which can take tens of seconds, depending on the camera's viewing angle.

In contrast to these existing approaches, CSR-based markers offer a versatile platform that

can operate in the near-infrared, visible, or near-ultraviolet spectrum, depending on the application. This spectral flexibility allows either shifting the detection outside the visible range for invisibility or tuning the appearance to blend into the background. Moreover, their freestanding form enables easy attachment to various surfaces, making them adaptable to diverse application scenarios without altering the object's appearance.

3.3 Optimization of CSR-Marker Fabrication

Traditional fiducial markers, which are typically produced by printing black toner on white paper, have a high visual contrast that makes them easy to detect with standard cameras. In this study, to create unobtrusive markers, we use CSRs as a functional material instead of toner particles. The CSRs are then embedded into a proper transparent binder and can be applied to various surfaces, not just paper. This shift in materials and target surfaces introduces some technical considerations.

3.3.1 Scalable Deposition and Patterning Strategies for Large Particles

Designing fiducial markers using CSRs introduces unique challenges in both deposition and pattern formation, primarily due to their large size, ranging from 100 to 200μm in diameter, and their light scattering behavior. Unlike conventional inks for printing, which often involve particles below 5μm, the manipulation of particles an order of magnitude larger requires a fundamental rethinking of established deposition techniques or exploring new approaches. The literature is limited on scalable and precise patterning methods for particles in this size range. While pearlescent pigments used in automotive or cosmetic coatings sometimes involve particles above 50–100μm, these are generally used in randomly dispersed configurations with quite low surface coverage rather than close-packed configurations.

Among the candidate techniques, screen printing emerges as a method with high-throughput potential. This technique has been adapted for use with functional inks containing particles up to approximately 100μm in diameter [63]. However, its implementation with CSRs re-

quires careful optimization of the ink formulation and mesh geometry to prevent clogging and to ensure sufficiently dense deposition. Spray coating offers another route, especially when applied to adhesive or pretreated substrates. This method enables the creation of densely packed layers. This approach becomes particularly relevant in later sections of my thesis where dye-infused CSRs (d-CSRs) are introduced. Another approach considered was dispenser-based deposition, which is promising for automation and integration into high-precision manufacturing workflows. However, the large size of CSRs poses a significant challenge, as nozzle clogging is a commonly reported issue in dispenser-based deposition and represents a major barrier to reliable use. Despite these limitations, this method is applicable, particularly if nozzle design and fluid dynamics are optimized for large-particle suspensions.

3.3.2 Current Semi-Automated Approach using Replica Molding

One of the most critical challenges is fully embedding CSR shells in a binder. The binder has a dual purpose of fixing the positions of the CSRs and providing refractive index matching to maximize reflection and minimize unwanted scattering. We use NOA160 (Norland Optical Adhesives), a commercially available optical adhesive, as a binder. NOA160 offers near-perfect refractive index matching with my CSRs and is user-friendly in terms of processing, making it suitable for routine fabrication. Although using shells gives us the advantage of being able to fill the CSRs both inside and outside with an index-matching binder, air penetration into CSRs should be avoided as trapped air bubbles cause strong scattering as shown in Figure3.1. For this purpose, we start by dispersing the CSR shells at high concentration in a mixture of NOA160 and acetone where the acetone serves to reduce the viscosity of the NOA glue. Directly mixing the shells with binder results in a relatively viscous fluid, which can trap air bubbles within the shells during mixing. By incorporating acetone, the reduced viscosity allows for more effective mechanical agitation to eliminate trapped air bubbles. This ensures a dense, bubble-free packing of CSRs in the binder, after the solvent is gently evaporated. This suspension should then be deposited on a fiducial marker template. If CSRs are applied to regions corresponding to the traditionally black areas of the marker, the white

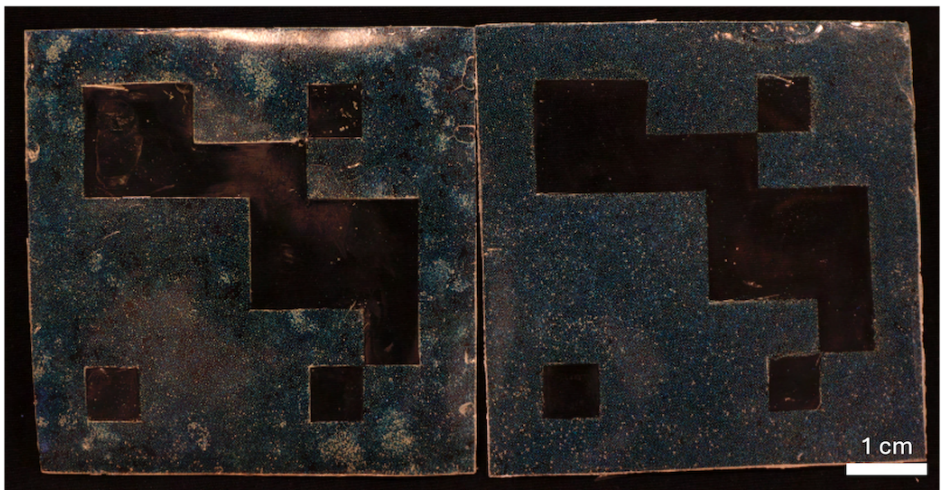

Figure 3.1: The first samples of the same fiducial marker pattern produced using green-retroreflective CSR shells (G-CSRs) embedded in NOA160. The presence of many beads in the left marker renders it more scattering than the right one. The right marker, made almost only with CSR shells and less beads, appears clearer but still exhibits noticeable scattering from trapped air bubbles both within the binder and inside the hollow CSR shells. Scale bar: 1 cm

areas are pure binder. Or in the exact opposite case, where the CSRs are white and the binder is in the black areas, a frame must be created using CSRs to define the boundaries of the marker. Therefore, we have CSR and non-CSR regions, like the black-and-white pattern, thus maintaining the visual contrast necessary for detection by machine vision systems.

Figure3.1 shows the first samples of CSR markers produced entirely through a manual process. In this method, I first prepared a fully cured square layer of NOA glue, then carefully cut out the desired marker pattern by removing regions where CSRs were intended to be placed. These voids were then filled with the CSR-binder mixture and cured once more under UV light to complete the marker. While these early prototypes demonstrated proof-of-concept functionality, the fabrication was highly time-consuming and automation was required to increase efficiency and consistency. Additionally, we observed that the long-term stability of markers made with the UV-cured NOA160 binder is not acceptable. Over time, the cured binder becomes noticeably rigid and even brittle. POM investigations revealed also the development of birefringent regions within the binder, which may be caused by strain-induced

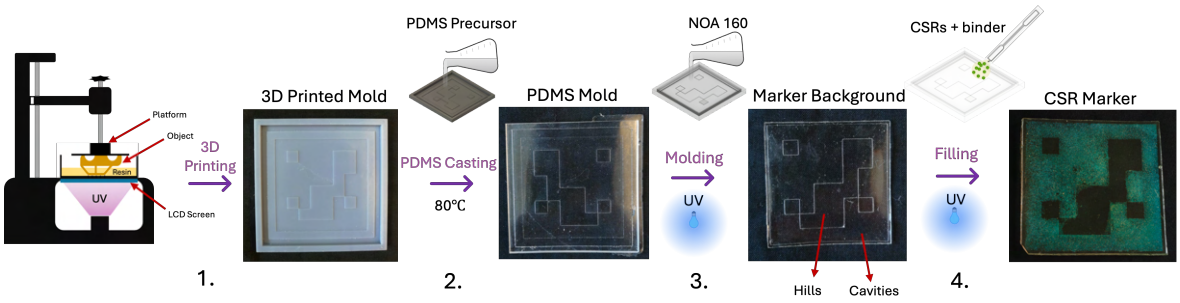

Figure 3.2: The schematic illustration of the steps of mold-based CSR marker production.

birefringence resulting from gradual material shrinkage. Although later chapters will explore alternative binder options to address this issue, we continued our preliminary experiments using NOA160 for consistency and comparison.

My current marker fabrication is based on the replica molding method. As illustrated in Figure 3.2, the process begins with the stereolithography (SLA) 3D-printing of a mold of the desired fiducial marker pattern, which is then used for casting PDMS to make a flexible and reusable negative replica. This soft template is then used to make the final positive copy, called the marker background, which identifies the regions where CSRs should not be present. To produce a marker background, I fill the PDMS mold with the binder (NOA160), place it upside down on a PVA-coated glass substrate, and press down firmly with a glass test tube as a rolling pin to eliminate air pockets. I then cure the binder by exposing it to UV light, and peel off the PDMS mold to obtain a solidified ”marker background” adhered to the glass substrate. The third step in Figure 3.2 shows such a NOA marker background consisting of cavities designed to be filled with the CSR–NOA160–acetone suspension. At this stage, the process becomes partially manual: I carefully deposit the CSR suspension into the cavities using a fine metal spatula, and remove any visible air bubbles with a needle to ensure uniform filling. After solvent evaporation, a final UV-curing step solidifies the CSR-loaded areas and completes the marker fabrication. This combination of automated mold fabrication and manual cavity filling defines the process as semi-automated. Once the reusable PDMS mold is available, a complete marker can be produced in around 20 minutes, with minimal material waste.

One problem I encountered during this replica molding was PDMS curing inhibition where the PDMS precursor came into contact with the 3D-printed mold. This resulted either in strong adhesion of the PDMS to the mold or a sticky, partially uncured surface. Many studies have shown that most commercially available SLA resins inhibit PDMS curing [64, 65, 66]. During thermal curing of PDMS, 3D-printed molds in contact with the PDMS can release unreacted monomers and phosphine oxide-based photoinitiators that can interact with the platinum (Pt) catalyst used in PDMS formulations such as Sylgard 184. The unreacted monomers can also promote undesired cross-linking at the interface, causing PDMS to adhere to the mold. To solve this problem, I implemented a simple post-treatment protocol consisting of 10-15 min UV exposure followed by heating at 120℃ in a vacuum oven [64]. UV curing helps further polymerize residual monomers, while heat treatment helps evaporate the volatile photoinitiator fragments. This combination solved the PDMS curing inhibition and enabled reliable mold release.

The main challenge in the current fabrication process is filling the marker background with the CSR–binder suspension. At this stage, a semi-automated method provides a workable solution: once the reusable mold is ready, a complete marker can be produced in under an hour without material waste. The filling step has turned out to be more challenging than initially expected, leading me to try several approaches in parallel. Several factors make CSR patterning more difficult than conventional printing processes. First, the CSR shells are significantly larger than standard pigment particles, ranging from 100 to 200 micrometers in diameter, compared to about 1 micrometer. Second, their hollow structure makes it essential to disperse them evenly in the liquid binder before deposition. Trapped air bubbles within the shells can cause strong light scattering, making the markers visible to the naked eye and reducing their contrast in machine vision applications. While I initially attempted to speed up the filling step using a bar coater, this approach resulted in uneven deposition caused by force chain formation among partially jammed CSRs and caused to irregular filling. As an alternative, a robot dispenser system is currently under consideration.

3.4 Detection Methods based on Selective Reflection of CSRs

Previous studies in our group have demonstrated CSR-based encoding of information laid out as text [35] and QR-codes [49] and how the polarization contrast can be used to reveal encoded patterns. However, in those works, the authors used a sequential imaging approach where they captured multiple images of the scene under varying polarization conditions using a single camera and then performed manual image-processing, which is an effective but time-consuming method and not applicable for real-time detection scenarios. Therefore, in this study, the most important aspect when building the prototype for detecting CSR-based patterns is a read-out device that works in real-time and provides dynamic background subtraction.

The ultimate goal of the study is, of course, to create markers and corresponding detection systems that operate in near-ultraviolet (UV) and infrared (IR) ranges. But first, we focus on developing and testing a system that works for visible light, where suitable components are more affordable and easier to access. Most commercially available cameras have built-in filters that block IR and UV light, and optical elements such as circular polarizers and beam splitters are optimized typically for visible light; for example, many visible-range polarizers absorb UV light. Since it is not possible to build a single setup that performs equally well across all wavelengths, we adopt a modular approach: different setups should be designed for UV, visible, and IR light, respectively.

3.4.1 Dual-vision setups

The basic idea is to capture the same scene by two cameras simultaneously detecting two different polarization states; one camera with a right-handed circular polarizer and a second camera with a left-handed circular polarizer. At the same time, there should be a single input for the imaging system to avoid the parallax problem caused by the slight spatial shift between the two cameras or lenses in stereovision imaging setups. Our first generation (G1) readout system consists of readily available optical components: a beam splitter, two identical circular polarizers, and two USB cameras. The beam splitter is used to split incident

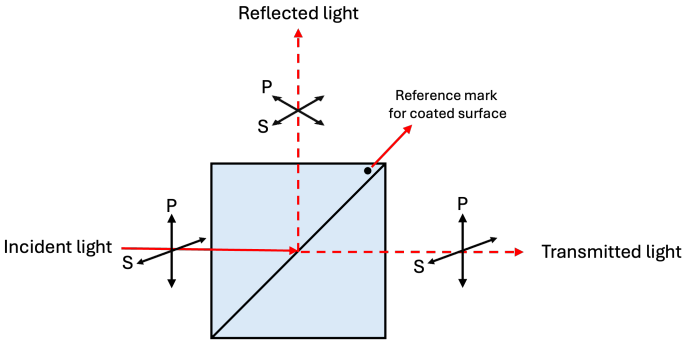

Figure 3.3: Schematic illustration of a non-polarizing cube beam splitter. The incident light is separated into reflected and transmitted components, with both S- (perpendicular to the plane of incidence) and P- (parallel to the plane of incidence) polarization states.

light into two separate paths at a specific reflection-to-transmission ratio (R/T), i.e. 50/50 in our case. Beam splitters are often categorized by their construction shape: cube or plate. Figure 3.3 shows a cube beam splitter consisting of two right-angle prisms glued together along their hypotenuse where a surface of one prism has a reflective coating. When light hits the coated surface, half of it is reflected at a 90-degree angle, while the other half transmits through straight. In addition to splitting beams, a beam splitter also serves as a mirror converting right-handed polarization into left-handed, and vice versa.

In the G1 dual-vision setup, pictured in the Figure 3.4a and, designed and constructed by Dr. Hakam Agha in the Experimental Soft Matter Physics group, the cameras are perpendicularly positioned on either side of the beam splitter, and polarizers are mounted directly in front of the lens of each camera. Light from the scene enters through the front aperture of the beam splitter. This light is divided: half passes straight through to the first camera, while the other half is reflected at a right angle toward the second camera. Since unpolarized light is equally transmitted to both cameras, subtracting the images captured by each sensor effectively cancels out the background, isolating the polarized components of the scene, which are normally only the patterns generated by CSRs. The key to this configuration lies in the behavior of circularly polarized light upon reflection. A right-handed circularly polarized signal reaching the first camera is compatible with its polarizer and thus detected. However, when the same light reflects off the beam splitter and travels toward the second camera,

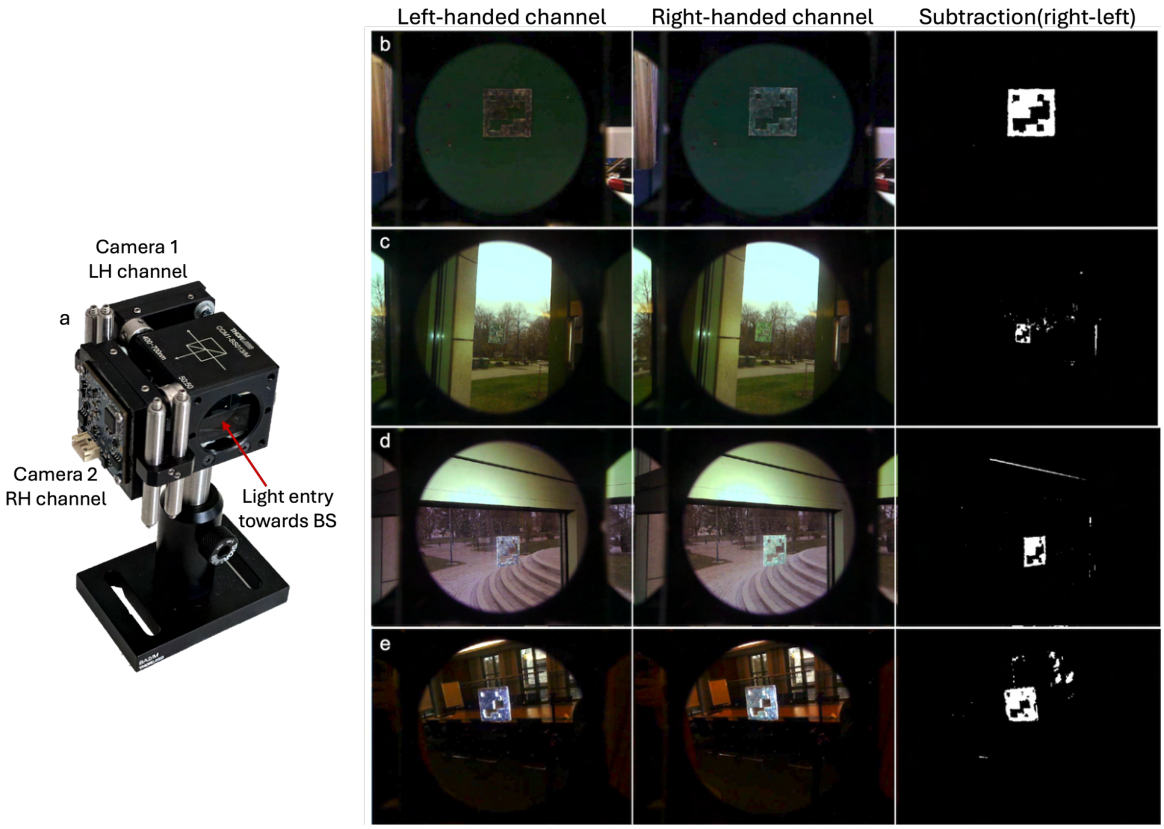

Figure 3.4: (a) Dual-vision imaging setup for CSR-Marker detection based on background subtraction, containing two USB cameras with circular polarizers of the same handedness attached in front of their lenses and facing a cube beamsplitter. b–e) Screenshots from software performing real-time background subtraction for CSR-marker detection produced by green retroreflective, right-handed CSR shells (with approximately 5–10% bead presence). The markers are placed on backgrounds and imaged using the dual-vision imaging setup. The first and second columns display the raw video input for left- and right-handed circular polarization, respectively; the third column presents the substraction result (the right subtracted from the left channel), converted to monochrome and processed further. In (b), the marker is placed on green color metallic surface. Frames (c-d) show the marker placed on a window with natural scenery (c) and an urban environment (d) behind it. In frame (e), the marker is placed on a mirror reflecting a room with windows. In all cases, the marker is illuminated from the imaging direction using a white torch placed next to the imaging set-up. For improved visibility, screenshots in (b) and (e) have been uniformly brightened post-capture due to the low original exposure. Reproduced from [33] on a CC-BY license

its polarization is inverted (due to mirror reflection), becoming left-handed. Because both cameras use identical polarizers (right-handed polarizers in this case), the second camera

blocks this reflected light. The reverse applies to left-handed signals: they are blocked from the first camera but become right-handed upon reflection and are detected by the second. This clever setup enables differential imaging of circularly polarized features, such as those produced by CSRs, while filtering out ambient, unpolarized light. Importantly, it also filters out linearly polarized light, which may be present in many scenes due to Brewster angle reflections or due to large-angle Rayleigh scattering. Circular polarization, in contrast, is very unusual in natural scenes.

Once the dual-camera setup captures the scene, the acquired video streams are processed through custom image analysis software designed by my colleague Ali Tourani to detect polarization contrast. The software aligns the outputs of the two cameras and performs a real-time subtraction of two inputs, effectively filtering out the background and highlighting only the optical signal generated based on the selective polarization of CSR patterns. Given that the two cameras are mounted on orthogonal sides of a beam splitter, small mechanical misalignments are unavoidable during assembly and thus an initial calibration step is required. The resulting color image is then converted to monochrome to simplify processing. The entire software is implemented in Python and includes a real-time graphical user interface (GUI). This interface allows for manual adjustment of brightness, contrast, and color channel masking. The GUI displays the live video feeds from both cameras and the subtracted image side by side simultaneously.

Figure 3.4b-e shows the real-time background subtraction results of the detection system. The markers in the images are made from right-handed CSRs with green retroreflection and are placed in four different environments, including challenging scenarios with glasses and mirrors. In each case, the left and middle images show the raw video feeds from the two synchronized cameras, while the rightmost image presents the processed output after background subtraction. A commercial white LED torch, aligned with the cameras' viewing direction, ensures consistent retroreflective illumination. Despite variations in the background—including colored surfaces, outdoor scenes through a window, and even reflections in a mirror—the system consistently highlights the CSR pattern with high contrast. While

some minor alignment artifacts remain due to hardware and calibration limitations, these do not affect the overall detectability of the marker. Importantly, even in complex scenarios involving specular reflections or transparent surfaces, which are common in real-world robotics applications, our method proves robust and effective. This confirms the viability of CSR-based background subtraction for real-time fiducial marker detection, with room for further optimization in future iterations.

This setup had the advantages of simultaneously observing the same scene with the two cameras, having a user-friendly approach, where one could simply plug the setup into a computer and make it immediately functional, and easy processing of the camera outputs to detect CSR markers. However, it also had some drawbacks. The system is relatively heavy, making it unsuitable for mounting on drones or mobile robots. Additionally, while synchronization between cameras is essential to capture the scene simultaneously, the specific cameras used in this setup do not support hardware-level synchronization. Furthermore, to support high-speed robotic tasks, cameras with global shutters are required to avoid motion-induced distortions. To address these limitations and make the system more suitable for robotics applications, we decided to update the setup. Therefore, we designed a custom 3D-printed cube cage providing a larger opening towards the scene and thus a wider field of view, see Figure 3.5. We also upgraded to two new visible-range cameras that support synchronization and include global shutters, higher resolution, better software support libraries, etc. We also replaced the original cube beamsplitter with a much lighter plate beamsplitter.

The plate beam splitter offers the same optical function but lacks the optical adhesives that can absorb light and reduce transmission efficiency. This updated system solves many of the earlier issues. It is lighter, easier to modify, provides synchronized and distortion-free imaging, supports improved software tools, and has a wider field of view (65 degrees compared to 40 degrees in the original setup). While the view is still somewhat limited by the structure of the cage, it is sufficient for most applications.

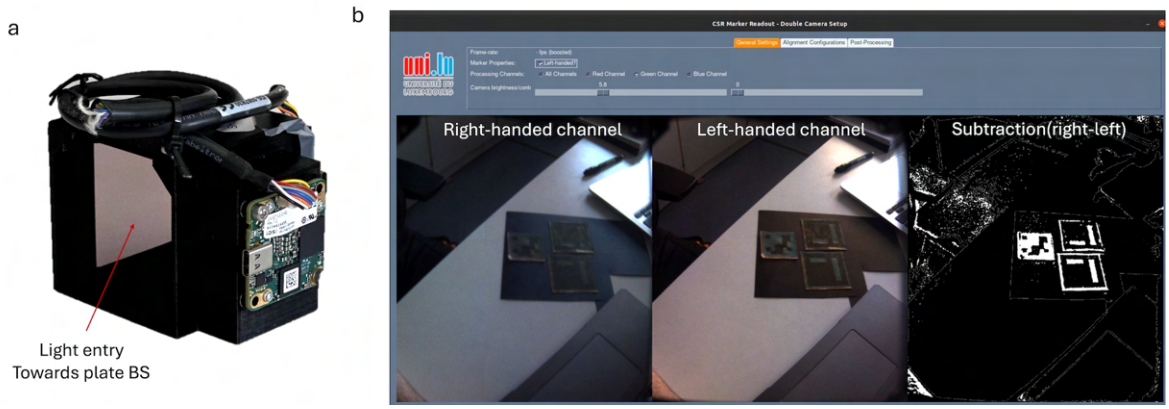

Figure 3.5: (a) The generation-2 dual-vision imaging setup designed for real-time detection of CSR-based markers, optimized for robotics applications. The system features a 3D-printed cube cage with a wider front opening to increase the field of view, two synchronized visible-range global shutter cameras equipped with circular polarizers of the same handedness, and a lightweight plate beam splitter replacing the original cube splitter. (b) Marker detection results for three different ARUCO marker patterns prepared by G-CSRs. The first and second columns display the raw video input for right- and left-handed circular polarization, respectively; the third column presents the substraction result (the right subtracted from the left channel), converted to monochrome and processed further. Illumination was provided from the imaging direction using a white light source placed adjacent to the setup.

3.4.2 Single-vision setup

Another detection approach is to use a single camera with a polarizer, rather than two cameras, to eliminate the common issue of image misalignment that is often found in dual-camera setups. To overcome this issue and enable robust detection of CSR-markers, we designed a compact, single-camera imaging system that uses a switchable circular polarizer to alternate between polarization states without changing the camera's position. The system combines a fixed circular polarizer with a liquid crystal (LC) half-wave ($\lambda/2$) plate mounted in front of the camera lens. A 2 μm thick commercial LC cell (from EHC) filled with the nematic LC mixture ZLI-1132 (birefringence 0.1396 at 589 nm, 20℃) [67], functions as a $\lambda/2$ plate when no voltage is applied (OFF state), changing the handedness of circularly polarized light reflected from the CSR marker. The cell features parallelly rubbed polyimide coatings on both glass substrates, ensuring a uniform planar alignment of the nematic LC in the absence of an applied field. A set of 1 cm² transparent ITO (indium tin

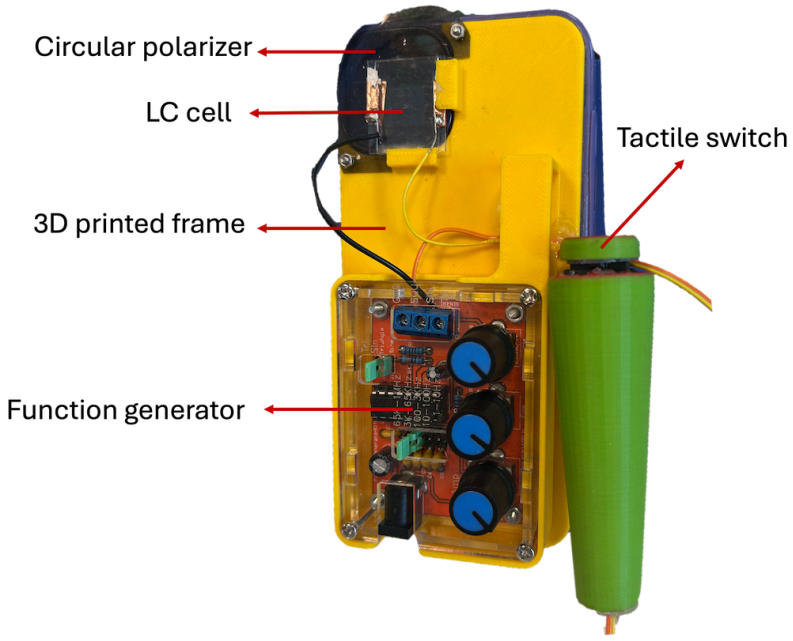

Figure 3.6: Photograph of the compact, mobile phone-based dual-polarization imaging setup developed for the detection of CSR-based patterns. The system integrates a fixed circular polarizer and a switchable liquid crystal half-wave plate mounted in front of a mobile phone camera. A tactile button connected via a flexible cable controls the polarization switching without disturbing the camera position. This system was used to capture the detection results presented in Chapter 5.

oxide) electrodes allow for the application of an electric field across the cell. When an AC voltage is applied via a mini function generator connected through a tactile on/off switch, the director alignment of the LC phase switches from planar to homeotropic, and thus the apparent birefringence effectively reduces to zero, so the LC cell no longer functions as a $\lambda/2$ plate, and only the fixed circular polarizer determines the polarization state reaching the camera. Switching is controlled by a tactile button, connected to the setup via a flexible cable in a way that avoids mechanical disturbance of the camera, ensuring consistent image alignment and avoiding motion blur during operation. The whole setup is mounted using a custom-designed and 3D-printed holder attached to a mobile phone case as shown in Figure 3.6. By switching the LC cell between ON and OFF states, the system captures images of the same scene alternatingly through left- and right-handed circular polarizers using a single

camera. Although the OFF-to-ON switching of the LC is nearly instantaneous, the slower ON-to-OFF relaxation leads to a temporary deviation from the desired function either as a λ/4 plate or without function, thus losing polarization control over some frames after switching off. For this reason, the background subtraction should always be done by comparing subsequent video frames recorded during the OFF-to-ON sequence when using this setup. Once optimized, the frame subtraction between these two captures reveals the hidden CSR pattern. This single-camera, polarization-switching approach offers a practical and compact alternative to dual-camera systems. It enables reliable CSR-based marker detection with reduced hardware complexity, improved alignment, and compatibility with mobile devices, but its reliance on two sequentially obtained images means that rapidly moving objects may not be subtracted as intended. In general, the frame rate must be high enough that all motion between two subsequent frames is negligible. This single-camera imaging setup was developed in parallel with the contrast enhancement efforts described in Chapter 5, where it is used extensively to demonstrate detection of d-CSR-based patterns under real-world conditions. An example application of this setup will also be presented in the next section.

3.4.3 Illumination and Imaging Constraints in Applied Scenarios

To evaluate whether our current system supports real-time detection, we conducted initial tests during a visit to our collaborator, Mathew Schwartz, at the New Jersey Institute of Technology (NJIT). The idea was to integrate our dual-camera imaging setup and a visible light torch onto a robotic arm of a KUKA construction robot available in his labs, simulate basic construction tasks, and observe whether the system could detect CSR markers placed on walls. During these experiments, we encountered a major limitation: under realistic conditions, the $5cm5cm$ markers were not possible to detect with the current setup. The flashlight had to be adjusted to its most focused setting where the light beam barely covered the marker, making the illumination impractical for real-life scenarios that require detecting multiple markers in a broader scene. Since the robot must detect markers without knowing their locations in advance, the current combination of marker size, CSR reflectivity, illumination strength, and camera resolution is insufficient to use for realistic construction experiments.

The main reason behind the poor detection performance we identified is the relatively low reflectivity of the CSR markers as we made them up to now. This limits their visibility, particularly at long distances. To improve the reflectivity, we have some strategies, such as using smaller CSRs or distribution of mixed-sized CSRs to increase the number of reflectors per unit area. Additionally, newly developed CSRs with focal conic domain configuration are promising to offer higher retroreflectivity [34]. However, the most exciting and most striking improvement is achieved by infusing black dye into the CSRs, as I will describe in detail in Chapter 5. Another constraint was the low resolution of the imaging system. The cameras used in these tests lacked the resolution needed to detect the fine details of the markers over realistic operational distances.

Following the observations made during our tests at NJIT, I started considering natural examples of highly visible structural coloration as potential references. Jewel beetles, well known for their vibrant iridescent exoskeletons, are a prominent example of structural color in nature [68, 69]. To compare the visibility of our CSR-based markers, I conducted a test using a mobile phone-based dual-polarization imaging setup. In this experiment, I placed both a CSR-marker,backed with a printed black-and-white version of the same pattern to enhance contrast, and two jewel beetles in an indoor environment, see Figure 3.7. I then captured images through left-handed and right-handed circular polarizers at increasing distances under ambient lighting.

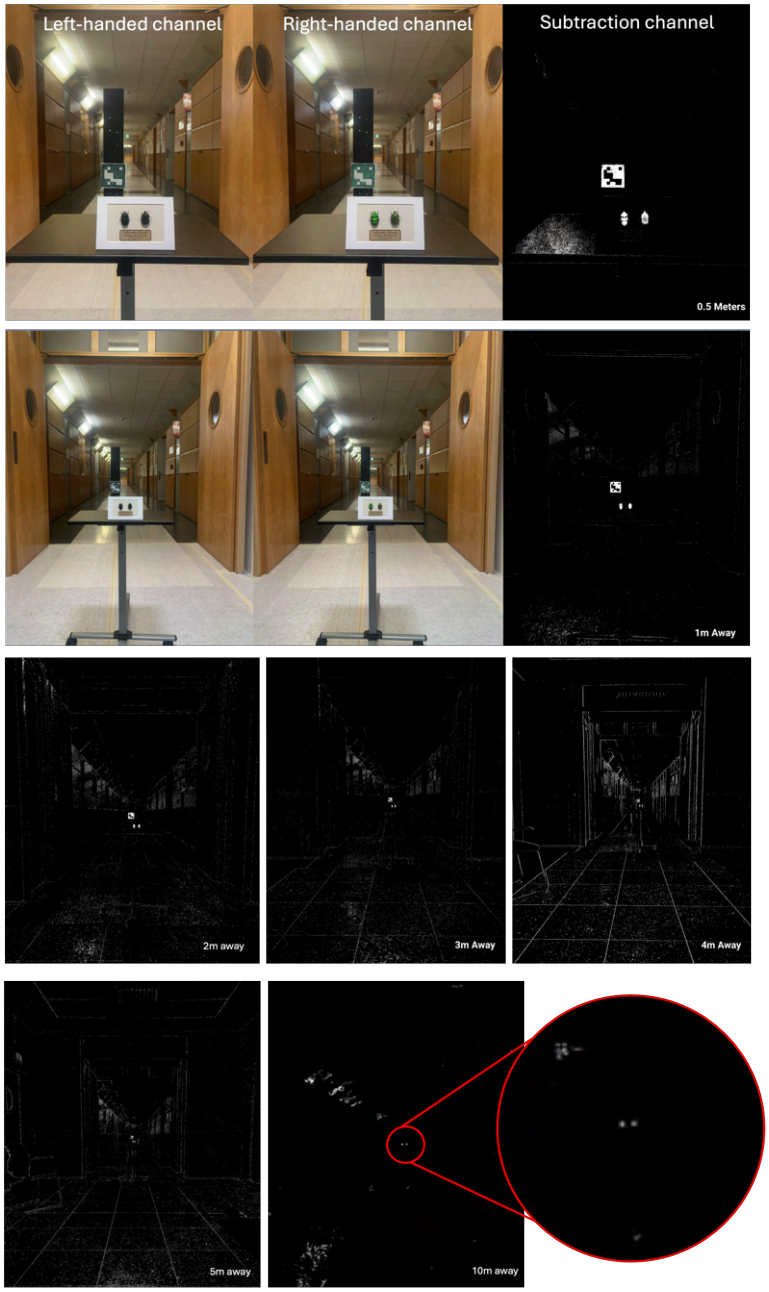

Figure 3.7: Comparison of long-range visibility of a green retroreflective CSR-marker and two jewel beetles in an indoor environment using a mobile phone-based time-sequential dual-polarization imaging setup. Images were captured through left-handed and right-handed circular polarizers at increasing distances. The top two rows show the LH, RH, and subtraction images, at 0.5m and 1 m. The bottom rows display only the subtraction images from 2m to 10m in 1m increments. A zoomed-in inset is included for the 10m image to highlight the visibility of the beetles.

Up to approximately 4 meters, both the marker and the beetles were detectable. However, beyond this range, the marker became increasingly difficult to distinguish, and eventually disappeared from the subtraction channel, while the beetles remained visible even at a distance of 10 meters. This comparison shows the superior reflectivity and optical contrast of biologically evolved structural coloration while demonstrating the limited visibility of our CSR-marker and the need to enhance the color and polarization contrast of our CSR-based system for detection over longer distances. It also emphasizes a common challenge in the development of artificial structural color materials: their reliance on a dark background to achieve sufficient visual contrast [70, 71, 72, 73]. In our case, the printed background provided the necessary contrast between the LH and RH channels, which was otherwise insufficient for reliable detection through background subtraction. To overcome this dependency on dark backgrounds, I explored a strategy of infusing a black dye into the CSRs. I present the promising results in Chapter 5.

3.5 Extending Polarization-Based Detection beyond the Visible Spectrum: in IR and UV Ranges

Achieving invisibility to the human eye requires tuning the retroreflection wavelength of CSRs out of the visible spectrum into the IR or near-UV range. This can be done by tuning the cholesteric pitch p in the material, as described in Equation 2.12. By adjusting the concentration of the chiral dopant in the mixture, we can readily tune p, and thus shift the reflection wavelength to the desired IR or near-UV region. Even though this spectral tuning is straightforward, adapting CSR-marker technology to the invisible range brings some optical and material challenges. These include limitations in binder transparency at the target wavelengths, reduced availability of optical components (e.g., circular polarizers, beam splitters), and the need for customized imaging setups. The following sections deal with how the imaging and detecting systems for CSR-based patterns can be transferred to the IR and near-UV range, and the technical and optical challenges encountered in these ranges.

One potential optical issue is blue-shifted reflections caused by the photonic cross-communication and internal shell reflection, which can make a supposedly invisible marker visible. In the UV range, these blue-shifted reflections are not problematic because they remain in the deeper UV region and do not affect the visual appearance of CSR-based markers. In contrast, for near-IR CSRs, blue-shifted reflections from shell-internal reflections and cross-communication can fall into the visible range unless the central wavelength λ_0 is long enough. Additionally, oblique reflections that occur when the illumination is opposite to the observer, also cause blue-shifted reflections [33]. These visible signals can be effectively avoided if the central retroreflection wavelength λ_0 is approximately 1.7 μm or greater [35]. However, equipment that operates at such long IR wavelengths is expensive and not commonly available. Most commercial IR systems, standard night vision tools, work at 850 or 940 nm. As I mentioned earlier, most commercial cameras are manufactured with filters that block IR and UV light. Additionally, while optical elements such as circular polarizers are widely available for visible light (e.g., in 3D glasses), those for UV and IR are more difficult to find and limited in design flexibility. Therefore, we first started by testing only the retroreflection behavior of markers prepared by IR and near-UV CSRs, using NOA160 as a binder. Figure 3.8 presents IR- and UV-CSR-markers placed in an interior setting, and imaged using a modified DSLR camera with its built-in UV/IR filter removed. The light sources we used are standard commercial LEDs: a 940 nm night vision flashlight for the IR marker and a black light torch (380 nm) for the UV marker. We also collected photos of both IR and UV markers using a regular phone camera (bottom row), to compare the images of the same scene captured by a modified DSLR camera (top row). The first two columns show the IR marker under different illumination conditions; the other two columns show the same for the UV marker. Under ambient white light only (frames a/e and c/g), the markers are barely visible. One might notice them with prior knowledge of their location and upon close check. Although both markers appear mostly transparent, the IR marker's pattern is faintly visible given that λ_0 is just outside the visible range. The UV marker pattern, however, remains undetectable. When we turn on the wavelength-specific flashlights along with the ambient light, i.e., 940 nm (frames b/f) for IR and a blacklight (frames d/h) for UV-marker, a clear difference

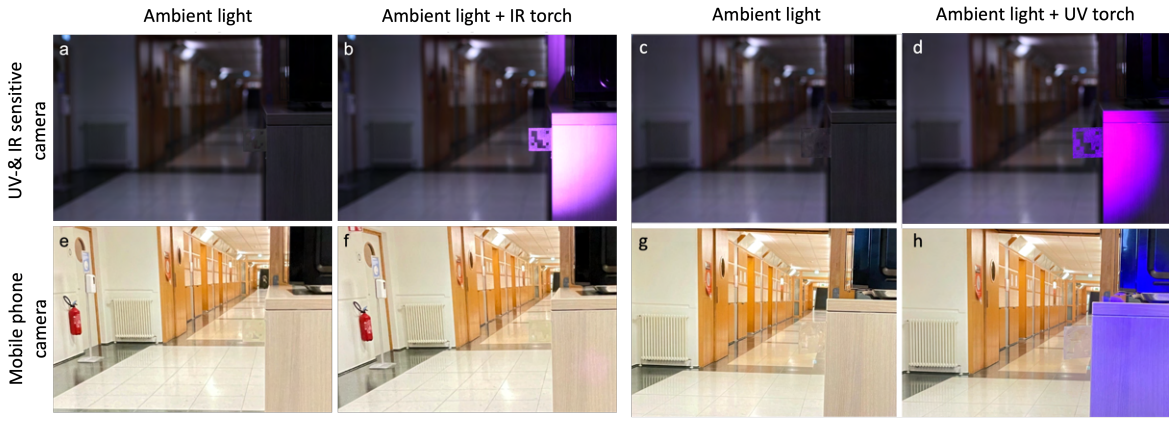

Figure 3.8: Macroscopic images of near-IR (columns 1–2) and near-UV (columns 3–4) CSR-markers placed in indoor environment. Top row: captured using a modified DSLR camera with the UV/IR blocking filter removed. Bottom row: captured using a standard mobile phone camera. Illumination conditions are as follows: ambient white ceiling light only in (a/e) and (c/g); ambient light plus a 940 nm IR torch in (b/f); and ambient light plus a 380 nm UV torch (d/h). Under standard illumination, the patterns are barely visible. However, when imaged with a UV/IR-sensitive camera and illuminated with the corresponding light source, the markers become clearly distinguishable. No polarization filters were used, so the background remains visible. Size of the marker: 5 cm x 5 cm. Reproduced from [33] on a CC-BY license.

appears between the images captured by the two cameras. The UV/IR-sensitive camera captures a strong, distinct signal from the CSR-filled regions of the markers, while the NOA-only regions remain transparent. As expected, nothing changes in the mobile phone images since the built-in UV/IR blocking filter prevents detection, except in the frame (h), where a violet signal appears. This is due to the some violet components of the UV flashlight, which supposedly emits light around 380nm.

These results demonstrate that CSR-based markers can be spectrally tuned to the UV and IR range for machine readability while remaining unobtrusive to the human eye, provided suitable lighting and imaging equipment are used. Given the promising initial results, I then started with designing a setup for detecting CSR markers operating outside of the visible range. I chose to focus first on the UV range as the IR-CSRs prepared initially by my colleague Xu Ma, designed to ensure a central wavelength (λ_0) long enough to avoid blue-shifted reflections, showed stability issues. During the annealing, the CSR precursor shells

frequently collapsed/popped. Therefore, I postponed further work on the IR range until the issues were resolved.

3.5.1 Toward Detection of UV-Markers: Material Considerations and Setup Design

Target Wavelength and Illumination Constraints

The primary concern when considering any technology that uses UV light in human-populated areas is the potential harm to human skin and eyes. Although UV radiation can be harmful in high doses or over prolonged exposure, the wavelength targeted in this study to achieve invisibility is 380 nm. This lies just beyond the visible spectrum, at the edge of what is still considered perceptible to the human eye. While the typical lower limit of human vision is around 400 nm, the sensitivity may extend down to 380 nm. Wavelengths below this fall into the UV-A region (315–400 nm), which is effectively invisible to the human eye. It is important to note that such light is also present in sunlight at significant intensities and is emitted by everyday light sources, such as fluorescent lamps. Therefore, using near-UV wavelengths for CSR-marker illumination may be feasible without posing safety concerns. This narrow shift we need to apply here is relatively low-risk, especially when used with low-power LEDs and controlled illumination setups. Nevertheless, further analysis is required to confirm long-term exposure limits and safety thresholds.

A more practical challenge related to illumination is that many commercially available UV sources, such as “blacklight” LEDs, also emit visible violet light. This visible component can make the marker visible to the human eye, which defeats the purpose of creating unobtrusive fiducial markers. Therefore, to achieve invisibility, the illumination source must emit a narrow-band UV and may require a filter to block the visible light. To understand the spectral characteristics of our available UV light sources, I decided to measure and analyze the emission spectra of different UV illuminators we purchased. I tested a few common commercial UV-LED flashlights, along with a computer-controlled UV-LED unit (AMS Technology), and compared the results in Figure 3.9. To compare the emission spectra of all UV sources, an

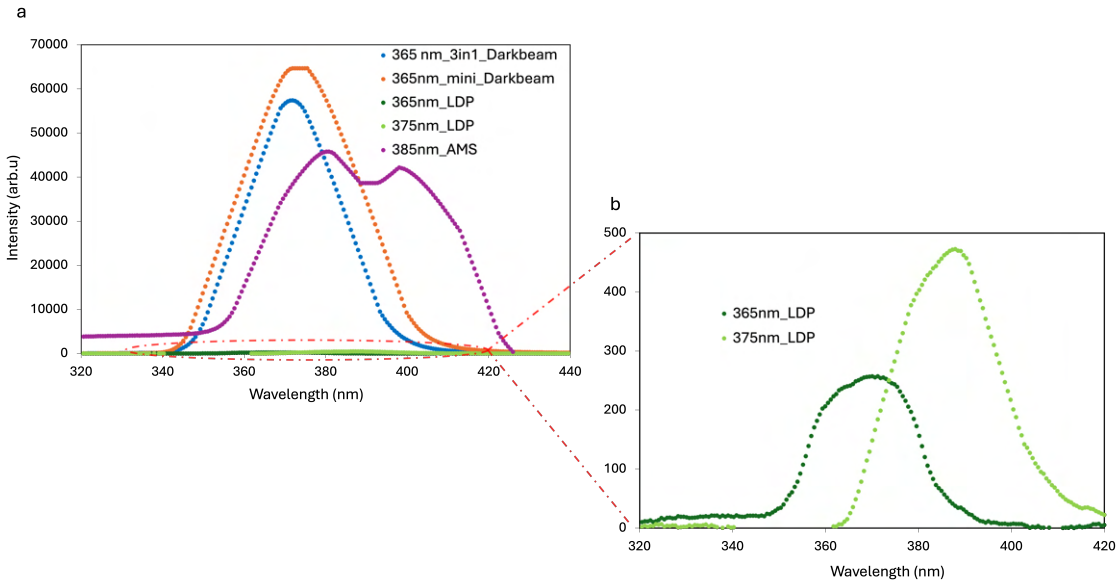

Figure 3.9: Emission spectra of different UV sources available in our lab measured at an equal distance from the detector of an AVANTES AvaSpec spectrophotometer. (a) All UV sources plotted together on a linear scale. Due to the wide variation in intensities, emissions from weaker sources are not clearly visible in this view. A red ellipse highlights the low-intensity region of interest. (b) A zoomed-in view of the highlighted region, showing the spectra of low-intensity sources that are not visible in the full-scale plot.

initial plot (Figure 3.9a) displays the full dataset on a linear scale. However, due to the large variation in intensities, the weaker emissions are not visible. To address this, a second plot (Figure 3.9b) presents a magnified view of the low-intensity region (indicated by red dashed lines).

Measurements confirmed that most UV flashlights available on the market strongly emit violet light and are not suitable for applications requiring complete invisibility unless we block unwanted components with a bandpass filter. On the other hand, two flashlights (Llewellyn Data Processing-LDP LLC) that were supposedly designed not to emit visible light had very weak light intensity. Although these two light sources successfully blocked unwanted short wavelengths in the UVA region and were eye-safe, the weak intensity rendered them unsuitable for use. The computer-controlled LED system appeared more promising because, despite emitting visible light and short wavelengths of UV light, the light intensity can be

precisely adjusted via software. To examine in more detail how the visibility of the marker varies depending on the light source, I mounted a UV-CSR marker on a black wall and used different UV light sources while taking images both with a UV-sensitive modified DSLR camera and a standard mobile phone camera. Each light source was tested at a fixed distance to maintain consistent comparison. Figure 3.10a shows the marker under ambient indoor lighting only. As expected, neither camera reveals the encoded marker pattern, although the square shape of the marker is visible due to scattering at the edges. In the following rows (Figures 3.10b–f), each image pair shows the marker illuminated by a different UV light source. As seen in the DSLR images, most sources reveal the encoded pattern clearly, except for the 365 nm and 375 nm LEDs from LDP (row b-c), which are too weak to generate visible retroreflection. These results match the earlier emission spectra analysis. In the mobile phone images, several sources also have a noticeable cyan glow due to the fluorescence of the NOA glue.

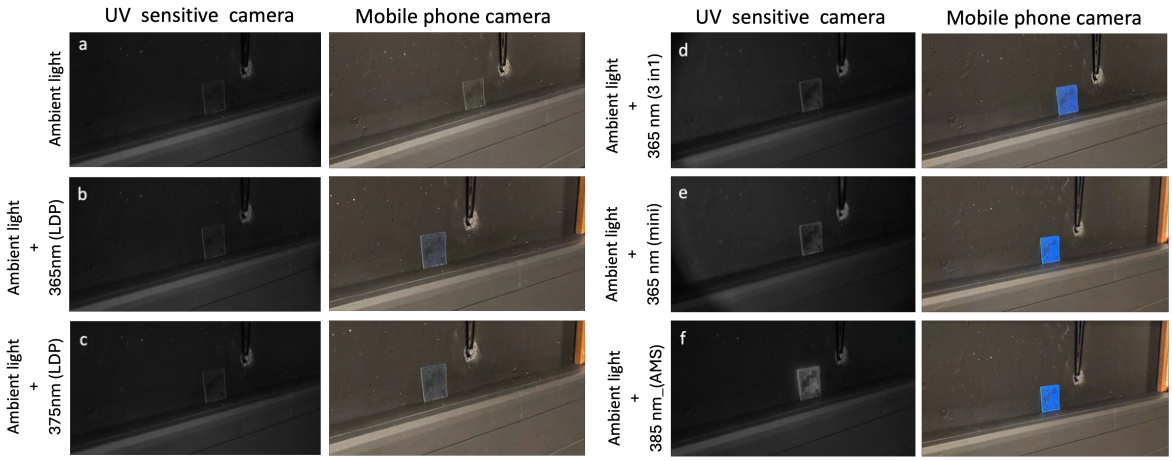

Figure 3.10: Comparison of CSR marker visibility under different UV light sources, captured using a UV-sensitive modified DSLR camera (left column) and a mobile phone camera (right column) under various illumination: (a) Ambient room lighting only, (b) 365 nm LED (LDP), (c) 375 nm LED (LDP), (d) 365 nm “3-in-1” LED, (e) 365 nm mini LED flashlight, (f) 385 nm computer-controlled LED (AMS).

Binder Transparency Issue/ Alternative Binders

As I started adapting our imaging setup to operate in the UV range, I encountered a major problem related to our standard binder material, NOA160. Once I switched from the modified DSLR camera to dedicated UV-only USB cameras, I immediately observed that the CSR markers appeared pitch black under UV ilumination (Figure 3.11a). This observation is a clear indication that NOA160 glue strongly absorbs light in UV wavelengths. This visibility issue had not arised in earlier tests (see Figure 3.8), most likely because the modified DSLR camera can also detect visible light. It probably masked the absorption behavior of the binder as we capture a mix of visible and UV signals. To better understand what was happening, I measured absorption spectra of several polymerized films: CLC films prepared using the CLC mixtures with varying chiral dopant concentrations (2.0%, 2.4%, and 2.6% wt.), an isotropic film made by heating the mixture above its clearing temperature prior to polymerization, and a NOA160 film. I plotted the results on the same graph as in Figure 3.11b. The results confirmed that NOA160 exhibits strong absorbance extending from 300 nm to approximately 420 nm in the visible range. In contrast, both the isotropic and CLC films showed absorbance only in the deep UV region (300 and 350 nm), which lies outside our target range. Since the CSR marker visibility relies on retroreflection at the design wavelength, it is essential that the binder material is transparent in that range. If the binder absorbs light at the illumination wavelengths, it prevents light from reaching the CSRs and effectively eliminates the optical signal from CSR markers. These findings confirmed that NOA160 is not a suitable binder for UV-range operations.

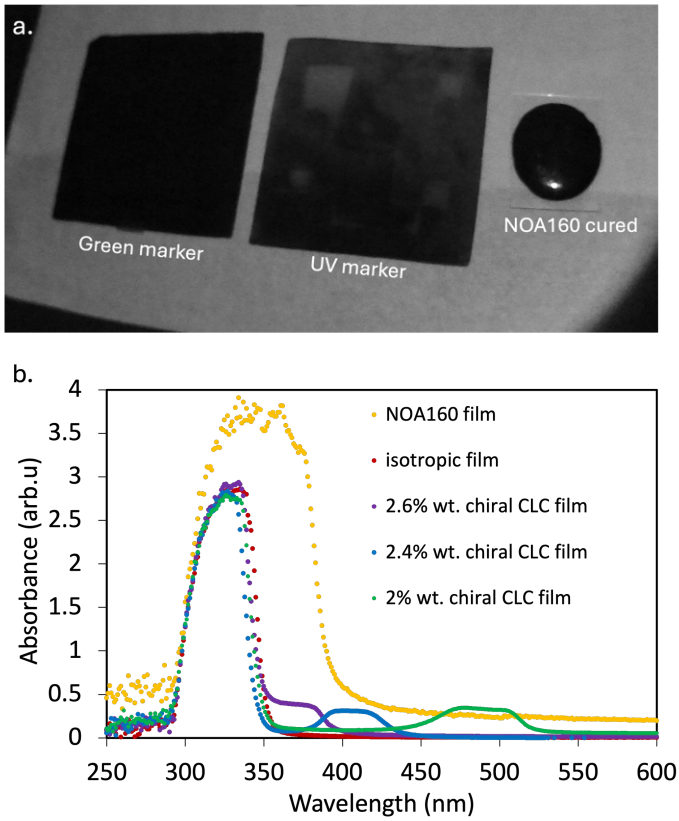

Figure 3.11: (a) Macroscopic image comparing the appearance of a green CSR marker (left), a UV CSR marker (middle), and a NOA160 glue sample (right) cured on a glass slide, all illuminated under UV light and imaged using a UV-only USB camera.(b) UV–visible absorption spectra of polymerized samples: NOA160 film, isotropic film, and several CLC films fabricated with mixtures varying in chiral dopant concentrations (2.0%, 2.4%, and 2.6% wt.).

The limitations of NOA160 in UV-range applications prompted a search for alternative binder materials that are transparent, optically isotropic, and also compatible with our marker fabrication process. During a short research visit to the group of Prof. Danqing Liu at Eindhoven University of Technology (TU/e), I investigated several acrylate-based monomers with high refractive indices as potential binder candidates. One of the first promising materials was a commercially available acrylate monomer, AgiSyn™ 2871 (Covestro) (Figure 3.12a), previously used by Belmonte et al. in the preparation of CLC particle-based reflective coatings [74]. Building on this, I expanded the search to include other monoacrylates with similarly

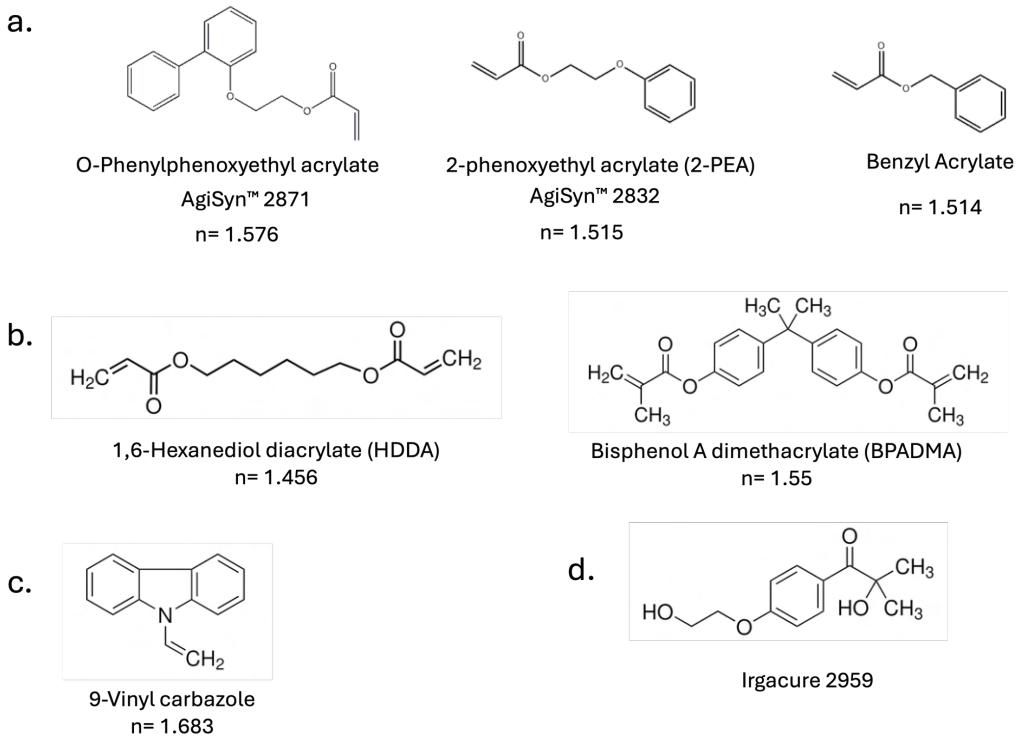

Figure 3.12: Chemical structures of (a)monoacrylate monomers, (b) diacrylate monomers, (c) other high refractive index component, (d) photo initiator, Irgacure 2959. The refractive index information is added under the chemical names.

high refractive indices. However, initial polymerization attempts using only monoacrylates and a photoinitiator resulted in soft, gel-like films without having sufficient mechanical stability. To improve this, I introduced diacrylate monomers into the formulation. Diacrylates, which contain two reactive acrylate groups, are cross-linkers that facilitate the formation of a three-dimensional polymer network during curing. This cross-linked structure provides rigidity and robustness to the final polymer film. Initially, I maintained a weight ratio of monoacrylate to diacrylate at 9:1. This ratio, of course, must be adjusted to optimize the desired working viscosity, while ensuring a high refractive index and transparency under UV light when viewed with a UV-only camera. The photoinitiator was added at 1 wt%, and chosen carefully based on its spectral characteristics. Since transparency in the target wavelength is essential, I screened several options and ultimately selected Irgacure 2959, a photoinitiator

Table 3.1: Summary of the liquid precursor formulations to be used as a binder alternative to NOA160. The measured refractive indices (n) of each mixture, determined using an Abbe refractometer.

Mixture	Acrylate monomer	Diacrylate monomer	Another monomer	Photo Initiator (1%wt.)	Refractive Index (n)
A (9:1)	AgiSyn™ 2832 (n= 1.515)	BPADMA (n= 1.55)	-	Irg. 2959	1.524
B (9:1)	AgiSyn™ 2871 (n= 1.576)	BPADMA (n= 1.55)	-	Irg. 2959	1.576
C (8:1:1)	Benzyl acrylate (n= 1.514)	BPADMA (n= 1.55)	9-Vinyl carbazole (n=1.683)	Irg. 2959	1.537
D (6:3:1)	Benzyl acrylate (n= 1.514)	BPADMA (n= 1.55)	9-Vinyl carbazole (n=1.683)	Irg. 2959	1.571

with absorbance in the deep UV that exhibits non-yellowing behavior upon polymerization. To evaluate the optical suitability of these new formulations, I first measured the refractive index of each liquid precursor mixture using an Abbe refractometer. Table 3.5.1 summarizes the chemicals components with ratios, and measured refractive indices.

Following refractive index measurements, I polymerized the mixtures into thin films and compared their appearance and transparency under UV illumination to that of a cured NOA160 film of the same thickness (0.7 mm). Using a UV-only USB camera, I qualitatively evaluated their optical transparency. From the images in Figure 3.13, it is evident that while NOA appears pitch black to UV-only camera under UV illumination, the other binder formulations are transparent to the camera. This indicates that these alternatives are promising candidates for UV-range applications. Additionally, unlike NOA, these formulations are significantly more fluid and therefore do not require dilution with solvents to adjust their viscosity.

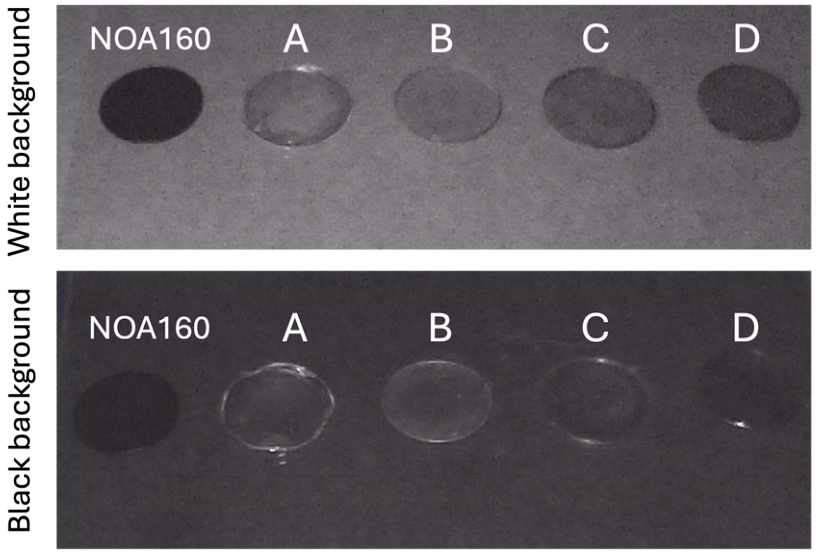

Figure 3.13: Macroscopic images of polymerized binder formulations that prepared as circular patches (each 0.7 mm thick) under UV illumination using a UV-only USB camera. For comparison, a cured NOA160 film of the same thickness was included.

Limitations of the UV-Compatible Optical Components

Due to the limited commercial availability of optical components tailored for the UV range (such as circular polarizers and beam splitters), I explored an alternative route to prepare my UV circular polarizers using polymerized UV reflective CLC films. The key idea is to use the same CLC mixtures used for preparing the UV-retroreflective CSRs, thereby ensuring the spectral overlap within the UV range. Figure 3.14a shows the UV–visible absorption spectra of polymerized CLC films produced with mixtures varying in chiral dopant concentrations, 2.5%, 2.6%, and 2.7 wt%, respectively. I used these measurements to identify the polymerized CLC film to be used as circular polarizers.

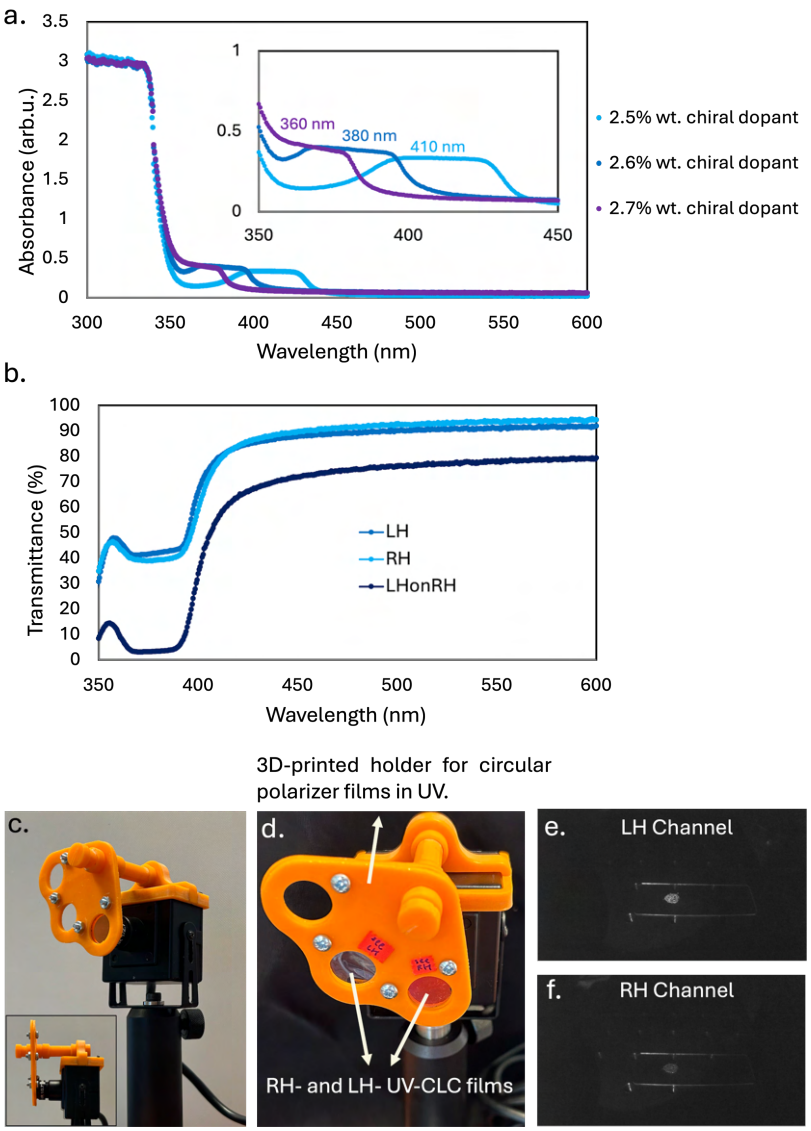

Figure 3.14: a) UV–visible absorption spectra of polymerized CLC films prepared with mixtures varying in chiral dopant concentrations (2.5%, 2.6%, and 2.7% wt). The mixture with 2.6% chiral dopant was selected to be used as circular polarizers in UV range due to its reflection band centered around 380 nm, matching our target UV illumination and imaging range. (b) Transmission spectra of LH- and RH- polymerized CLC films made with the mixture containing 2.6% wt. chiral dopant, along with a measurement of both films stacked together to confirm minimal transmission due to their complementary handednesses. (c) Custom-designed, 3D-printed holder for mounting UV-CLC films in front of a UV-only camera. The design allows rotation between LH and RH filters without shifting the camera; inset shows a side view highlighting how the polarizer sits flush against the camera lens. (d) Assembled imaging setup with the UV-only camera, film holder, and mounted UV-CLC films. (e–f) UV-CSRs in air imaged using this setup through (e) the RH circular polarizer and (f) the LH one.

I decided to use the films produced by a 2.6 wt% chiral dopant mixture as those films exhibit a retroreflection band centered around 380 nm, matching our target illumination and detection wavelength range. To validate the optical functionality for both LH- and RH-polymerized CLC films prepared from the 2.6 wt% mixture. As shown in Figure 3.14b, when LH and RH films are stacked on top of each other, the overall transmission drops to nearly zero, confirming the successful fabrication of polarization-selective films. This is due to the selective reflection of CLC: LH-CLC films reflect LH circularly polarized light while transmitting RH light, and vice versa. As a result, LH-CSRs are visible when viewed through an RH-CLC film, while RH-CSRs are visible through an LH-CLC film. To avoid confusion, I labeled the LH and RH channels on the setup. To enable imaging through these ”homemade” UV circular polarizers, we designed a custom 3D-printed mount together with an undergraduate intern, Rebecca Warga. This mount consists of three circular frames that allow sequential imaging of the same scene through LH and RH circular polarizers, as well as without any polarizer, using a single camera without misalignment or image shift. The mechanical design ensures that the films are fixed firmly in place directly in front of a camera lens (see panels c-d in Figure 3.14), while still allowing for smooth manual rotation between frames when needed. Figure 3.14(e–f) shows the images of UV-CSRs in the air captured using the UV-imaging system in panel (d) when viewed through LH and RH circular polarizers.

As a further step in this study, I aim to demonstrate the functionality of the UV imaging setup using a newly prepared batch of UV-retroreflective CSRs embedded in the alternative binder formulations introduced in the previous subsection. This integration enables the evaluation of refractive index matching and optical clarity in practical conditions, directly observed through the homemade UV circular polarizers. Notably, while NOA glue is unsuitable for UV transparency due to strong absorption at the target wavelengths, I propose repurposing this limitation as an opportunity. By using NOA to make a mold template with UV-CSRs embedded in UV-transparent alternative binders, the NOA functions as an absorbing background that enhances contrast between LH and RH polarization channels during detection. This design is expected to facilitate clear visualization of encoded patterns in the UV range.

Although we initially envisioned a fully automated, continuously rotating polarizer mechanism, the current design offers sufficient flexibility for the optimization of individual components within the UV imaging setup. This implementation demonstrates a practical, low-cost solution for UV circular polarizers, leveraging the same materials already used in CSR fabrication and paving the way for further development of a detection setup for the UV range.

Chapter 4

Enhancing the Color Saturation and Detection Contrast of CSR Markers

4.1 Integrating Nature-Inspired Absorption to Enhance Structural Color Saturation

Artificial structural colors offer a way to create vibrant colors without using traditional dyes or pigments. However, many systems still face important limitations. They often appear pale unless the material is surrounded by an index matching binder [75, 74, 33, 33] and is placed on a black background [76, 77, 73, 78], and color changes with viewing angles. These challenges limit their use in real-world applications, especially where lighting or background conditions can't be easily controlled. However, in nature, we often see examples where these issues are resolved. For example, in jewel scarab beetles, a cholesteric arrangement of chitin reflects circularly polarized light to create color. Thanks to the continuous curving arrangement of the helix orientation in these beetles, the reflected color stays independent of viewing angle [79, 69]. We can already mimic the angle-independent color reflection found in beetles by shaping CLCs into spherical shells. However, as I demonstrated in Chapter 4, when we compared the visibility of CSR markers with jewel beetles over increasing distances, nature was far ahead of us in terms of contrast. The reason for this is that most

species with very bright colors, which are mainly generated from periodic nanostructures, also contain pigments in their structures that act as broadband absorbers [32, 80, 81]. Studies showed that these pigments, such as melanin, help enhance the visibility and richness of the structural color by absorbing scattered light. For instance, the vivid metallic blue of the Morpho butterfly is due to interference effects created by nanostructures on its wing scales, which also contain melanin [30]. The absorption of melanin increases contrast and makes the reflected color appear more intense. In the velvet satin bowerbird, a thick melanin layer underneath a keratin-based surface results in a deep violet-blue appearance [31]. Likewise, in scarabaeid beetles, an underlying melanin layer enhances color vibrancy [82]. Because melanin absorbs light across the entire visible spectrum, it serves as a natural black background, amplifying the brightness of structural coloration.

Several previous studies have demonstrated that integrating strong broadband absorbers into photonic structures can significantly suppress unwanted optical artifacts, enhance the visibility and saturation of artificial structural colors. Cong et al. reported the enhancement of structural color in artificial opals by incorporating carbon black nanoparticles into the voids of monodisperse polystyrene (PS) colloids. The resulting coatings exhibited significantly improved color saturation and more vivid structural colors compared to the original white PS opals. Carbon black helped suppress background scattering, improving contrast and enhancing color visibility. Furthermore, they presented the tunability across the visible spectrum via changes in particle size. However, this study only discusses flat films, so iridescence is strong, meaning the structural colors are varied with the angle of observation [83]. A similar bioinspired approach was adopted by Kohri et al., where they developed films of biomimetic core–shell particles with a polydopamine (PDA) shell layer on polystyrene (PS) core particles. The PDA layer mimics the function of melanin in nature, effectively absorbing the scattering light. Their films exhibited intense, saturated colors that remained visible even against white backgrounds, offering promising potential toward structural color-based ink materials with enhanced colors [70].

In the context of CLC systems, Belmonte et al. presented a method to fabricate angular-

independent multicolor reflective coatings using CLC beads by incorporating a reactive dye with an absorption peak between 450 and 600 nm. In this study, the authors aimed to suppress the undesired blue and green cross-communication signals that compromise color purity. By incorporating the dye directly into the droplet network, they were able to effectively minimize the blue-green wavelengths in the reflection band. While their results demonstrated that the coatings have saturated structural colors, particularly for green and red-reflecting ones, the enhancement was characterized primarily on black backgrounds and the beads were always embedded in an index matching binder. The study did not address whether this saturation effect is background-independent. Nevertheless, the work is highly promising as it clearly shows the potential of dye absorption to boost color saturation in CLC-based coatings [74].

Inspired by nature and guided by the designs in literature, this chapter explores how dye-doped CSRs (d-CSRs) can integrate high-saturation structural color to CSR-based patterns without compromising the polarization-selective reflection. The approach involves absorbing unwanted scattering using a black dye, similar to how melanin functions in beetles, and thereby enhancing the retroreflective signal from the CSRs. Additionally, by tuning the cholesteric pitch and using different dye concentrations, a wide color palette that is independent of the background and observation angle can be designed.

4.2 Preparation of dye infused CSRs (d-CSRs)

Previous studies in our research group demonstrated that adding Sudan Black dye to cholesteric liquid crystal elastomer (CLCE) sheets [84] and fibers [85] significantly enhances the colors and contrast, particularly on bright backgrounds. The question was how could I integrate the dye absorption into my CSR system and increase the color saturation of CSRs? I considered two possible approaches. The first was to add the black dye directly during the mixture preparation and use this dye-doped CLC mixture to produce shells. Before the shell production, I prepared a series of polymerized films using a dye-doped mixture and compared the effect of dye concentration on color contrast and intensity with films prepared using a regular

CLC mixture. Although these films had intense colors, I could not succeed in my attempts to produce stable shells by using the dye-doped CLC mixture. I encountered the problem of shells being unstable and popping immediately after the collection in the bottle. Then, I followed a much simpler method as in the work of Geng et al.[85]. In this method CLCE fibers are infused with black dye by simply soaking the fibres in a solution of Sudan Black. This approach offers a quick and easy-to-apply method that will not interfere with the shell production.

Before conducting the controlled dye infusion of CSRs, we first produced spherical shells of reactive CLC mixture that varied in the ratio of chiral dopants, solidified the shells by photopolymerization, and followed the washing steps described as Geng et al.[35] up to obtaining punctured solid CSR shells with high optical quality in different retroreflection wavelength. It is important to note that each solidified shell has a hole that will be useful for future processes, including the dye infusion and embedding with a binder to create patterns with CSRs. On the other hand, we should carefully carry out the washing, the solvent exchange, and the mixing steps to avoid introducing air into the shells so as not to cause random scattering later. That is why, the strategy for the rest of the study is never to let the shells dry. After the washing steps are complete, the shells are in the water. Before starting the dye infusion, we need to do a solvent exchange as the Sudan Black dye is insoluble in water and water will cause the dye to coagulate as big chunks. Here in dye infusion experiments, my purpose was to develop a protocol that the dye goes into the shells by the swelling of the polymer with the solvent of the dye mixture. Then only the excess amount of the dye that is precipitated on the outside of the shells is washed away. That is why the proper solvent choice at each step is of great importance for the successful infusion of the Sudan Black into the CSRs. In this study, I used acetone as a solvent for the dye infusion as it both dissolves the Sudan Black dye and swells the polymer, allowing the dye to go into the shells along with the swelling.

Figure 4.1 shows the reflection spectra and the reflection mode POM images of polymerized CLC films. I followed the same washing steps as in the CSR production: I polymerized

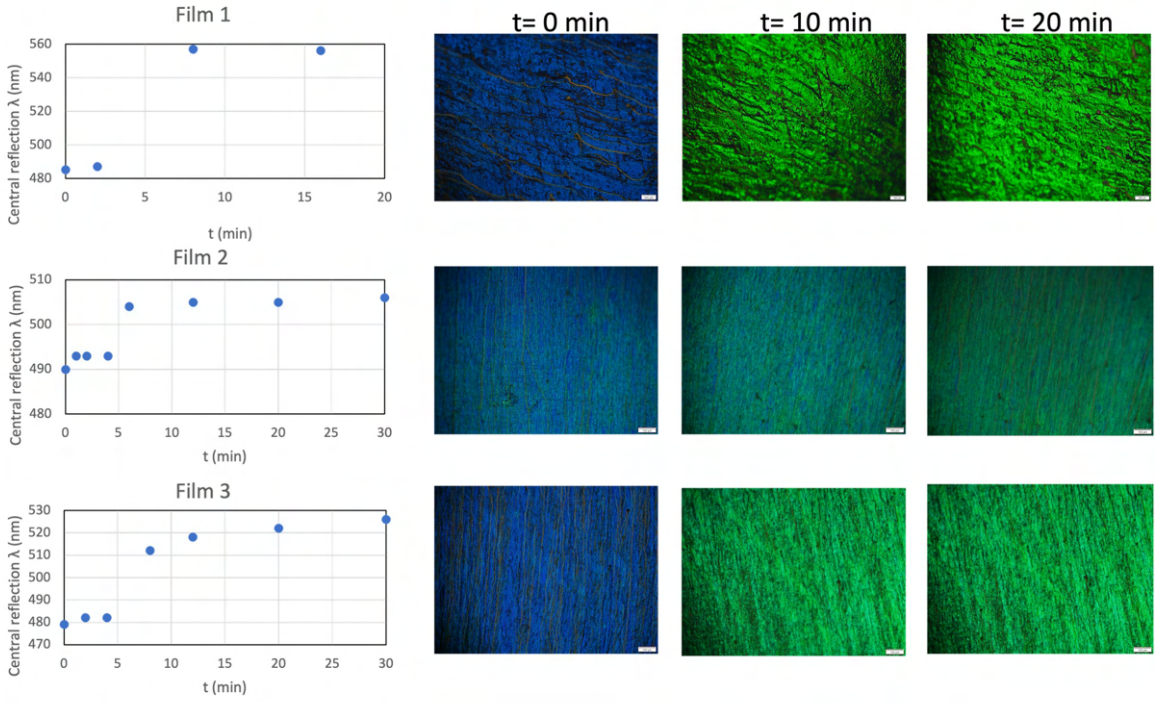

Figure 4.1: Swelling behavior of polymerized CLC films in acetone. (a) Reflection spectra of three identically prepared polymerized CLC films during immersion in acetone, showing the red-shift of the reflection peak over time due to solvent-induced swelling. All films were fabricated from the same CLC mixture prepared in separate LC cells (2 cm × 1 cm, planar aligned and 20 μm thick), polymerized for 10 minutes under UV, and subjected to identical washing steps (water, acetone, water). At t=0, the films had already been dried after washing. Upon immersion in acetone, the reflection peak gradually red-shifts, stabilizing after 20 minutes, indicating equilibrium swelling. (b) Reflection-mode POM images corresponding to the spectra in (a), highlighting visible color changes during swelling. Images were captured at regular intervals for three films to confirm reproducibility. The most pronounced color changes occur in the first 20 minutes. Scale bars: 200 μm. All films were immersed in 5 mL of acetone in identical petri dishes.

the films for 10 minutes, then washed them with water, acetone and water respectively. I then immersed the washed and dried films in acetone to monitor the swelling behavior and collected microscope images and reflectance spectra at regular intervals during immersion. Initially, the central reflection peak of the polymerized films was at 600 nm. In Figure 4.1a at t=0, films are already washed and dried. The reflection peak is shifted to 480-490 nm as a result of the removal of the unreacted monomers and nonreactive chiral dopant. The

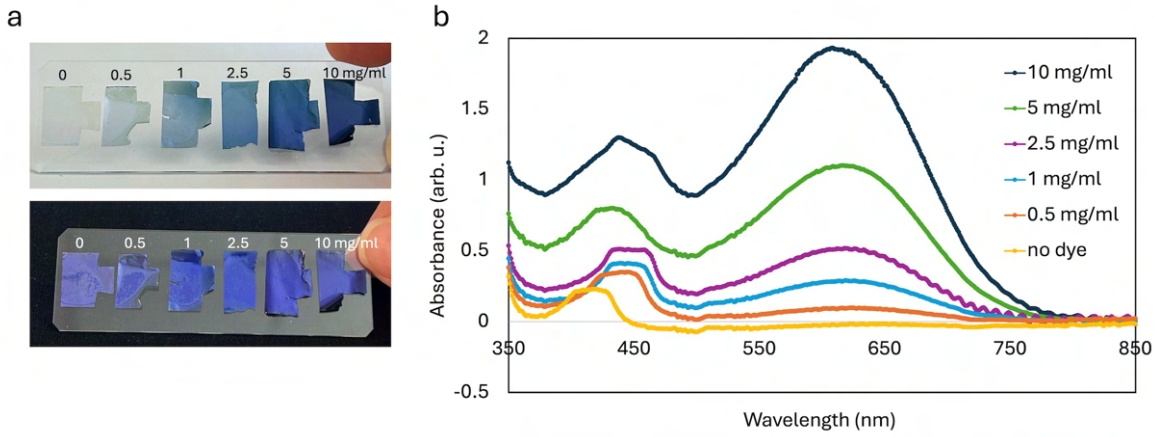

Figure 4.2: (a) Macroscopic images of blue retroreflecting CLC films infused with varying concentrations of solution of Sudan Black dye in acetone (0.5, 1, 2.5, 5, 10 mg/ml), alongside a control sample that was only washed and dried after polymerization. Samples are photographed on both black and white backgrounds under ambient light at a slight angle to avoid specular reflection. (b) Corresponding absorption spectra of the same films.

moment the dried films immersed into acetone, the reflection peak is starting to red-shift due to polymer swelling by acetone. The POM images prove that the most significant change in color and the optical response occurs in the first 20 minutes of swelling. After that, the reflection color did not change much, indicating that the swelling process has reached a near-equilibrium. Following this observation, I prepared a blue reflected CLC film, cut it in half and immersed one half in a saturated solution of Sudan Black dye in acetone (20 mg/mL) [86] for 30 minutes. I then rinsed the films with ethanol to remove excess dye from the film surface. However, using the dye at such a high concentration caused the dye absorption to dominate over the Bragg reflection of the films, resulting in black films instead of color-enhanced ones. Figure 4.2 presents the optimization of the dye concentration by showing the blue-reflecting CLC films after infusion with various concentrations of dye solution in a controlled manner, alongside a film that was only washed and dried after production. The results confirmed that the dye-infused films retained their color, and ethanol effectively removed only the dye accumulated on the surface while preserving the dye infused in the polymer network.

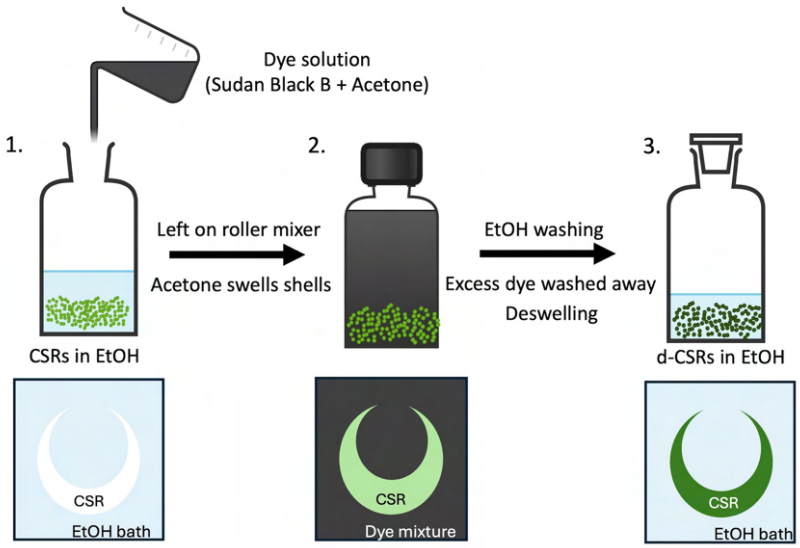

Figure 4.3: The schematic illustration of the steps of dye infusion process.

I started the controlled dye infusion process of CSRs by first exchanging the water medium with ethanol. There are several reasons for this. Firstly ethanol is known as a deswelling agent preventing the polymer from swelling before we add the dye solution. Ethanol also dissolves the Sudan Black dye, so it does not cause the dye to coagulate during the process. Figure 4.3 schematically illustrates the infusion process. The first step is to add the dye-in-acetone solution to the CSR suspension in ethanol and then to leave the batch overnight on a roller mixer to carry out the infusion. The shells swell with acetone, and the dye is infused into the polymer network through this swelling. The final step is rinsing CSRs with ethanol to remove excess dye from the surface of CSRs, and obtain our dye-infused CSRs (d-CSRs).

4.3 Optical characterization of d-CSRs

4.3.1 Macroscopic Optical Appearance of d-CSRs

To investigate the effect of dye infusion on the optical properties of the shells, I prepared circular 2D patches (or sheets) of closely packed CSRs surrounded by air. I also prepared two control samples of regular CSRs without dye infusion: one surrounded by air and the

other embedded in NOA160. The latter was then UV-cured into a solid state. To prepare the 2D patches, I used a plastic pipette to drop a small volume of the CSR-in-ethanol suspension onto a glass slide, keeping the pipette tip in contact with the glass surface to ensure central deposition of CSRs. As the ethanol evaporated, I gently guided the CSRs toward the center using a metal spatula, resulting in a closely packed circular arrangement. Figure 4.4 presents the set of images showing a glass slide with patches of CSRs with four different retroreflection colors: blue (B), green (G), yellow (Y), and red(R). I took six photos for each color using a DSLR camera (Canon EOS 77D), three on white paper and three on black fabric as two extreme conditions to observe the background influence on contrast and color intensity of CSRs. Within each set, the first column shows the samples under ambient illumination viewed at a normal incidence of 0°, the middle column is under ambient illumination viewed at 45° with respect to the sample normal, and the third column under retroreflection illumination only from a ring-shaped light source around the camera (i.e. the ambient light is turned off), ensuring identical illumination and observation directions, both at 45°. This layout repeats for each color group.

The second circular patch in each row, representing the 0 mg/mL dye concentration, appears white, regardless of the retroreflection color of the CSRs, lighting condition, viewing angle, or background on which the samples are placed. This whiteness results from strong random light scattering by the air-surrounded CSRs without index matching binder. On the other hand, the index-matched CSRs corresponding to the first circular patch of each sample appear nearly invisible on a white background, under all viewing and illumination conditions. In this case, only the circular boundary of the 2D patch is perceived due to the specular reflection and diffraction at the edges of the NOA glue. However, when the same index-matched sample is viewed on a black background, we see that the 2D patches of B-CSRs are clearly colored, but the color saturation is rather poor for G-, Y-, and R-CSRs. The noticeable difference in the NOA-surrounded samples on the black background is observed under the retroreflection illumination: the samples show saturated colors, but surprisingly only in blue and green tones. In contrast to the regular shells, and remarkably, even at the lowest dye infusion concentration, the d-CSRs exhibit a highly saturated color that remains independent

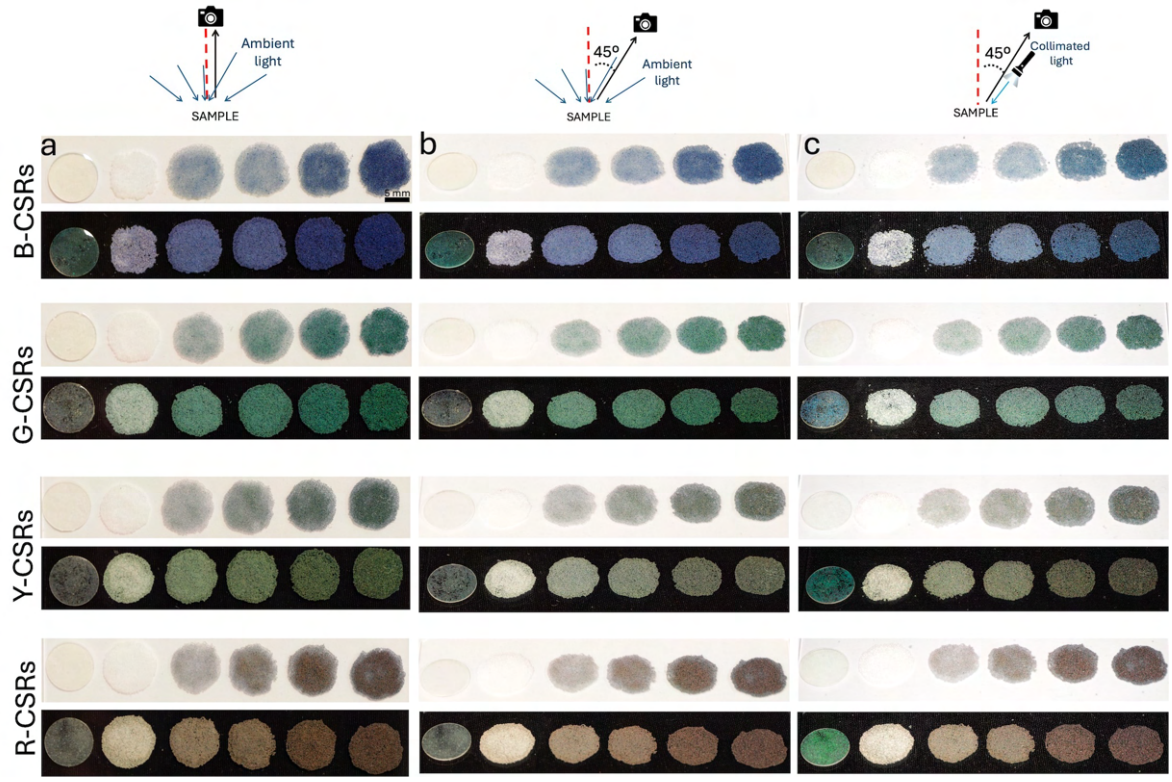

Figure 4.4: Macroscopic images of B-, G-, Y- and R-CSRs as densely packed 2D patches placed on a white paper and a black cloth captured with a) diffused light at 0°, b) diffused light at 45°, and c) collimated light at 45°. The leftmost patch is regular CSRs in NOA160 and the subsequent patches to the right show CSRs in air infused with dye-in-acetone solutions with concentrations of 0, 0.5, 1, 2.5, and 5 mg/mL, respectively.

of both viewing angle and background color. We attribute this effect to the black dye absorbing all the randomly scattered light, resulting in an intense, saturated color, surprisingly achieved even without the need for an index-matching binder. In fact, NOA glue also suppresses scattering through refractive index-matching but alone does not provide sufficient color visibility. To improve color perception, we are required to place the index-matched samples on a black background. This is precisely why many studies on CLC-based photonic structures and bio-inspired structural colors in the literature are demonstrated on black backgrounds so that a black substrate provides contrast by absorbing light, minimizes background reflections, and enhances the reflected light originating from the reflector sample.

4.3.2 POM Characterization of d-CSRs

Following the analysis at the macroscopic level, I studied the samples of 2D circular CSR patches on a glass slide using polarized optical microscopy (POM) to better understand the origins of the colors observed macroscopically. I placed the glass slides flat on the microscope stage and the samples were illuminated by white light from above so the light hit the shells with maximum intensity at zero angle of incidence. Figure 4.5 shows the collected

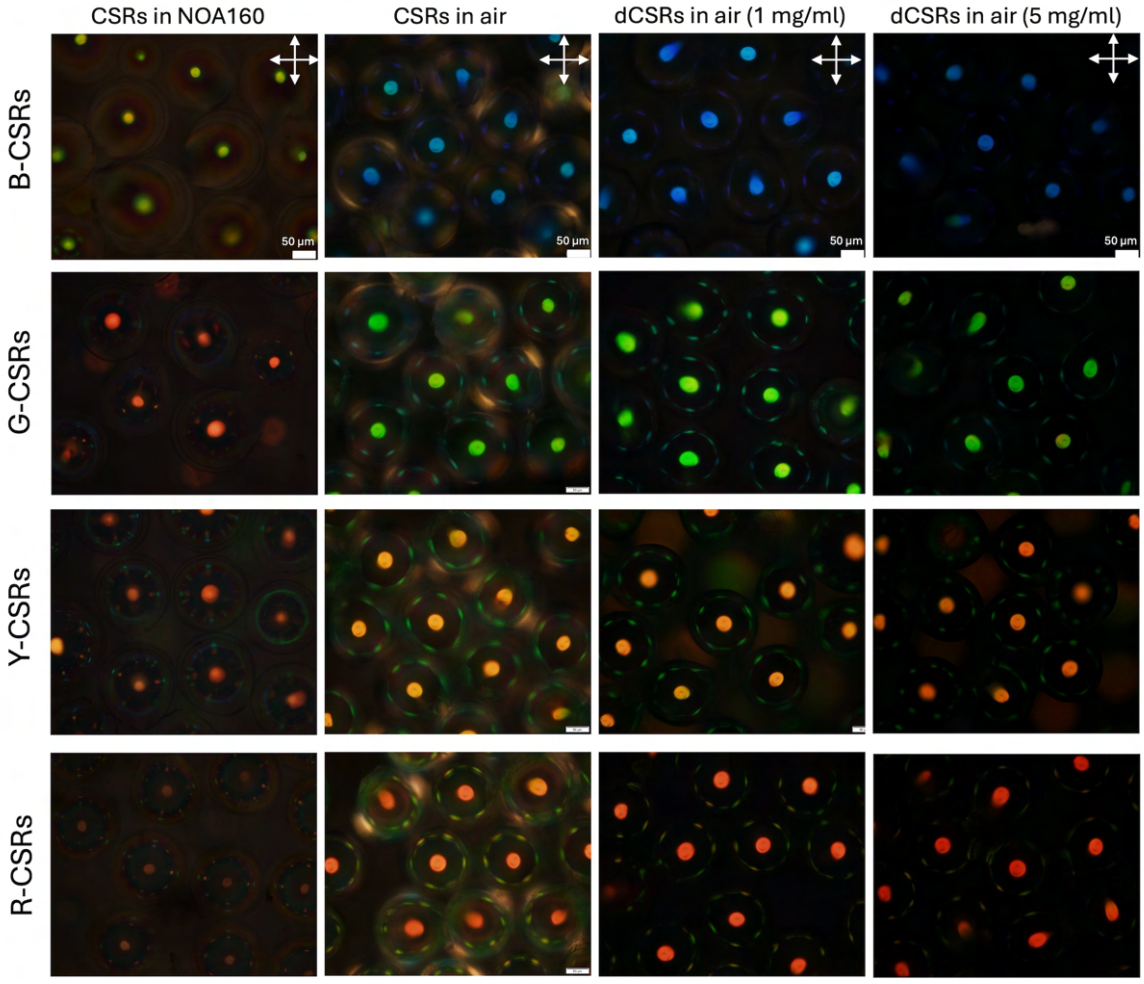

Figure 4.5: Microscopic images of of B-, G-, Y- and R-CSRs taken in reflection mode with crossed polarizer and with a $\lambda/4$ plate inserted. Regular CSRs a) in NOA160, and b) in air; d-CSRs in air c) infused by 1mg/mL , and d) 5mg/mL dye mixture. Exposure settings were kept constant within each medium group (air vs. NOA160) to allow reliable visual comparison.

micrographs of samples in the reflected light microscope with crossed polarizers. The optical appearance of CSRs confirms the radial helix orientation as each shell exhibits a central reflection spot with a color corresponding to the selective retroreflection wavelength at normal incidence. As the chiral dopant concentration decreases, the retroreflection peak shifts toward longer wavelengths, resulting in colors of CSRs ranging from blue to green, yellow-orange, and red. We also observe smaller cross-communication spots with blue-shifted reflections along the perimeter of the shells[38, 40]. The comparison between the central retroflection color observed under the microscope in Figure 4.5 and colors perceived macroscopically in Figure 4.4 reveals that the retroreflection colors in B- and G-d-CSRs match their macroscopic appearance. However, the situation is slightly different for yellow and red retroreflective shells: Y-d-CSRs appear orange microscopically, while R-d-CSRs appear red under the microscope but have macroscopic appearance pink or brown/brick-red depending on the dye concentration. This difference between microscopic and macroscopic color appearance is not trivial to explain, but it is worthwhile to examine the absorption spectrum of Sudan Black dye. Its absorption spectrum in Figure 4.6a reveals that the absorption is lower for blue wavelengths than for red wavelengths, with a minimum absorption of around 500 nm (cyan-green region), and a peak absorption at around 600 nm (orange-red region). This indicates that Sudan Black does not absorb equally across the visible spectrum, and therefore doesn't behave like an ideal black dye. To observe the absorption characteristics clearly, I prepared dye solutions in acetone at relatively low concentrations (0.05, 0.025, and 0.01 mg/ml), as higher concentrations exceeded the detection limits of the spectrophotometer and resulted in saturated measurements. Notably, even the 0.05 mg/ml solution approached the upper limit for accurate absorbance readings. These lower concentrations were used only for spectroscopic clarity and are much lower than the actual concentrations used during the dye infusion of the shells.

Figure 4.6b shows a photo of the patches prepared by drying dye-in-acetone solutions used in the dye infusion process, with concentrations of 0.5, 1, 2.5, and 5 mg/mL, respectively. To provide a visual comparison of their macroscopic appearance prior to infusion, I placed a few drops of each solution onto a glass slide positioned on a white paper background. After

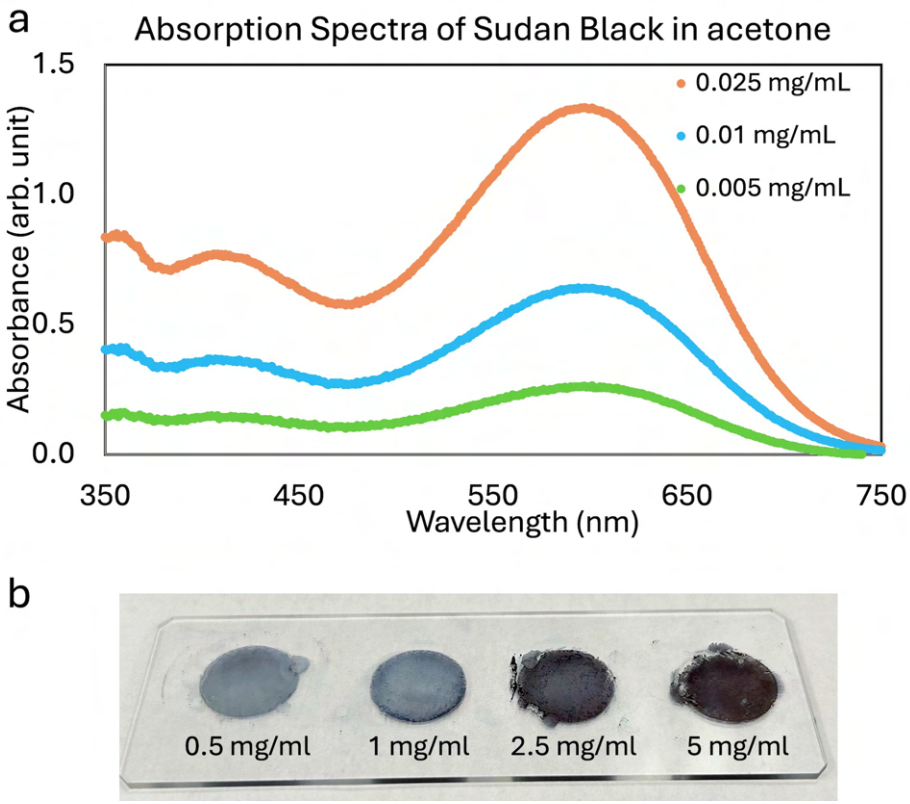

Figure 4.6: a) UV–visible absorption spectra of Sudan Black dye dissolved in acetone at low concentrations (0.01, 0.025, and 0.05 mg/mL). (b) Photographs of dried patches of dye-in-acetone solutions at higher concentrations (0.5, 1, 2.5, and 5 mg/mL, respectively) used in the dye infusion process. Drops of each solution were placed on a glass slide and left to dry so that the remaining dye stains could be visually compared.

the acetone evaporated readily, the remaining circular dye stains illustrate how the visual opacity increases with concentration, giving an indication of how 'black' the Sudan Black dye appears at each concentration. Consequently, the dye contributes to the overall color by selectively absorbing certain wavelengths, particularly in the red-orange wavelengths, and making it challenging to predict the precise color we see macroscopically. Therefore, the colors observed macroscopically are not only determined by Bragg reflection arising from the cholesteric helix but are the result of an additive color system combining structural coloration and dye absorption.

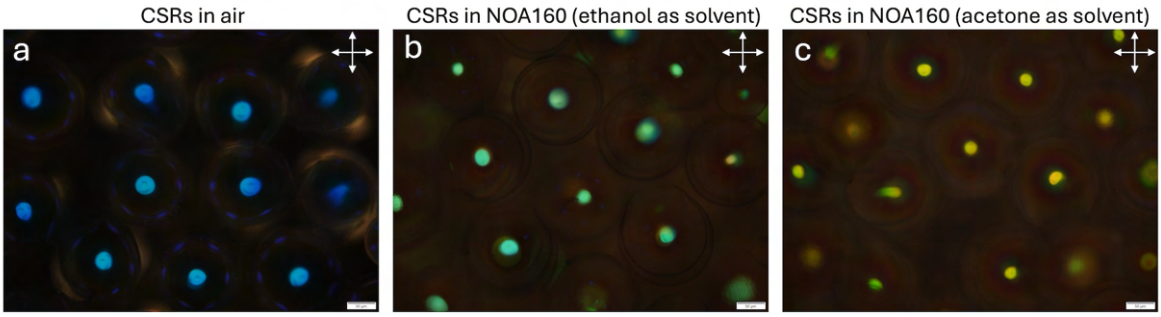

Figure 4.7: Microscopic images of blue-retroreflective CSR samples (a) in air, (b) embedded in NOA160 diluted with ethanol, and (c) embedded in NOA160 diluted with acetone. The air-dried CSRs retain their original blue reflection, while ethanol-diluted samples shift to cyan and acetone-diluted samples shift further to green.

Unlike CSRs and d-CSRs in the air, their NOA160-embedded counterparts consistently exhibit a redshift in POM images, even though all samples with the same color are prepared from the same batch of shells. This redshift is attributed to polymer swelling that occurs during sample preparation. To reduce the high viscosity of NOA160 glue, I dilute it with acetone, a solvent known to swell the polymer. Although acetone evaporates after sample preparation, it facilitates the NOA160 to infiltrate and remain in the network as a swelling agent. As a result, the polymer structure remains swollen, resulting in a red shift in the retroreflection.

This swelling effect is further demonstrated in Figure 4.7, which compares the microscopic images of CSRs from the same blue-retroreflecting batch: (a) in air, (b) embedded in NOA160 diluted with ethanol, and (c) embedded in NOA160 diluted with acetone. The CSRs in air display their original blue retroreflection, while the ethanol-diluted sample shifts to cyan color, and the acetone-diluted sample shows a more pronounced redshift, appearing green. These observations confirm that both ethanol and acetone facilitate the penetration of the binder into the polymer network during sample preparation, but to different extents. Acetone is a stronger solvent that causes significant swelling, allowing more binder to enter and resulting in a more pronounced redshift. Ethanol, on the other hand, is a weaker solvent—often considered an anti-solvent for many hydrophobic polymers. Although NOA is partially soluble in ethanol and some binder still diffuses into the polymer, the resulting swelling and redshift are notably less pronounced than with acetone. We also observed a significant

blue shift in the macroscopic appearance of the CSR sample embedded in NOA160 when comparing retroreflection and ambient light illumination conditions. As I collected the macroscopic images in Figure 4.4c at a 45° angle of incidence under retroreflection illumination, it is necessary to reproduce microscopic images in same conditions, i.e., at a 45° angle of incidence obtained by tilting the sample on a black-painted glass substrate, to better understand the observed color shift. Figure 4.8 shows that the NOA-embedded CSRs viewed with the microscope at a 45-degree angle of incidence are dominated by blue-shifted cross-communication reflections, consistent with the macroscopic images. This blue-shift is not present in d-CSRs or in regular CSRs in the air. Tilting the sample with respect to the light changes the reflection pathways, especially since the samples consist of multilayered CSRs. At oblique incidence, light may pass through multiple shells before reaching our eye or a camera, and the cross-communication patterns becomes more complex.

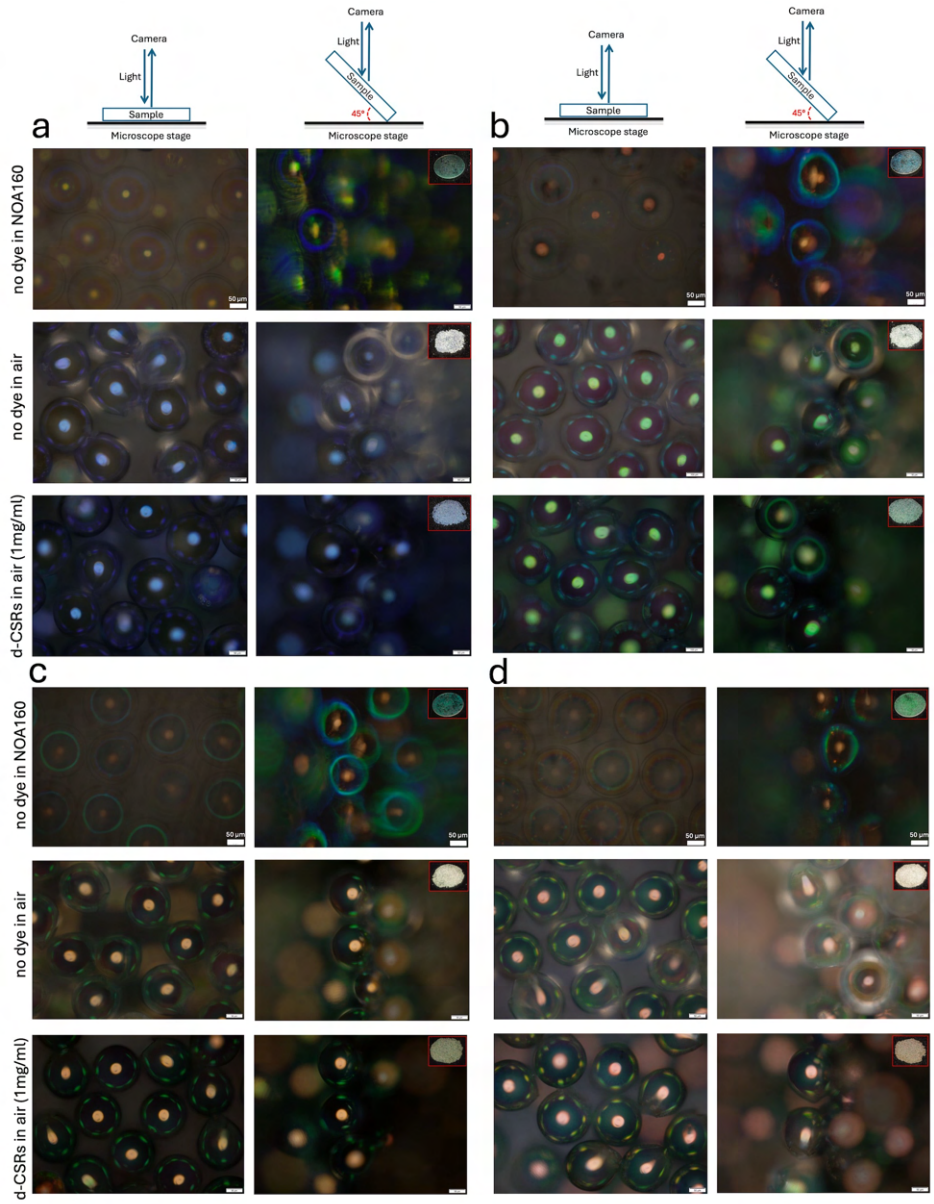

Figure 4.8: Microscopic images showing the viewing angle-independence of the retroreflection color for (a)B-, (b)G-, (c)Y-, and (d)R-CSRs taken in reflection mode without polarizers. Each panel contains six images: the left column shows retroreflection under normal incidence, the right column shows retroreflection with the sample tilted at a 45° angle. The three rows in each panel represent different samples: (top) CSRs in NOA160, (middle) CSRs in the air, (bottom) d-CSRs in the air infused with a 1 mg/mL dye-in-acetone solution. All images were captured in reflection mode without polarizers. Red-framed insets display the corresponding macroscopic appearance of the sample under the same tilted (45°) retroreflection illumination condition. Scale bars: 50 μm.

The hypothesis is that the reflection pathways for the transparent samples (CSRs in NOA160) involve transmission and refraction, and those pathways are blocked by the absorption of black dye for d-CSRs. As a result, we see a color shift for NOA-embedded CSRs, but the same color for d-CSRs in the air. Another hypothesis is that the orientation of the shells with respect to the light source contributes to the color shift in NOA-embedded CSRs. During sample preparation, NOA160 glue is diluted with acetone to reduce its viscosity, allowing easier dispersion of CSRs. As the acetone evaporates, the medium gradually becomes more viscous. In this transition, CSR shells, being asymmetric in geometry with a thinner top, thicker bottom, and an opening at the top, likely orient themselves in response to the impact of gravity. This typically results in the opening settling to the side or upward. Due to this preferred orientation, when the sample is tilted, the chance of light entering the shell increases, altering the reflection pathways and contributing to the observed blue-shifted color under angled retroreflection.

4.3.3 Spectrophotometry Analysis

Up to this point, we have characterized the shells based on their microscopic and macroscopic appearance. However, to quantify these observations, we also performed spectrophotometry analysis. As shown in the Figure 4.9, while the dye concentration does not cause a noticeable shift in the reflection wavelength, a clear red-shift is observed in the reflection spectra of samples embedded in the binder. The data represent the reflection spectra of a single shell from each dye concentration.

Although these initial results were sufficient to obtain reflection wavelength data, statistically meaningful analysis was required to investigate whether there is a correlation between dye concentration and reflection intensity and/or the central reflection peak wavelength. Therefore, I repeated the measurements collecting reflection spectra from 10 blue (B-CSR) and 10 green (G-CSR) shells for each concentration. I expected the peak intensity to decrease slightly with increasing dye concentration, as higher dye content would absorb more of the incoming light. Interestingly, most spectra, except those from NOA-embedded CSRs, ex-

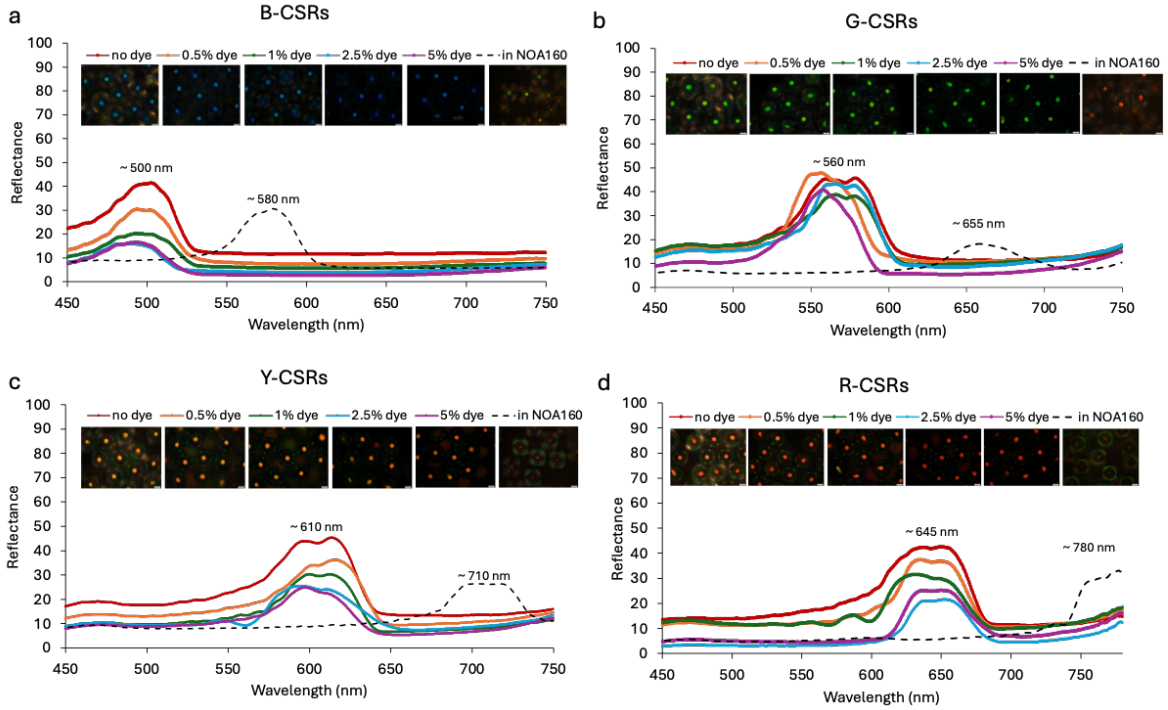

Figure 4.9: POM and spectrophotometry characterization of (a) B-, (b) G-, (c) Y-, and (d) R-CSRs in air with increasing dye concentration (0 mg/mL to 5 mg/mL). Insets show corresponding reflection mode POM images in crossed polarizers.

hibited double-headed peaks, while NOA samples have smoother, more symmetric peaks. To better understand this behavior and to determine the effect of dye concentration on the reflectance, I performed data fitting using Lorentzian functions, analyzing how the peak parameters such as the amplitude and the central wavelength varied with dye concentration. However, I could not establish a consistent or meaningful correlation between the peak characteristics and dye concentration. As shown in the Figure 4.10b, the amplitude of the fitted Lorentzian peaks remained relatively constant across different dye concentrations.

Additionally, I observed that even slight changes in the alignment of the shell's central reflection spot or adjustments in the focus could significantly affect the recorded spectrum. This observation motivated a follow-up experiment in which my colleague Dr. Vijaykumar Varma and I designed a setup to rotate individual CSRs under the microscope while collecting reflection spectra and corresponding microscope images from multiple perspectives of

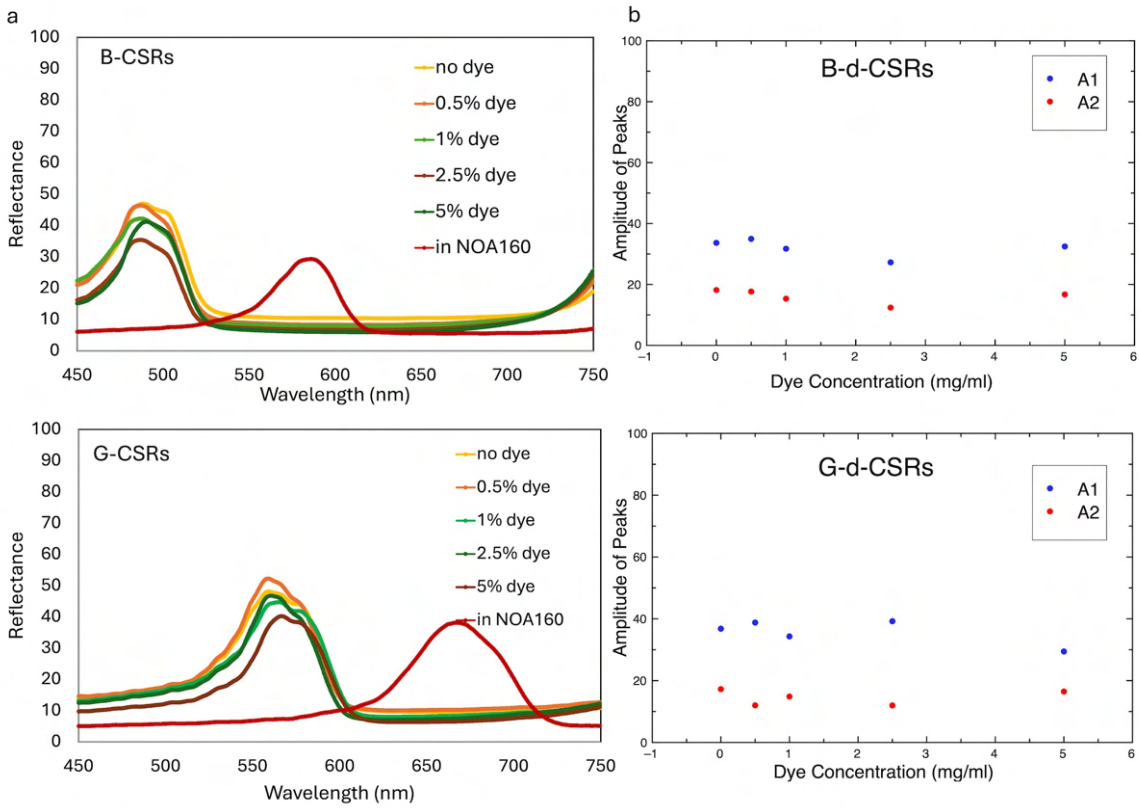

Figure 4.10: (a) Spectrophotometry characterization of B-, and G-CSRs in air with increasing dye concentrations (0 to 5 mg/mL). The 0 mg/mL samples (no dye) were treated with acetone during the post-polymerization washing process, but unlike the d-CSRs, they were not soaked overnight in dye-in-acetone solutions. All samples were subsequently rinsed with ethanol for the same duration before being drop-cast onto glass slides using a plastic pipette. Ethanol was allowed to evaporate prior to measurement. The CSRs in NOA160 were measured as well to highlight differences in optical response due to both dye infusion and binder embedding. (b) The comparison of the amplitude of the fitted Lorentzian peaks as a function of the concentration of dye solution.

the same shell. The aim of this experiment was to better understand the sources of spectral variability and systematically investigate whether orientation-dependent changes occur.

For this purpose, I used a round borosilicate glass capillary with an inner diameter of 0.2 mm, just wide enough to fit a single shell. The refractive index of borosilicate glass is approximately 1.46, which I matched using glycerol (n = 1.47), filling both the inside and outside of the capillary, as well as the inside of the shell CSR. This minimizes refraction and reflec-

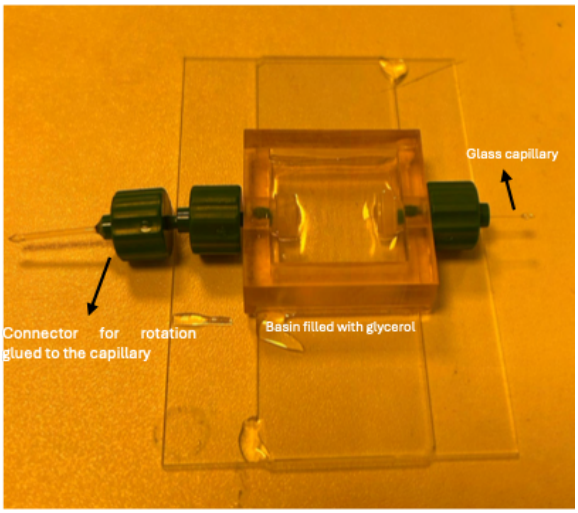

Figure 4.11: The experimental setup designed to rotate the glass capillary tube containing the shells.

tion artifacts due to refractive index mismatch, approximates normal incidence, and allows us to get cleaner images and spectra. The shells were initially suspended in ethanol and then mixed with glycerol, the ethanol was evaporated afterwards. Because of glycerol's high viscosity (1.412 Pa·s @20 ℃), loading the CSRs-glycerol mixture into such a narrow capillary was challenging. To overcome this, I heated the glycerol to reduce its viscosity [87], then used the capillary as a pipette, and filled the mixture into the capillary by applying a squeeze-release motion with an attached rubber bulb. After filling, I sealed both ends of the capillary with glue to prevent leakage. The high viscosity of glycerol became an advantage during the experiment because it prevented the shells from moving during capillary rotation, providing a suitable medium for the experiment.

The setup includes a custom-designed 3D-printed basin that allows the glass capillary to be immersed in glycerol and rotate freely. As shown in Figure 4.11, two soft stoppers close openings of the basin at the inlet and outlet points of the capillaries to prevent leakage, along with several connectors to keep the capillary straight yet allow controlled rotation. Using this setup, I successfully collected both reflection spectra and microscope images of the same shell at different orientations relative to the camera and the microscope's illumination.

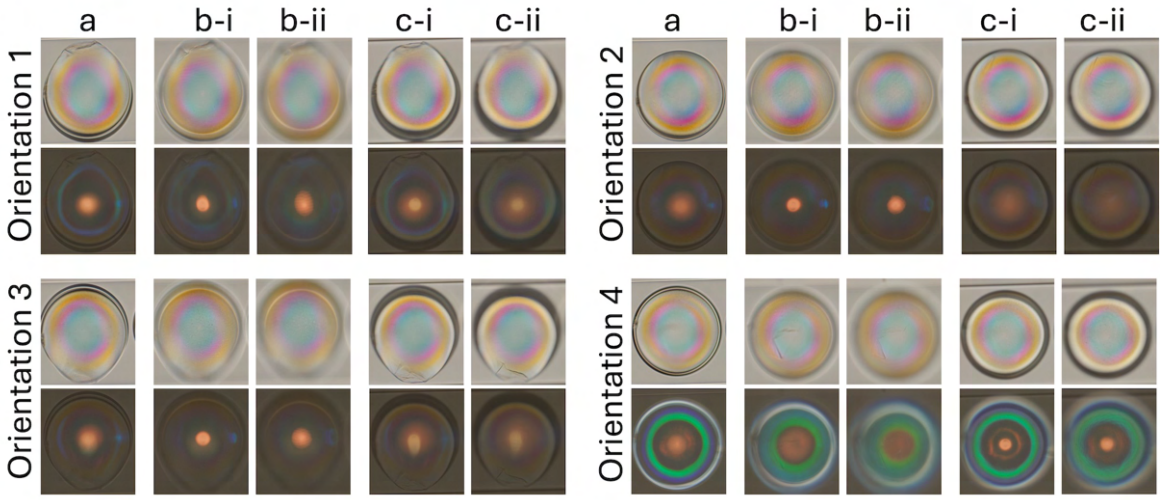

Figure 4.12: Microscope images of an R-CSR placed inside a borosilicate capillary with 0.2 mm inner diameter (ID) taken under four rotational orientations and five different focal positions (columns a, b-i, b-ii, c-i, c-ii). The glass capillary is rotated 90° between each orientation. In orientations 1 and 3, the shell opening is lateral. Orientation 2 corresponds to the CSR opening facing downward, while orientation 4 has the opening facing upward. In each orientation, the top row shows transmission mode images, and the bottom row is in reflection mode. Focus positions are as follows: (a) shell equator, (b-i and b-ii) above the equator, (c-i and c-ii) below the equator. Scale bars: 50 μm

Figure 4.12 shows microscope images of a red retroreflective CSR taken at four distinct orientations (labeled as 1–4) and five different focal planes (columns a to c-ii). As previously discussed, when collecting reflection spectra of the shells, the spectrophotometer captures only a small portion of the central reflection spot. The CSR shown here has a diameter of approximately 150 μm. For all orientations, the incidence angle is at 0° (normal incidence), as the capillary was placed horizontally and flat on the microscope stage. During the imaging, I rotated the capillary in 90-degree increments and collected images at each orientation. In orientations 1 and 3, the side of the CSR faces both the camera and the light source, with the shell opening directed laterally. In orientation 2, the CSR opening faces downward, while in orientation 4, the opening faces upward, directly toward the camera. For each orientation, the top row shows the transmission mode images, and the bottom row shows the reflection mode images. The five columns correspond to different focal planes: (a) focused at the

equator of the shell, (b-i) and (b-ii) focused above the equator, and (c-i) and (c-ii) below it. These images illustrate how subtle changes in focus and orientation significantly affect the perceived appearance (size, brightness and color) of the central reflection spot. To demonstrate how these visual differences appear in the spectrum, I collected reflection spectra of the same CSR measured at three focal planes—the equator, the upper surface, and the lower surface—for each of the four orientations.

Figure 4.13 shows, at first glance, that even for the same shell and in the same binder environment, varying only the orientation or the focus leads to a significant difference in the intensity of the reflection band. Notably, the observed spectral variations are not random but correlate with the underlying unique geometry of the CSR and the optical pathways involved in Bragg reflection. Looking first at the first three orientations, the reflection spectra

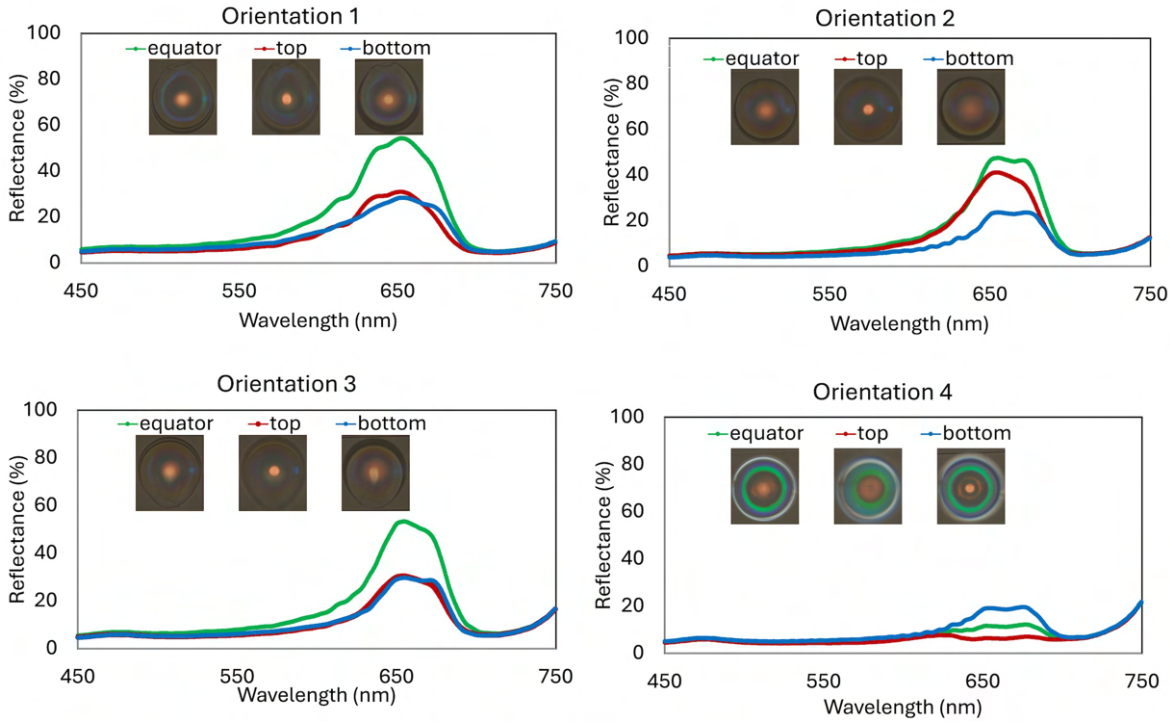

Figure 4.13: Reflection spectra of a single R-CSR measured at three focal planes (equator, upper surface, and lower surface of the CSR) across four distinct orientations. Insets in each graph show the corresponding microscope images at the related spectral acquisition. Scale bars: 50 μm.

consistently show the highest peak intensity at the equatorial focus of the CSR, despite the absence of liquid crystal material at this geometrical center of the shell (this region is filled with glycerol in this experiment). The equatorial focal plane collects reflected light through a maximal optical path through radially arranged helical twist, leading to stronger constructive interference and thus reflectance. Additionally, a lensing effect may contribute: due to the spherical symmetry, refracted and reflected light rays converge near the equatorial focus, amplifying the measured reflection signal.

Interestingly, despite this spectral trend, the microscope images show that central reflection spot appears the sharpest when focusing on the top surface. Light coincides with the material interface in this upper focal plane. There is a true reflection from the material, but fewer pitches dominate the reflection, resulting in lower intensity, although the image is the sharpest. However, at the equatorial and lower surface focus, the images appear blurry and diffused.

In orientation 4, the spectral behavior deviates significantly from the other orientations. Here, the shell opening is oriented toward the light source. Focusing on the top surface means focusing on the hole in the shell; the incident light partially transmits through the opening without interacting efficiently with the helical structure. As a result, the top-focus measurement yields the lowest reflectance among all conditions. This is consistent with the corresponding microscope image, which appears out of focus, suggesting that the focal plane does not intersect a meaningful part of the shell. In this specific orientation, highest reflectance occurs only when the focus is on the bottom surface, where the incoming light hits the actual material for the first time. Thus, for orientation 4, the “bottom focus” effectively corresponds to the same type of material interaction as the “top focus” in other orientations.

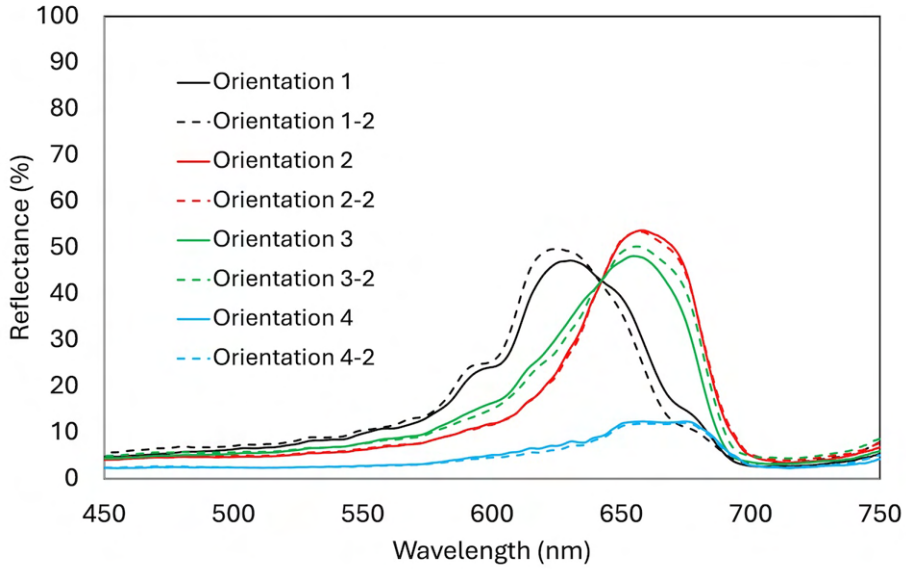

Figure 4.14: Reflection spectra of a single R-CSR measured at equatorial focus over two full turns. Fully drawn lines represents the first round and dashed lines are for second round.

In a separate angular rotation experiment, I rotated the same shell continuously over two full turns while keeping it at equatorial focus, and collected the reflection spectra at each 90° to check the consistency for the same orientation. Figure 4.14 shows these reflection spectra of a single R-CSR during two full 360° rotations. The fully drawn lines correspond to the first rotation cycle, while the dashed lines represent the second. The nearly identical spectral profiles across both cycles confirm the reproducibility of the reflection behavior and the rotational symmetry of the shell's response when viewed at equatorial focus.

4.4 Camouflaging and revealing graphical information based on selective polarization of d-CSRs

The optical characterization of d-CSRs demonstrated their ability to produce highly saturated retroreflective colors across the visible spectrum, from blue to red, even without requiring a refractive index matching binder. Leveraging this enhanced and tunable optical response, I

explored the potential use of d-CSRs for information encoding through optical camouflage. I created patterns on backgrounds that closely matched the reflection color of the d-CSRs, making them appear visually unobtrusive under ambient lighting conditions. Figure 4.15 demonstrates an example: a pattern spelling ”CSR” letters on a green plastic file binder prepared using G-d-CSRs. I designed a 3D-printed stencil to define the letters, and locally deposited G-d-CSRs using a plastic pipette. I captured photos in Figure4.15 using a DSLR camera (Canon EOS 77D), (a) under ambient light without any polarizer, as well as through (b) a left-handed (LH) and (c) a right-handed (RH) circular polarizers by manually placing them in front of a DSLR camera lens. I opted for a DSLR camera rather than our custom-built imaging setups to demonsrate how the pattern appears to the naked eye. Our dedicated imaging systems are designed to separate left- and right-handed channels for applying the background subtraction, but they do not show the unprocessed scene as an observer would experience it. Under ambient lighting without any polarizers (Figure 4.15a), the pattern visually blends into the background and is nearly invisible to the naked eye. However, when viewed through circular polarizers, the pattern becomes clearly distinguishable (Figure 4.15b-c).

The d-CSRs used in this demonstration have a left-handed cholesteric helix, which selectively reflects LH circularly polarized (LHCP) light. When the sample viewed through a RH circular polarizer, opposite to the helix’s handedness, the Bragg reflection is effectively suppressed and the ”CSR” letters appears dark due to the strong absorption from the infused Sudan Black dye, enhancing contrast between the two polarization states. In contrast, when the same sample is viewed through an LH circular polarizer, the Bragg-reflected LHCP light from the cholesteric structure is transmitted through the polarizer and reaches the detector or eye. The perceived brightness enhancement through LH polarizer is not due to the increased reflection of d-CSRs, but only to the effective filtering of reflected LHCP light. Since the background does not exhibit the same selective reflection, it appears dimmer. As a result, the ”CSR” letters appear brighter than the background, even though their absolute reflectance has not increased. This is a contrast illusion caused by polarization filtering: only the reflected light with the matching handedness is transmitted, enhancing visibility [88].

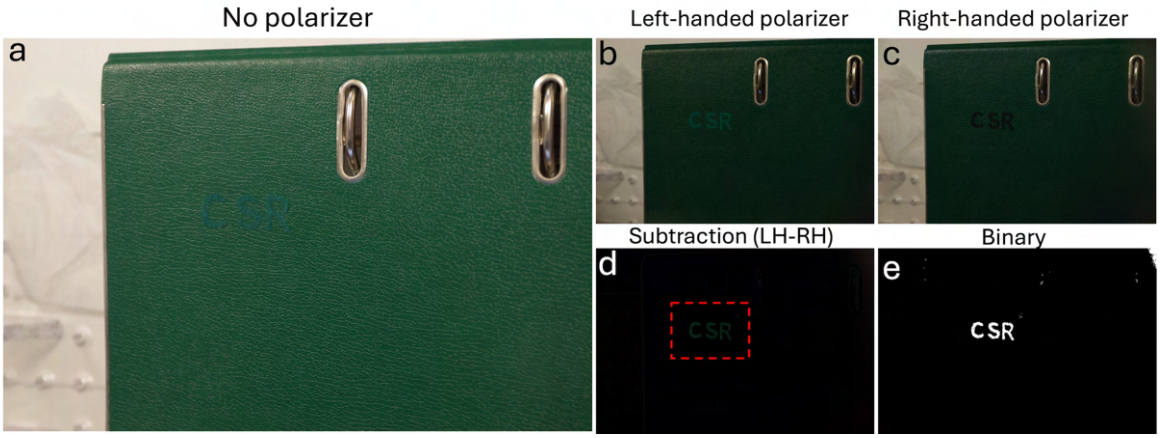

Figure 4.15: CSR letters patterned by using d-CSRs (λ_0=560 nm CSRs) infused by 2mg/mL dye-in-acetone solution on the surface of a green color file binder. Photographs taken under the office lighting, through (a) without any polarizer, (b) with left-handed circular polarizer, and (c) with right-handed circular polarizer. The background is removed by subtracting (b) from (c), as shown in (d). In (e) the green channel has been turned a binary image for maximum possible contrast. The subtraction of images and thresholding performed using Fiji ImageJ, an open source image analysis software.

The combination of the selective reflection of circularly polarized light from the cholesteric helix and the strong absorption of black dye provides a powerful contrast mechanism for detection based on selective polarization. Subtracting the RH channel image (Figure 4.15b) from the LH channel image (Figure 4.15c) effectively removes the background and isolates the reflection from the three letters (Figure 4.15d). Converting this subtracted image to a binary image, i.e. black and white, further enhances the contrast of the encoded information (Figure 4.15e). While this demonstration highlights the potential of d-CSRs for polarization-based information encoding and camouflage, one significant limitation of the system remains: the d-CSRs are dispersed in air and not embedded in any binder, making the marker they define mechanically fragile. Without a fixing medium, the particles are prone to displacement or damage through even mild handling or surface contact, which compromises the durability and reliability of the patterned information.

To address this issue and improve the mechanical durability of the d-CSR patterns without compromising their optical properties, I applied a protective matte clear coat using a com-

mercially available spray varnish (TRISTARcolor Professional Clear Varnish Spray, Matte Finish). This product is weatherproof, UV-resistant, and non-fading, making it suitable for outdoor or long-term applications. I sprayed the coating over the d-CSR pattern following the manufacturer's instructions. First, I cleaned the substrate (surface) with ethanol and left to dry completely. I then prepared two-dimensional circular patches using B-, G-, and R-d-CSRs on a black plastic substrate, as in two horizontal identical rows (Figure 4.16). To test the effectiveness of a protective coating, I masked the lower row. Once ethanol from the CSR deposition had fully evaporated, I sprayed the clear coat only to the upper row of the sample from a distance of approximately 30 cm in a well-ventilated area. I applied an initial coat and let it dry for at least 30 min before I applied three more layers, waiting 60 min between each layer to dry before subsequent application. I collected photos of the patterned surface under three different lighting conditions to evaluate any changes in optical response due to the coating. A key question was whether the circular polarization of the retroreflection would be affected by the transparent layer. Figure 4.16b confirms that the coated samples maintained the same polarization-selective reflection behavior as the uncoated ones, indicating that the clearcoat did not interfere with the optical properties of the d-CSRs. Equally important was assessing the mechanical stability of the pattern after coating. To test this, I applied pressure and lateral rubbing motions using a gloved finger over the coated patches. The particles remained firmly in place, demonstrating successful immobilization without the need for an additional binder. This result is highly promising, as the clearcoat not only provides mechanical stability but also successfully preserves the retroreflective and polarization-selective properties of the d-CSRs while significantly reducing unwanted specular (mirror-like) reflection. This simple post-processing step offers a scalable and practical route toward durable, real-world implementations of d-CSR-based information encoding.

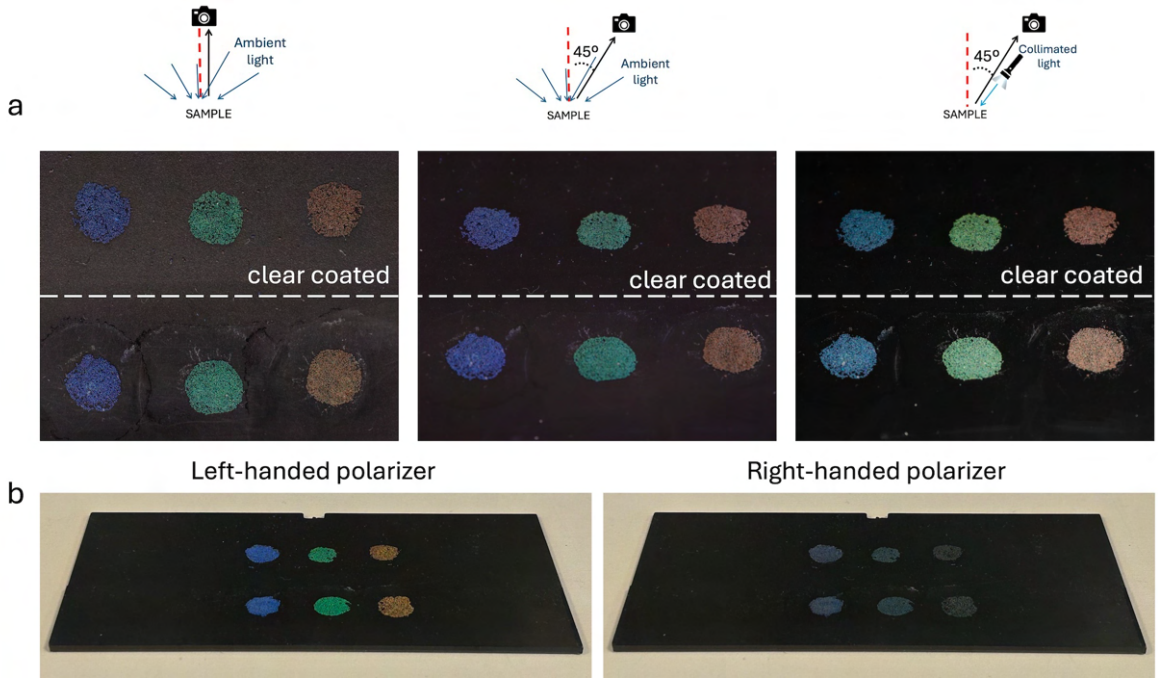

Figure 4.16: Macroscopic images of B-, G-, and R-d-CSR patches prepared in two identical horizontal rows on a black plastic substrate to evaluate the effect of a protective spray coating. All d-CSRs used here were prepared by infusing shells with a 2 mg/mL Sudan Black dye in acetone solutions. The lower row was masked, while the upper row was spray coated with a transparent matte coat (TRISTARcolor Professional Clear Varnish Spray). (a) Photographs were taken using a DSLR camera (Canon EOS 77D) under three lighting conditions: (left) diffused illumination at normal incidence (0°), (middle) diffused illumination at 45°, and (right) collimated illumination at 45°. (b) Corresponding images of the same sample captured using a mobile phone-based time-sequential dual-polarization imaging setup (previously described in Section 3.4.2): (left) through left-handed and (right) through right-handed circular polarizers to demonstrate polarization-selective visibility of clear-coated patches.

Encouraged by the promising results, Jan and I conducted an outdoor experiment to explore the potential of d-CSR patterns for real-world deployment. I prepared an ArUco fiducial marker (ID 0) using G-d-CSRs deposited onto a green plastic folder. I created the pattern using a 3D-printed stencil, following the masking technique I applied for the sample in Figure 4.15, then fixed the marker pattern in place with the transparent clearcoat layer. To assess the marker's visibility and robustness in a natural setting, we placed it outdoors on campus, among green plants, along with two other samples: jewel beetles and the NOA-based CSR marker. Using the phone-based time-sequential dual-polarization imaging setup, we

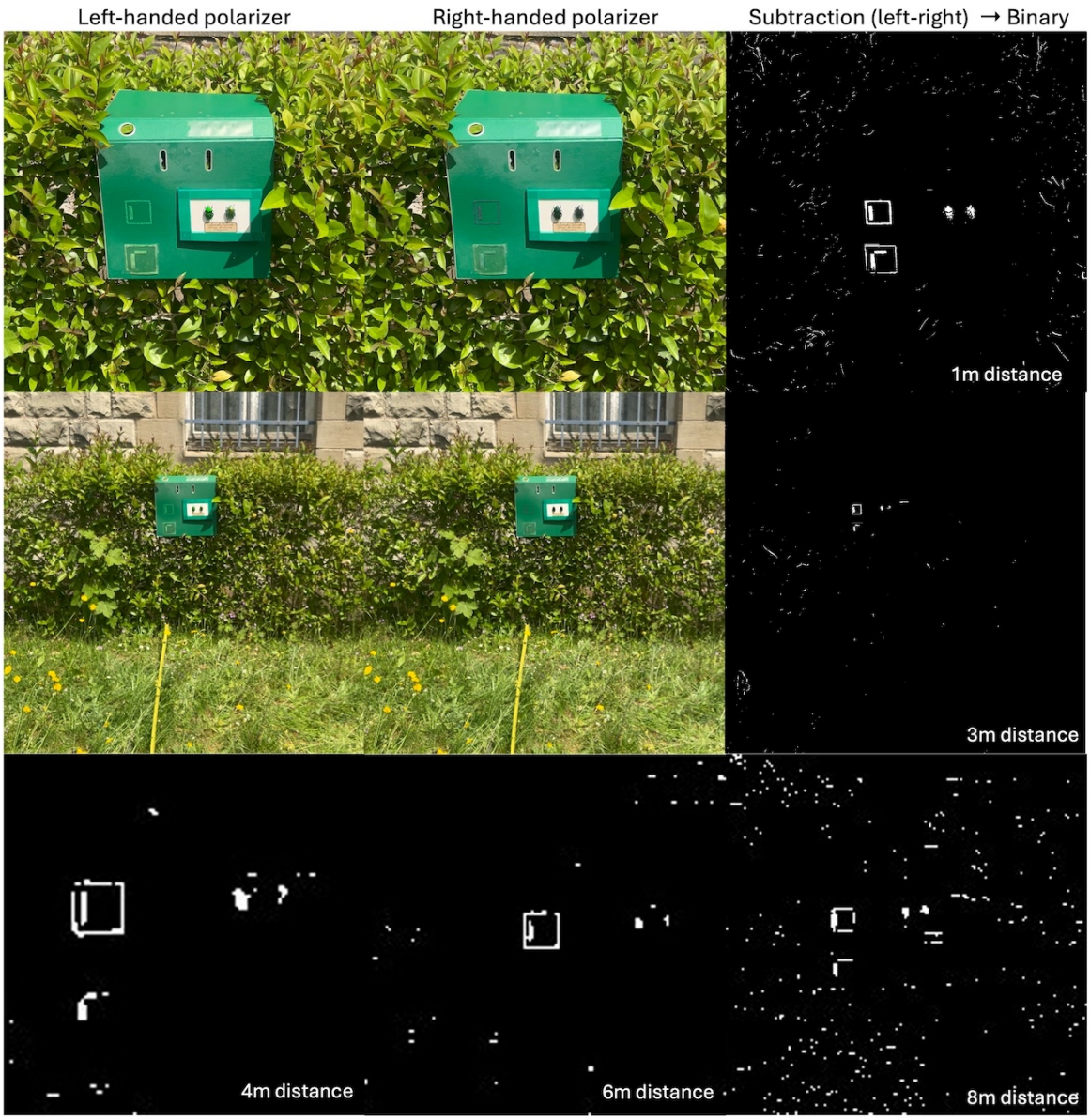

Figure 4.17: Comparison of long-range visibility of a G-d-CSR-marker, G-CSR-marker and two jewel beetles in an outdoor scene using a mobile phone-based time-sequential dual-polarization imaging setup. Images were captured through left-handed and right-handed circular polarizers at increasing distances. The top two rows show the LH, RH, and subtraction images, at 1m and 3m. The bottom rows display only the subtraction images (zoomed-in versions) at 4m, 6m, and 8m distances.

collected videos and still images over increasing distances. Figure 4.17 shows screenshots extracted from a video, in that we stopped every 1 meter and captured images through both LH and RH circular polarizers while continuously switching the voltage on and off to change the polarization state. The corresponding binary left-right subtraction images demonstrates how the selective retroreflection of the d-CSR marker allows it to be clearly distinguished from the complex background.

These preliminary results are highly encouraging: the optical response of the d-CSR marker outperforms that of the beetles, and exceeds the visibility of the standard CSR marker. While the current stencil-based method is effective, future improvements could be to apply an adhesive layer in the desired pattern on a target substrate, spray d-CSRs over the glue, and finally fix the pattern with a protective transparent coating. This would pave the way for more refined and scalable fiducial marker production.

By combining d-CSRs of different retroreflection wavelengths, it is possible to generate not only vivid spectral hues but also custom, non-spectral colors [78]. The fact that they can be easily arranged into arbitrary patterns, enabling flexible optical encoding on a variety of surfaces. Looking ahead, we envision expanding this strategy by developing cellulose-based d-CSRs [36, 37], incorporating carbon black as a robust and non-toxic broadband absorber. Such an approach would offer an environmentally friendly and long-term stable alternative to conventional colorants that goes beyond today's unsustainable dyes and pigments.

Chapter 5

Measuring the Anisotropic Refractive Indices of Polymerized Liquid Crystal Films

In this chapter, I present a simple and accurate experimental procedure for determining the anisotropic refractive indices of polymerized liquid crystal (LC) films by utilizing the polarization-dependent behavior of light reflected at Brewster's angle.

The motivation for designing and building this setup stems from the importance of refractive index matching between the CSRs and the surrounding medium when a fully transparent marker is desired. To minimize unwanted random scattering and to enhance the selective retroreflection signal, it is standard practice to embed CSRs in a binder with a refractive index as closely matched as possible to the average refractive index of the CLC phase [89, 75, 35, 78]. The reliable and easy method for measuring both the ordinary (n_o) and extraordinary (n_e) refractive indices of the polymer network becomes essential, especially when testing new binders or modifying the composition of the CSR formulation.

Traditionally, the Abbe refractometer is used to measure the refractive index of isotropic liquids. However, this technique relies on perfect optical contact between the sample and the prism of the refractometer. For polymerized films, air gaps can form between the prism

and the sample surface, resulting in inaccurate or misleading values. While, in principle, an Abbe refractometer could be modified to measure the ordinary and extraordinary refractive indices of anisotropic materials such as LCs by controlling the sample alignment and the polarization of the incident light, in practice, this is challenging. Standard instruments are not equipped for such control, and the confined geometry for the measurement makes uniform LC alignment difficult to achieve. Therefore, in most cases, the Abbe refractometer effectively provides only an average refractive index [90]. Ellipsometry is another established method for characterizing the optical properties of thin films. It involves analyzing the change in polarization state of light upon reflection to extract information such as the refractive indices and film thickness. While powerful and precise, ellipsometry requires complex data fitting based on detailed multilayer optical models which makes the analysis even harder for thicker or non-uniform samples. Indeed, ellipsometry is most effective for thin films in the nanometer range, whereas the LC polymer films studied in this work are typically much thicker, i.e. $\approx$ 10-20 μm.

Given these constraints, I sought a simpler and more accessible method to characterize LC polymers with different shapes and thicknesses. Brewster's angle-based measurement offers a suitable alternative. It is based on the well-known Fresnel equations and involves measuring the reflected intensity of p-polarized light as a function of the angle of incidence. By fitting experimental reflectance data with the Fresnel model, one can extract the refractive index of the material. The method shares theoretical roots with ellipsometry but is far simpler in practice. Brewster Angle Microscopy (BAM) is one example where this principle is applied to image thin films at the Brewster angle, allowing the study of thickness and surface topography. In contrast to full ellipsometry, the Brewster angle approach does not require complex modeling or precise control over film thickness and can be implemented with basic optical components [91].

In the following sections, I describe the theoretical background of the Brewster angle method, the design of the experimental setup, and the calibration procedure. I then demonstrate the measurements performed using a polymerized nematic LC film.

5.1 The principle of using Brewster's angle for the refractive index measurements

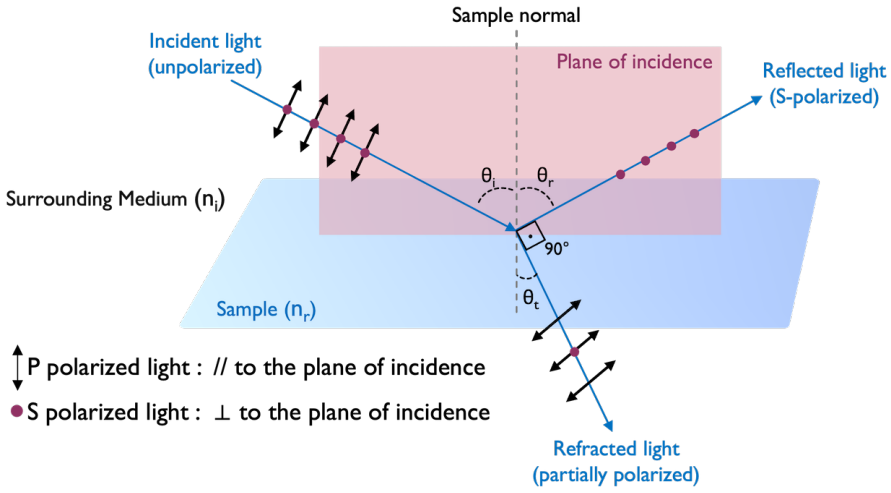

Figure 5.1: Schematic illustration of the polarization of light that is incident on an surface at Brewster's angle.

Brewster's angle is a fundamental optical phenomenon that provides a simple and effective way for estimating the refractive index of transparent isotropic materials. When unpolarized light strikes the interface between two media, such as air and glass, at a specific angle—known as Brewster's angle—the reflected light is perfectly s-polarized (perpendicular to the plane of incidence) while the reflectance of the p-polarized component (parallel to the plane of incidence) is zero, and that light is fully refracted. Figure5.1 schematically illustrates the polarization of light that hits a sample surface at Brewster's angle, θ_B.

Moreover, at this angle of incidence, the reflected and the refracted beams are perpendicular to each other (θ_t= $90 - \theta_r$). As we know from the law of reflection that the angle of incidence (θ_i) is equal to the angle of reflection (θ_r), we can rearrange Snell's law (equation 2.5) at Brewster's angle as follows:

$$n_i \cdot \sin\theta_B = n_r \cdot (90 - \sin\theta_B) \tag{5.1}$$

where n_i is the refractive index of the incident medium (typically air, $n_i \approx 1$), n_r is the refractive index of the sample, θ_B is the Brewster's angle. This condition allows for the determination of the refractive index of a material using the following expression known as Brewster's law:

$$tan\theta_B = n_r/n_i \tag{5.2}$$

To determine Brewster's angle experimentally, one can monitor the intensity of reflected light as a function of the angle of incidence. This can be achieved either by directing p-polarized light onto the sample or by isolating the p-polarized component of the light reflected from the sample using a polarizer. As the angle of incidence is gradually adjusted, the intensity of the reflected beam reaches a minimum (ideally zero) at Brewster's angle [92, 93]. For angles near normal incidence and at very high incidence angles, the reflected intensities of both p- and s-polarization components become nearly equal. However, their behavior differs at intermediate angles. The angular dependence of reflectance for each polarization component is described by Fresnel's equations. The equation for the p-polarized component is as follows:

$$R_p = \left| \frac{n_1 \cos\theta_t - n_2 \cos\theta_i}{n_1 \cos\theta_t + n_2 \cos\theta_i} \right|^2 = \left| \frac{n_1 \sqrt{1 - \left(\frac{n_1}{n_2}\sin\theta_i\right)^2} - n_2 \cos\theta_i}{n_1 \sqrt{1 - \left(\frac{n_1}{n_2}\sin\theta_i\right)^2} + n_2 \cos\theta_i} \right|^2 \tag{5.3}$$

where R_p is the reflectance of p-polarized light, θ_i and θ_t are the angles of incidence and refraction, and n_1 and n_2 are the refractive indices of the incident and transmission media.

In the scope of this thesis, the same principle is applied to anisotropic materials, such as liquid crystal films. Due to their directional optical properties, the reflectance minimum, i.e. the apparent Brewster angle, depends on the orientation of the optic axis relative to the incoming light. By systematically aligning the LC film in different orientations with respect to the polarization direction of the incident beam, we can obtain the anisotropic refractive indices, n_o and n_e.

When the optic axis is perpendicular to the plane of incidence, the light experiences the

ordinary refractive index, n_o, and Snell's law can be used to derive the Brewster angle as described above. However, when the optic axis lies in the plane of incidence (i.e., the film is rotated so the director (optic axis) is parallel to the incidence plane), the light interacts with the extraordinary refractive index, n_e. In this case, the standard Snell's law approach no longer applies, and the so-called "pseudo-Brewster angle" technique must be used [94, 95]. At the pseudo-Brewster angle, the reflectance of p-polarized light again reaches a minimum, and from this, n_e can be derived using more advanced expressions from anisotropic optics theory as follows:

$$R_{pp} = \left(\frac{n_o n_e \cos(\theta) - \sqrt{n_o^2 - \sin^2(\theta)}}{n_o n_e \cos(\theta) + \sqrt{n_o^2 - \sin^2(\theta)}} \right)^2 \tag{5.4}$$

Together, measuring both Brewster and pseudo-Brewster angles enables us to determine both n_o and n_e of polymerized LC films.

5.2 Design, construction and testing of the automated set-up for measuring refractive index using the Brewster angle

Many people contributed to the development of this experimental setup in different ways, and I am deeply grateful for their support. First of all, I would like to thank Dr. Ricardo Rojas-Aedo for his assistance in designing the non-automatic initial version of the experimental setup. I am also thankful to Claudia Kieffer, a B.Sc. student in the ESMP group under my supervision from September to June 2023, for collecting the initial measurements using polymerized nematic liquid crystal (LC) films. I am particularly grateful to Rebecca Warga for her dedicated efforts in automating the setup during her internship in the ESMP group and to our technician Robert Himelrick for his assistance in improving the design for 3D printing. Finally, I extend my sincere thanks to Dr. Alejandro Ibarra for further enhancing the automation and performance of Brewster's Angle setup, ultimately helping to realize the final, fully functional version.

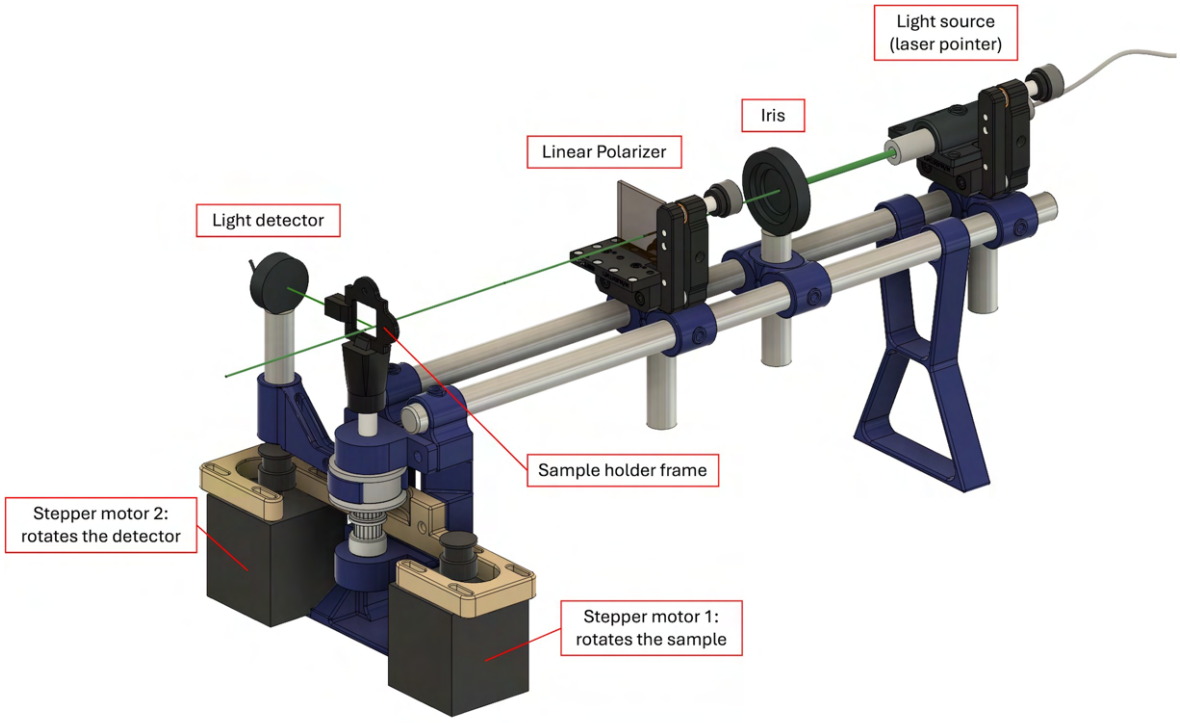

Figure 5.2: CAD design of the automated setup for measuring the Brewster angle.

Description of the set-up

Figure 5.2 shows the CAD model of our experimental setup built for measuring Brewster's angle. The system comprises optical components for light manipulation and mechanical elements for precise rotational motion control. The main optical elements are a diode laser of 530 nm wavelength as the light source, a polarizing beam splitter (PBS) cube, and a photodiode power sensor. An iris diaphragm is positioned before the PBS cube to reduce the beam size, ensuring that a well-defined, focused spot eventually hits the sample surface. The PBS cube then separates the incident beam into two orthogonally polarized beams. The transmitted beam is directed toward the sample, and its reflected intensity is measured at various angles of incidence using the photodiode sensor. All optical components (the light source, iris, and PBS) are mounted on two parallel horizontal metal rods that serve as a modular base, allowing flexible placement and rearrangement of components along the beam path as needed. While the distances between components are not critical for our

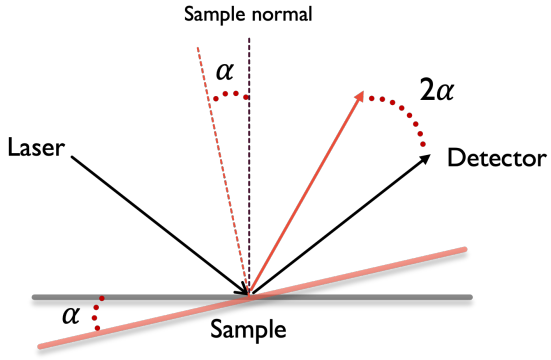

Figure 5.3: The angular diagram in the plane of incidence for our setup. If the sample rotates clockwise by an angle of α relative to the incident light, the light detector must rotate clockwise by an angle of 2α according to the law of reflection in order to detect the reflected light.

application, careful alignment is essential: each element is positioned to ensure that the laser beam travels in a straight line, without angular deviation, hitting all optical elements cleanly and ultimately striking the middle of the sample. The sample is fixed in a custom-designed holder mounted on a rotating axle. This holder consists of two frame pieces, each embedded with magnets that securely sandwich the sample between them, keeping it flat and aligned perpendicular to the propagation direction of laser beam. At the base of the axle, an angle sensor is attached to track the sample's rotational position throughout the experiment. The stepper motors drive the mechanical rotation: one rotates the sample, while the other rotates the light detector. To continuously capture the reflected beam, the detector must rotate twice the angle of the sample, as illustrated in Figure 5.3.

This continuous synchronized motion is achieved by a custom Python-based control program that communicates with an Arduino microcontroller. The Python interface handles user interaction and real-time motor coordination via a graphical user interface (GUI), while the Arduino runs a C++ program that executes the motor movements. Together, the two systems ensure synchronized and smooth operation during measurements. After each run, both motors can be reset to their initial "zero" positions. In this default state, the sample's angle of incidence is zero; however, due to mechanical constraints in the setup, the detector is positioned at approximately 20° relative to the sample normal. This offset is not a problem

because the rotation of the sample can be tracked by the angle sensor mounted under the axle. The angle sensor accurately determines the true angle at which the reflected beam is first captured. This point is taken as the effective starting position for the experiment. Thus, we first move the sample to the starting angle and then run the experiment for synchronized rotation with the light detector. During measurements, the software continuously records and logs the time, the angle of incidence, and the intensity of reflected light. This data is used to determine the Brewster angle, from which the refractive index of the sample can be calculated.

Testing the accuracy of the setup by using an isotropic sample with a known refractive index

Before applying the setup to nematic LC films, it was necessary to validate its accuracy by measuring the refractive index of a well-characterized, isotropic material. I thus first calibrated the reflected light measurements by using a piece of borosilicate glass. I performed measurements by rotating the sample and collecting reflectance data over an incident angle range of 30° to 70°, repeating the procedure three times for the same sample to assess repeatability. At each recorded angle, the detector recorded the reflected intensity of the p-polarized light.

To determine the reflectance R_p as a function of incidence angle, the measured power was normalized to the laser beam spot size hitting the sample to obtain irradiance values. To calculate R_p, the irradiance of the reflected beam was divided by the reference beam irradiance. The reference measurement was taken by removing the sample and positioning the detector perpendicular (90°) to the plane of incidence, to capture the incoming light. Using the measured R_p versus angle of incidence data, I plotted the reflectance curve to identify the Brewster angle, the angle at which R_p reached its minimum as shown in Figure 5.4. I then fit the experimental data to the Fresnel equation for p-polarized light using the software Pro Fit 7 (see the code in the Appendix). Initially, the fitting was carried out by assuming that the angular offset parameter was zero. Under this assumption, the fitted refractive index

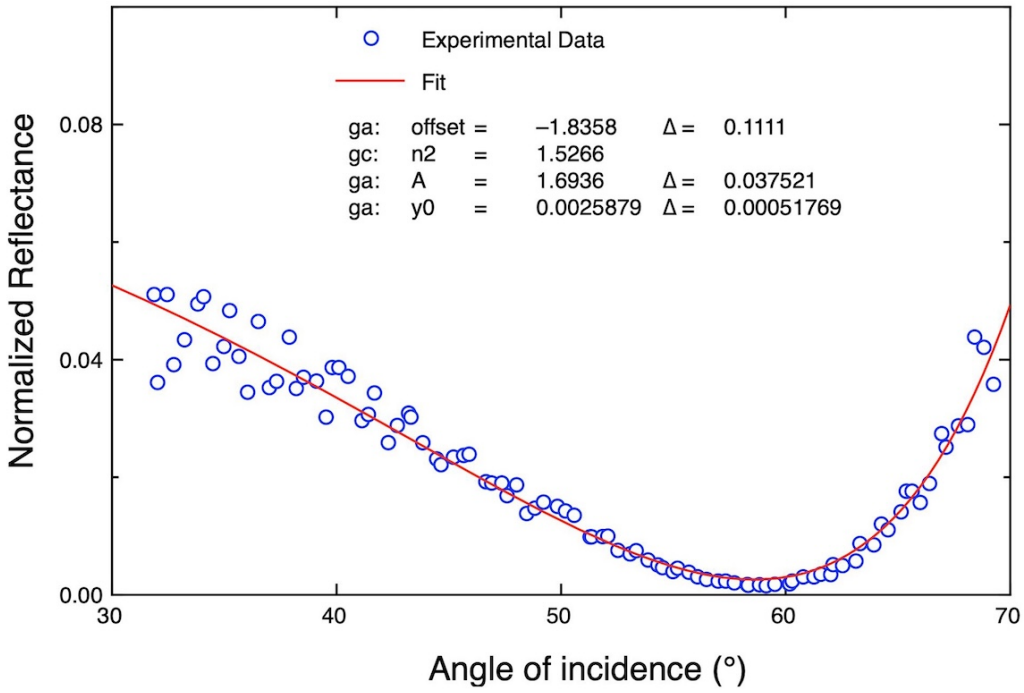

Figure 5.4: Calibration measurement using a borosilicate glass. Experimental data (blue circles) represent the measured p-polarized reflectance as a function of incidence angle. The red line corresponds to a Fresnel function for p-polarized light (equation 5.3) fitted to the data to determine the angular offset in the setup using the known value $n = 1.5266$ for the borosilicate glass [96].

value shifted from the known literature value of $n = 1.5266$ to $n = 1.6603$ for borosilicate glass [96].

This discrepancy was attributed to the first manual calibration of the angle sensor aligned with the sample's rotation axis. To determine the deviation of angle values, I fixed the refractive index at the literature value and reintroduced the angular offset as a free fitting parameter within the Python code implemented in Pro Fit 7 (see the code in the Appendix). The fitting then revealed an angular offset of approximately –1.8°, as shown in Figure 5.4. This correction was subsequently applied to all further measurements to ensure accurate angle calibration.

It is worth emphasizing that it is essential to perform such a reference measurement using

a sample of known refractive index (such as borosilicate glass) before every new measurement session. This ensures that any mechanical or alignment-related offset in angle determination can be corrected for, thereby improving the accuracy and reliability of refractive index measurements for unknown samples.

5.3 Measurement of n_o and n_e of polymerized nematic liquid crystal films

To determine the anisotropic refractive indices of polymerized nematic LC films, measurements were performed in two orthogonal sample orientations to separately calculate the ordinary (n_o) and the extreme extraordinary ($n_e^{max} = n_{||}$) refractive indices. These orientations correspond to different alignments of the optic axis with respect to the plane of incidence.

In the first configuration, the optic axis of the film was aligned perpendicular to the plane of incidence. In this orientation, incident p-polarized light interacts solely with the ordinary refractive index of the film because the optical axis lies entirely out of the incidence plane. Since the ordinary ray obeys Snell's law, the Brewster angle method can be applied directly to extract n_o analogous to the approach used for isotropic materials.

Using the previously determined angular offset obtained from the borosilicate glass calibration, the measured reflectance data was fit to the Fresnel equation for p-polarized light. Figure 5.5 shows the experimental data and corresponding fit based on equation 5.3. The Brewster angle, corresponding to the reflectance minimum, was extracted from this fit (see the code in the Appendix), yielding an ordinary refractive index of $n_o = 1.439 \pm 0.003$.

To determine the maximum extraordinary refractive index $n_{||}$ the same film was rotated by 90°, such that the optic axis now lay within the plane of incidence. In this configuration, the incident p-polarized light interacts with the extraordinary refractive index of the material. However, due to the anisotropic nature of the material, the extraordinary ray does not follow Snell's law in the usual form, because the angle between the light polarization and optic axis varies as we are rotating the sample during the experiment, the value of n_e changes,

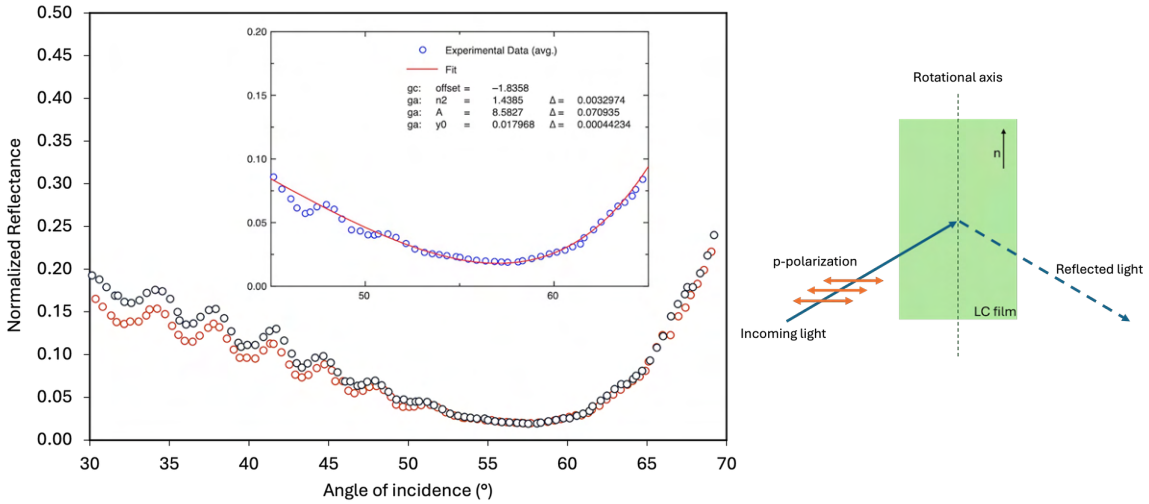

Figure 5.5: Experimental measurements and fitting for determining the ordinary refractive index n_o of a polymerized nematic LC film. The plot shows two independent measurement runs (data points represented by black and orange colored circles) of p-polarized reflectance as a function of incidence angle, with the optic axis oriented perpendicular to the plane of incidence. The inset displays the data fitting (red line) based on the Fresnel equation 5.3 for p-polarized light, applied to the average of the two runs (blue circles). A schematic illustration on the right shows the measurement geometry of the LC film, with the optic axis aligned perpendicular relative to the incident light's polarization and the plane of incidence.

between the maximum $n_e = n_{||}$ if the light beam hits the film along the film normal, and the minimum $n_e = n_o = n_\perp$ for the (hypothetical) extreme case that light would enter along the film plane, thus along the optic axis. For all intermediate angles, which are the practical measuring angles, we get an intermediate value for n_e, continuously varying with measuring angle. Consequently, the simple way of establishing a refractive index via the Brewster angle cannot be applied.

Instead, the pseudo-Brewster angle method was used, which involves analyzing the reflectance minimum under p-polarized illumination and fitting the data using expressions derived from anisotropic optics and ellipsometry theory [95]. Specifically, the reflectance behavior was modeled using equation 5.4, which is valid for planar-uniaxial media where the optic axis lies in the plane of incidence. The same angular offset determined from the glass calibration was again applied to correct the incidence angle readings. During the fitting pro-

cess, the previously determined value of $n_o = 1.439 \pm 0.003$ was held constant, as the same film was used in both measurements. From the reflectance minimum in this new orientation and fitting with the anisotropic model (see the code in the Appendix), the extraordinary refractive index was obtained as $n_e = 1.64 \pm 0.02$. Figure 5.6 shows the experimental data and corresponding fit based on equation 5.4.

While this chapter represents an early step toward establishing a practical and accessible method for determining the anisotropic refractive indices of polymerized LC films, the preliminary results are already promising. The measured birefringence value is approximately 0.20 via Eq. 2.8, falling well within the expected range for nematic LC systems [67]. These findings are in good agreement with the birefringence value of 0.225±0.004 previously obtained using the Michel-Lévy chart method, as reported in the thesis of bachelor student Claudia I worked with, from films prepared with the same LC mixture. However, to establish

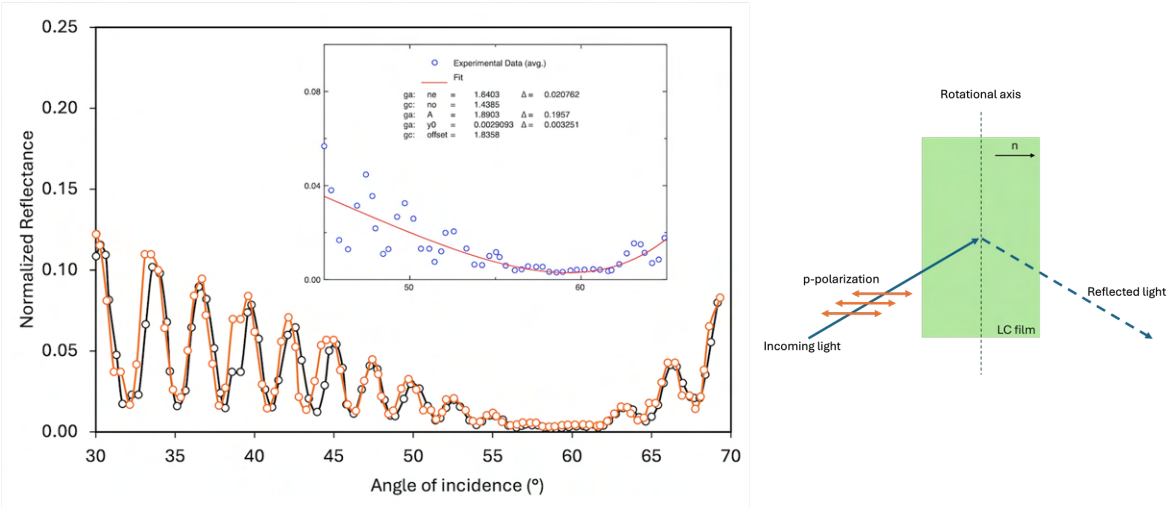

Figure 5.6: Experimental measurements and fitting for determining the extraordinary refractive index n_e of the polymerized nematic LC film. The plot presents two repeated measurement runs (black and orange circles) of reflected p-polarized light as a function of incidence angle, with the optic axis aligned parallel to the plane of incidence. The inset shows the data fitting (red line) based on the pseudo-Brewster angle expression in equation 5.4, applied to the average of two runs (blue circles). A schematic illustration on the right shows the measurement geometry of the LC film, with the optic axis aligned parallel with respect to the incident light's polarization and the plane of incidence.

statistical confidence and robustness of the method, further measurements with additional samples and repeated trials are necessary.

Both Figure 5.5 and Figure 5.6 show some fluctuations or “noise” in the data, which appear as zigzag patterns. These zigzags were also present when measuring the same sample in a second round, and the patterns from both measurements were in phase, supporting the idea that they may arise from thin-film interference. One possible explanation for these variations is interference caused by the free-standing nature of the polymerized LC film during the measurements. Since the film is relatively thin (typically around 10–20 μm) and suspended in air within a frame holder, reflections from the film surfaces can interfere, producing oscillations in the measured intensity. Although this interference introduces noise, it does not significantly affect the determination of the minimum reflectance corresponding to Brewster’s angle, as the overall trend remains clear.

At the same time, several practical improvements to the experimental setup are anticipated. Although the current sample holder uses a magnetic frame, placing the films without any wrinkles remains a challenge. The current solution is to place the film while it is still slightly wet and let it dry within the holder. While the initial design concept included the possibility of a rotatable frame, this feature was not implemented in the final version. In practice, incorporating additional side supports obstructed the optical path and limited the accessible angular range. Consequently, the measurement of n_o and n_e still requires manual removal and reorientation of the film between measurements, which introduces potential misalignment and variation in the illuminated region.

A significant improvement would be to redesign the sample holder to include a rotatable mechanism, enabling the sample to remain fixed in place while the entire holder is rotated. Importantly, the new design must also ensure that the light path remains unobstructed by any part of the holder’s structure. Such a modification would ensure that the same region of the film is probed in both orientations, and enhancing reproducibility. Photographs of the current experimental setup and sample holder are shown in Figure 5.7. These illustrate the overall geometry of the setup, the placement of the magnetic frame relative to the detector,

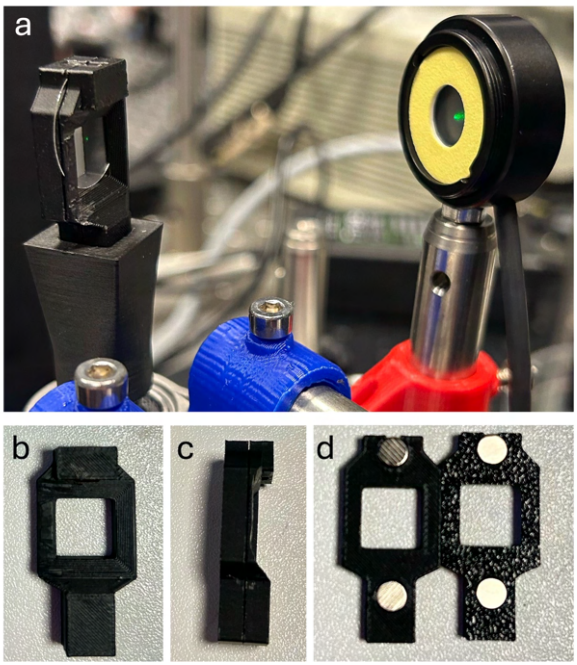

Figure 5.7: Photographs of the optical setup and magnetic film holder. (a) Close-up view of the measurement region showing the magnetic holder assembly with a reference glass sample between the two magnetic frames, positioned in front of the light detector. (b) Front view of the magnetic frames. (c) Side view of the magnetic frames. (d) Disassembled view showing the two magnetic frames separated.

and the detailed assembly of the two magnetic plates that clamp the film securely in place.

Despite current limitations, the results demonstrate that this method provides a reliable, accessible, and geometry-independent approach to characterizing birefringent materials. With continued improvements in alignment and automation, it can become a robust routine tool for characterizing LC-based solid films.

Chapter 6

Conclusion and Outlook

This thesis presented a comprehensive investigation into the optical properties, functional behavior, and practical applications of CSRs based on their polarization- and wavelength-selective optical properties. While the core of the work centers on fundamental optical phenomena in CLC systems, the broader motivation is to create functional, unobtrusive geometrical patterns that remain hidden under normal conditions but become detectable when proper imaging and illumination tools are used.

Throughout this work, we developed and improved various imaging and detection approaches to read out the CSR patterns. A major outcome was the creation of a compact, mobile phone–based dual-polarization imaging setup capable of capturing both left- and right-handed circularly polarized images with a single camera. This enabled fast, low-cost testing and detection of CSR-based tags and offered an accessible route to real-world deployment, especially outside laboratory conditions.

In parallel, a large portion of the study focused on understanding and improving the optical response of CSR particles themselves. Challenges in this domain included reducing random scattering from shell interfaces and maximizing the color intensity in order to increase the contrast for background subtraction based detection of CSR patterns. A central achievement of this thesis was the development of dye-infused CSRs (d-CSRs), created by incorporating a broadband-absorbing black dye into CSRs. These particles produce nearly

angle-independent, circularly polarized structural color across the visible range and offer significant contrast enhancements, without the need for an index-matching binder. A key technical milestone was the successful immobilization of d-CSR patterns using a transparent spray coat without sacrificing optical performance. This approach eliminated the need for index-matching binders and enabled mechanical durability without complicating the fabrication process. Field tests demonstrated the strong retroreflection and angular independence of these markers, which outperform biomimetic reflectors such as jewel beetles in side-by-side comparisons.

Looking forward, there are several directions in which the insights from d-CSRs can be further developed. One promising path is the shift toward more sustainable and biocompatible materials, particularly by replacing synthetic LCs with cellulose-based cholesteric systems. Similarly, replacing organic dyes with more stable pigments such as carbon black could further improve durability, particularly for outdoor use or long-term installations. Importantly, the d-CSR approach has significant potential for transferability into the near UV range. With suitable dyes (or perhaps combinations of dyes) which would allow high-intensity UV reflection without binder while also having high transparency, UV reflective CSR-based markers could be mounted on transparent surfaces like windows or glasses. These changes would bring the technology closer to practical deployment, especially in consumer products or outdoor conditions where durability and ecological impact are critical.

Speaking of the transferability of CSR-based patterns in the UV range, while NOA glue provides a near-perfect index-matching to CSRs, it has high absorption in the UV range, making UV-CSR markers appear pitch black when observed with a UV-only camera under UV illumination. This study also identified alternative formulations with required spectral transparency and good optical performance for polarization-sensitive detection. These findings pave the way for the incorporation of CSRs into durable optical coatings for UV range applications.

On the fabrication side, while replica printing for binder-based CSR-markers and stencil-based patterning for d-CSR patterns were successful, scalable deposition methods such as robot dispensing, spray coating, adhesive-assisted d-CSR deposition, followed by protective

coating, could significantly broaden the range of practical applications.

The final part of this thesis introduced a simple, low-cost, and effective method to determine the anisotropic refractive indices ($n_{\perp}$ and $n_{||}$) of polymerized LC films. By building a custom optical setup capable of detecting reflected intensity as a function of incidence angle, we enabled direct determination of $n_{\perp}$ and $n_{||}$ for arbitrarily thick polymerized LC films. Calibration with an isotropic glass sample validated the method's accuracy. This tool is also useful to support binder development for index-matching studies. Even though initial results were promising, further improvements are needed, such as improved stability and precise calibration for angle control.

The methods and tools introduced in this thesis, especially clear-coated patterns made of d-CSRs and dual-polarization imaging, form a solid foundation for further exploration. Continued work in this area can push CSR technologies from lab-scale experiments toward scalable, functional optical devices with real-world relevance in optics, materials science, robotics, and beyond.

Chapter 7

Materials and Methods

7.1 Microfluidic production of CSRs

Microfluidics device assembly and shell production

We produced CLC shells using a microfluidic device based on the concentric alignment of the tapered cylindrical glass capillaries nested into a square glass capillary, as first introduced by the Weitz group [56]. In the regular CSR production, we used a 5 wt.% isotropic aqueous solution of polyvinyl alcohol (PVA, M_w = 13–23 kg/mol, 87–89 % hydrolyzed, Sigma-Aldrich) as both the inner and outer phases. The middle CLC phase and the inner phase co-flow in the same direction, and the two phases meet a counter flow of the outer phase from the opposite side (See Figure 2.13).

The collected shells were kept in an incubator for annealing overnight at the production temperature. Solid shells were obtained by polymerizing the CLC phase under UV light for about 10 mins in a UV-curing chamber (Opsytec Dr. Gröbel Irradiation Chamber BSL-01), with the wavelengths 330-450 nm and light intensity of 66 mW/cm^2, followed by a series of washing steps: removing away the PVA outside the polymerized shells by washing with pure water, removing the unreacted components by washing with acetone and a final water wash to clean the inner PVA residues, as described by Geng et al. [35]. During the polymerization process, shells are bulging out at their thinnest part due to the polymerization-induced

shrinkage, which causes pressure on the incompressible inner liquid (See Figure 7.1). The polymerized shells cannot preserve their deformed shape and rupture during the acetone washing step upon swelling.

Materials and preparation of CLC mixtures

The CLC mixtures used in this study were composed of reactive mesogens, a chiral dopant, a diacrylate monomer, and a photoinitiator, as shown in Figure 7.2, along with their chemical structures and the mass ratios in the mixture. The reactive monomers included 4'-hex-5-enyloxy-biphenyl-4-carbonitrile (6OCB-1-ene, Synthon Chemicals) and 1,4-bis-[4-(3-acryloyloxypropyloxy)benzoyloxy]-2-methylbenzene (RM257, Wilshire Technologies). A chiral dopant (S/R 5011, HCCH, China) was used to obtain the cholesteric phase, and 2,2-dimethoxy-2-phenylacetophenone (Irg651, Sigma-Aldrich) served as the photoinitiator. To reduce the melting and clearing points as well as the viscosity of the base mixture, 1,6-hexanediol diacrylate (HDDA, Sigma-Aldrich) was added as a non-mesogenic reactive monomer.

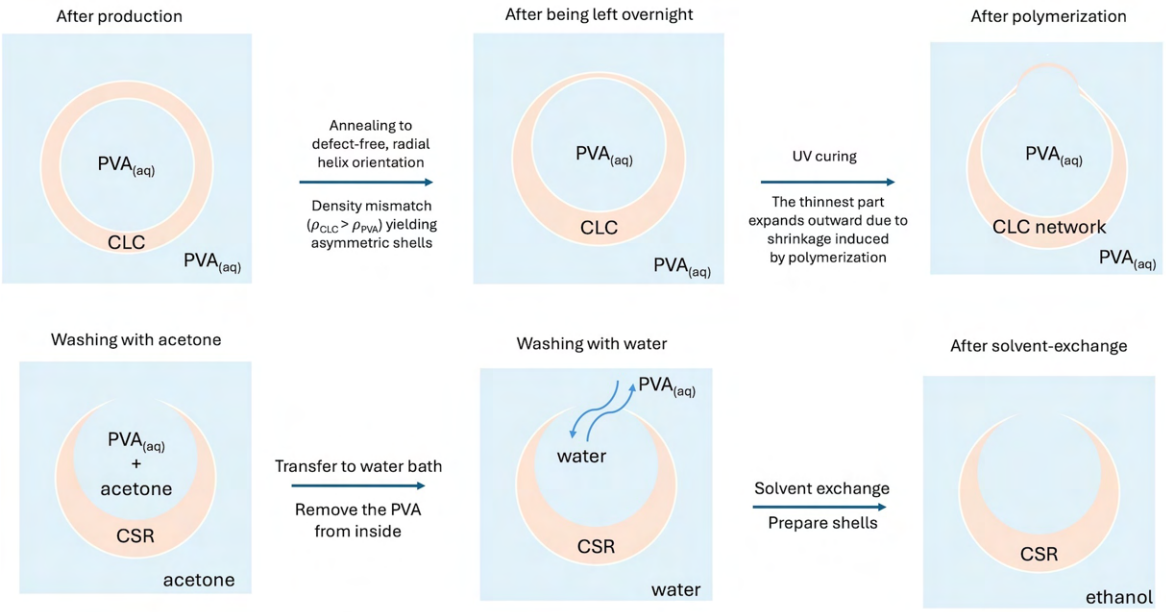

Figure 7.1: Schematic illustration of the process of making polymerized, punctured, and clean shells.

a

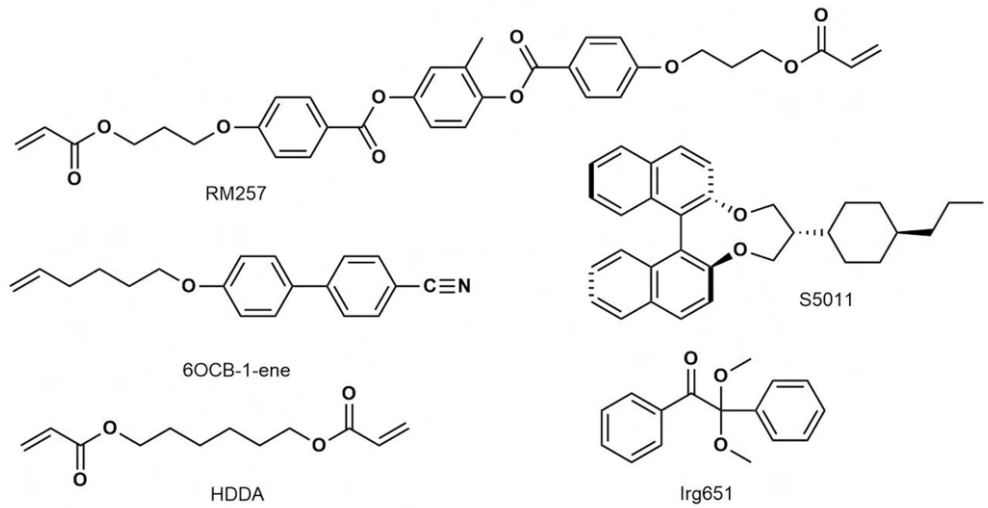

b

Retroreflection	HDDA	6OCB-1-ene	RM257	S5011	Irg651
Red	6	50.4	40	1.6	2
Orange	6	50.3	40	1.7	2
Green	6	50.2	40	1.8	2
Blue	6	50	40	2	2

Figure 7.2: a) Chemical structures of the materials used to prepare CLC mixture. b) Table of compositions of CLC mixtures. All numbers are wt.-%.

The retroreflection colors indicated in the table refer to the observed reflection colors after polymerization and post-washing steps were completed. For example, a representative shell precursor mixture (1 g total) consisted of 40 wt% RM257, 50 wt% 6OCB-1-ene, 6 wt% HDDA, 2 wt% S5011 (chiral dopant), and 2 wt% Irg651. This formulation was prepared by placing the components in a sealed glass vial and stirring magnetically at 400 rpm in a water bath at 60 ℃ for approximately 5-6 hours to achieve a homogeneous mixture. The concentration of the chiral dopant was adjusted depending on the target reflection wavelength, as detailed in Figure 7.2b.

Thermal characterization by differential scanning calorimetry (DSC, Mettler Toledo DSC823e, USA) and the viscosity measurements using a viscometer (RheoSensemicroVISC-m, USA) can be found in my colleague Xu Ma's paper [34].

7.2 Dye infusion process of CSRs and CLC films

Preparation of the CLC films

I first cut glass slides (Marienfeld GmbH) into pieces of approximately 1cm × 2cm using a glass cutter and pliers. I then cleaned the glass substrates with acetone and dried them using a compressed air gun to remove any dust particles. To prepare the planar-aligned sample cells, I coated the slides with 4 wt.$\%$ aqueous polyvinyl alcohol (PVA) solution using a spin coater (Laurell Technologies, WS-650-23). After the coating step, I gently rubbed the glass surface in the longitudinal direction using a clean velvet cloth to maintain uniform planar alignment. This rubbing direction defines the orientation of the director in the nematic phase. To assemble the cells, I sandwiched two PVA-coated glass slides such that the coated sides faced inward, with an offset of a few micrometers to create a gap for LC filling. I added either a small amount of UV-curable glue mixed with 10–20 μm polymer spacer beads or thin strips of kitchen stretch film as spacers at the corners. After aligning the slides, I cured the glue under UV light for a few seconds or used a paper clamp to make the cell structure stable.

I preheated the cell and the CLC mixture on a hotplate set to 45℃ for several minutes. Using a micropipette, I introduced approximately 10 μL of the mixture into the cell. The sample remained on the hotplate until the CLC filled the cell gap completely. To improve alignment, I placed the filled cell in an incubator set at 40℃ overnight. Following alignment, I polymerized the CLC in the above-mentioned UV-curing chamber (Opsytec Dr. Gröbel Irradiation Chamber BSL-01). As a final step, I gently detached the glass slides using a thin razor blade, similar to opening an oyster shell. To ease film removal, I occasionally immersed the cell in warm water to dissolve the PVA alignment layer. Once separated, I transferred the freestanding film onto a clean glass substrate and allowed it to dry fully. Finally, I measured the thickness of each film using a stylus profilometer (Bruker). The instrument employs a high-precision probe that senses vertical displacement as the tip moves and scans the surface.

Details of dye-infusion procedure

Dye solutions were prepared at five different concentrations: 0.5, 1, 2.5, 5, and 10 mg/ml Sudan Black B dye (Merck) dissolved in acetone. The mixtures were stirred on a hot plate at 45℃ and 400 rpm, followed by filtration through a 0.2 μm filter to remove any undissolved dye particles. Five separate batches of CSRs were prepared in ethanol. For the dye infusion, I prepared five different vials by adding 5 mL of the dye solution (the Sudan Black concentration varies, as described in detail below) to 0.5 mL of ethanol containing approximately 20,000 CSRs. I left the CSRs overnight in the dye solution on a roller mixer to carry out the infusion. The dye and acetone solution was removed using a pipette, ensuring that the CSRs, which settled at the bottom, were undisturbed. The shells were subsequently rinsed 3–4 times with ethanol (EtOH) to remove any dye precipitated to the outer surface. The washing process was continued until the ethanol appeared clear, indicating complete removal of excess dye. The dye-infused and ethanol-rinsed CSRs were deposited onto a glass slide using a pipette.

A similar procedure was applied to the polymerized CLC films. After polymerization and the standard washing steps to remove unreacted monomers, polymerized CLC films were immersed in the same dye solutions used for the CSRs and left overnight at room temperature. Following infusion, the films were carefully removed from the solution and rinsed several times with ethanol (3–4 times) to eliminate any dye adsorbed on the film surface. The rinsing was continued until the solvent remained clear, ensuring that only the dye incorporated within the polymer network remained. The infused films were then left to dry under ambient conditions before further optical characterization.

7.3 Optical Characterization and Measurements

Polarized Optical Microscopy (POM)

We performed optical characterizations by using a POM (Olympus BX51, Japan) equipped with an Olympus DP73 camera (Japan) and with 4x, 10x, 20x, and 50x objectives and

crossed polarizers. The bright field (BF) and polarized (PL) microscope images were collected in transmission and reflection modes.

UV-Vis Spectroscopy

The Ultrospec 2100 Pro UV-Visible spectrophotometer was used to collect absorption spectra of polymerized CLC films and solutions of Sudan Black and Tinuvin 328 dye in acetone.

The reflection spectra of CSR and d-CSR samples were measured using unpolarized white light and an Avantes AvaSpec-2048 spectrophotometer, which was connected directly to the microscope's eyepiece.

7.4 3D Printing and CAD Software

All 3D-printed components used in this thesis were designed using Autodesk Fusion 360, a computer-aided design (CAD) software.

I converted CAD files exported in `.stl` format into a sliced format (`.pm3` or `.sl1s`) using slicing software specific to the 3D printer in use. For the Anycubic Photon M3 printer (Anycubic, China), slicing and print preparation were performed using Photon Workshop. For the Prusa SL1S SPEED printer (Prusa Research, Czech Republic), slicing was done with PrusaSlicer software. For both printers, I followed the standard exposure settings recommended by the manufacturer.

I used commercial photopolymer resins, specifically Prusa's Prusament Resin Model series in Grass Green, Orange, and Transparent Clear colors. I followed the respective manufacturer's guidelines for post-processing steps, including isopropanol rinsing and UV post-curing, to ensure proper mechanical integrity and surface quality of the prints. In cases where I do polydimethylsiloxane (PDMS, Sylgard 184) casting in 3D-printed parts as molds, I applied a different post-processing protocol to prevent PDMS inhibition or adhesion. This specific post-treatment steps used for PDMS applications are described in detail in Chapter 4, Section 4.3.2.

Appendix

The Python code shown below is implemented in Pro Fit 7 for fitting the angle versus reflectance data using the Fresnel equation for p-polarized light 5.3. This code was used to determine the ordinary refractive index, n_o, from the Brewster angle measurement, assuming the optic axis of the film is aligned perpendicular to the plane of incidence.

```
## function FresnelRp "Fresnel Rp (with offset)"


import numpy as np # Required for math operations (sin, cos, sqrt).


def FresnelRp(x, n2, A=1.0, y0=0.0):


 # Inputs:
    #   x: Angle of incidence in degrees (from Pro Fit data column).
    #   n2: Refractive index of the material (fitted parameter).
    #   A: Amplitude scaling factor (default=1.0, accounts for beam size/light intensity).
    #   y0: Vertical offset (default=0.0, adjusts for non-zero minimum reflectance).

    theta_i = np.radians(x)  # Convert angle to radians
    sin_theta_i = np.sin(theta_i)
    cos_theta_i = np.cos(theta_i)

    # Snell's law and Fresnel calculation for p-polarized reflectance (Rp)
    sin_theta_t = sin_theta_i / n2
    if np.abs(sin_theta_t) > 1:
        return A * 1.0 + y0
# Total internal reflection (unlikely for n2 > 1). Return max reflectance (100%) if light cannot
transmit.

    cos_theta_t = np.sqrt(1 - sin_theta_t**2)
    numerator = n2 * cos_theta_i - cos_theta_t
    denominator = n2 * cos_theta_i + cos_theta_t
    Rp = (numerator / denominator)**2

    # Scale Rp by A and shift by y0 to match experimental data:
    return A * Rp + y0
```

The following Python code, also implemented in Pro Fit 7, to fit the angle versus reflectance data using the pseudo-Brewster angle method. This implementation follows the equation 5.4 as reported in [94, 95] and was used to determine the extraordinary refractive index, n_e, when the optic axis of the film is aligned parallel to the plane of incidence.

```
## function FresnelAnisoRp "Fresnel Rp for anisotropic sample"


import numpy as np  # Required for sin, cos, sqrt, radians


def FresnelAnisoRp(x, offset, ne, no=1.52, A=1.0, y0=0.0):
    # Inputs:
    #   x: Angle of incidence in degrees (from Pro Fit data column)
    #   offset: Angle offset (in degrees)
    #   ne: Extraordinary refractive index (fitted)
    #   no: Ordinary refractive index (optional)
    #   A: Amplitude scale factor (optional)
    #   y0: Vertical offset (optional)

    phi = np.radians(x + offset)  # Convert to radians


    sin_phi = np.sin(phi)
    cos_phi = np.cos(phi)

    # Calculate sqrt(no^2 - sin^2(phi)) term
    inside_sqrt = no**2 - sin_phi**2
    # Handle total internal reflection safely
    inside_sqrt = np.clip(inside_sqrt, 0, None)
    sqrt_term = np.sqrt(inside_sqrt)


    numerator = no * ne * cos_phi - sqrt_term
    denominator = no * ne * cos_phi + sqrt_term
    Rpp = (numerator / denominator)**2


    return A * Rpp + y0
```

References

[1] Joonil Cho and Yasuhiro Ishida. “Macroscopically oriented porous materials with periodic ordered structures: from zeolites and metal–organic frameworks to liquid-crystal-templated mesoporous materials”. In: *Advanced Materials* 29.25 (2017), p. 1605974.

[2] Peter J Collings and John W Goodby. *Introduction to liquid crystals: chemistry and physics*. CRC Press, 2019.

[3] Pierre-Gilles De Gennes and Jacques Prost. *The physics of liquid crystals*. Oxford: Clarendon Press, 1993.

[4] Martin Urbanski et al. “Liquid crystals in micron-scale droplets, shells and fibers”. In: *Journal of Physics: Condensed Matter* 29.13 (2017), p. 133003.

[5] Tim Sluckin, David Dunmur, and Horst Stegemeyer. *Crystals that flow: classic papers from the history of liquid crystals*. Taylor & Francis London, 2004.

[6] Ingo Dierking. *Textures of liquid crystals*. John Wiley & Sons, 2003.

[7] Jonathan V Selinger. *Introduction to the theory of soft matter: from ideal gases to liquid crystals*. Vol. 408. Springer, 2016.

[8] Devesh Mistry et al. “Coincident molecular auxeticity and negative order parameter in a liquid crystal elastomer”. In: *Nature communications* 9.1 (2018), p. 5095.

[9] VSR Jampani et al. “Liquid crystal elastomer shell actuators with negative order parameter”. In: *Science advances* 5.4 (2019), eaaw2476.

[10] Sven T Lagerwall. “On some important chapters in the history of liquid crystals”. In: *Liquid Crystals* 40.12 (2013), pp. 1698–1729.

[11] Christina Schütz et al. “From equilibrium liquid crystal formation and kinetic arrest to photonic bandgap films using suspensions of cellulose nanocrystals”. In: *Crystals* 10.3 (2020), p. 199.

[12] Danqing Liu and Dirk J Broer. “Liquid crystal polymer networks: preparation, properties, and applications of films with patterned molecular alignment”. In: *Langmuir* 30.45 (2014), pp. 13499–13509.

[13] Tatsuo Uchida and Hidehiro Seki. “Surface alignment of liquid crystals”. In: *Liquid Crystals—Applications And Uses: (Volume 3)*. World Scientific, 1992, pp. 1–63.

[14] Christian Decker and Aubrey D Jenkins. “Kinetic approach of oxygen inhibition in ultraviolet-and laser-induced polymerizations”. In: *Macromolecules* 18.6 (1985), pp. 1241–1244.

[15] Katia Studer et al. “Overcoming oxygen inhibition in UV-curing of acrylate coatings by carbon dioxide inerting, Part I”. In: *Progress in Organic Coatings* 48.1 (2003), pp. 92–100.

[16] Eugene Hecht. *Optics, Global Edition.* Harlow: Pearson, 2016.

[17] Justin Peatross and Michael Ware. *Physics of light and optics*. Brigham Young University, Department of Physics, Provo, UT 84602, 2015.

[18] Wikimedia Commons. *File:Electromagnetic-Spectrum.svg*. Online. Licensed under the Creative Commons Attribution-ShareAlike 4.0 International License (CC-BY-SA 4.0). 2023. URL: `https://commons.wikimedia.org/wiki/File:Electromagnetic-Spectrum.svg`.

[19] Avijit Lahiri. *Basic optics: principles and concepts*. Elsevier, 2016.

[20] David Dunmur and Kazuhisa Toriyama. “Optical Properties”. In: *Handbook of Liquid Crystals Set* (1998), pp. 215–230.

[21] Max Born and Emil Wolf. *Principles of optics: electromagnetic theory of propagation, interference and diffraction of light*. Seventh (expanded) anniversary edition. Cambridge University Press, 2019.

[22] SP Palto et al. “Photonics of liquid-crystal structures: A review”. In: *Crystallography Reports* 56.4 (2011), pp. 622–649.

[23] Christoph Fenzl, Thomas Hirsch, and Otto S Wolfbeis. “Photonic crystals for chemical sensing and biosensing”. In: *Angewandte Chemie International Edition* 53.13 (2014), pp. 3318–3335.

[24] Jiyu Sun, Bharat Bhushan, and Jin Tong. “Structural coloration in nature”. In: *Rsc Advances* 3.35 (2013), pp. 14862–14889.

[25] WD St John et al. “Bragg reflection from cholesteric liquid crystals”. In: *Physical Review E* 51.2 (1995), p. 1191.

[26] Corinne Binet, Michel Mitov, and Alain Boudet. “Bragg reflections in cholesteric liquid crystals: from selectivity to broadening and reciprocally”. In: *Molecular Crystals and Liquid Crystals Science and Technology. Section A. Molecular Crystals and Liquid Crystals* 339.1 (2000), pp. 111–123.

[27] Roy S Berns. *Billmeyer and Saltzman’s principles of color technology*. John Wiley & Sons, 2019.

[28] Gordon Zyla et al. “Generation of bioinspired structural colors via two-photon polymerization”. In: *Scientific reports* 7.1 (2017), p. 17622.

[29] Shinya Yoshioka and Shuichi Kinoshita. “Wavelength–selective and anisotropic light–diffusing scale on the wing of the Morpho butterfly”. In: *Proceedings of the Royal Society of London. Series B: Biological Sciences* 271.1539 (2004), pp. 581–587.

[30] S Kinoshita, Shinya Yoshioka, and J Miyazaki. “Physics of structural colors”. In: *Reports on Progress in Physics* 71.7 (2008), p. 076401.

[31] Rafael Maia et al. “Iridescent structural colour production in male blue-black grassquit feather barbules: the role of keratin and melanin”. In: *Journal of the Royal Society Interface* 6.suppl_2 (2009), S203–S211.

[32] Mohan Srinivasarao. “Nano-optics in the biological world: beetles, butterflies, birds, and moths”. In: *Chemical reviews* 99.7 (1999), pp. 1935–1962.

[33] Hakam Agha et al. “Unclonable human-invisible machine vision markers leveraging the omnidirectional chiral Bragg diffraction of cholesteric spherical reflectors”. In: *Light: Science & Applications* 11.1 (2022), p. 309.

[34] Xu Ma et al. “Tunable templating of photonic microparticles via liquid crystal order-guided adsorption of amphiphilic polymers in emulsions”. In: *Nature Communications* 15.1 (2024), p. 1404.

[35] Yong Geng, Rijeesh Kizhakidathazhath, and Jan PF Lagerwall. “Encoding hidden information onto surfaces using polymerized cholesteric spherical reflectors”. In: *Advanced functional materials* 31.21 (2021), p. 2100399.

[36] Yong Geng et al. “Cholesteric Spherical Reflectors with Tunable Color from Single-Domain Cellulose Nanocrystal Microshells”. In: *Advanced Materials* 36.8 (2024), p. 2305251.

[37] Richard M Parker et al. “Hierarchical self-assembly of cellulose nanocrystals in a confined geometry”. In: *ACS nano* 10.9 (2016), pp. 8443–8449.

[38] JungHyun Noh et al. “Tuneable multicoloured patterns from photonic cross-communication between cholesteric liquid crystal droplets”. In: *Journal of Materials Chemistry C* 2.5 (2014), pp. 806–810.

[39] Jing Fan et al. “Light-directing omnidirectional circularly polarized reflection from liquid-crystal droplets”. In: *Angewandte Chemie* 127.7 (2015), pp. 2188–2192.

[40] Yong Geng et al. “High-fidelity spherical cholesteric liquid crystal Bragg reflectors generating unclonable patterns for secure authentication”. In: *Scientific reports* 6.1 (2016), p. 26840.

[41] Yong Geng et al. “Elucidating the fine details of cholesteric liquid crystal shell reflection patterns”. In: *Liquid Crystals* 44.12-13 (2017), pp. 1948–1959.

[42] Mathew Schwartz et al. “Cholesteric liquid crystal shells as enabling material for information-rich design and architecture”. In: *Advanced Materials* 30.30 (2018), p. 1707382.

[43] Yong Geng et al. “Through the spherical looking-glass: asymmetry enables multicolored internal reflection in cholesteric liquid crystal shells”. In: *Advanced Optical Materials* 6.1 (2018), p. 1700923.

[44] Hyun-Gyu Lee, Sundas Munir, and Soo-Young Park. “Cholesteric liquid crystal droplets for biosensors”. In: *ACS applied materials & interfaces* 8.39 (2016), pp. 26407–26417.

[45] Ju-Hyun Jang and Soo-Young Park. “pH-responsive cholesteric liquid crystal double emulsion droplets prepared by microfluidics”. In: *Sensors and Actuators B: Chemical* 241 (2017), pp. 636–643.

[46] Lawrence W Honaker et al. “Designing biological microsensors with chiral nematic liquid crystal droplets”. In: *ACS applied materials & interfaces* 14.33 (2022), pp. 37316–37329.

[47] Mónica P Arenas, Hüseyin Demirci, and Gabriele Lenzini. “An analysis of cholesteric spherical reflector identifiers for object authenticity verification”. In: *Machine Learning and Knowledge Extraction* 4.1 (2022), pp. 222–239.

[48] Gabriele Lenzini et al. “Security in the shell: An optical physical unclonable function made of shells of cholesteric liquid crystals”. In: *2017 IEEE workshop on information forensics and security (WIFS)*. IEEE. 2017, pp. 1–6.

[49] Mathew Schwartz et al. “Linking physical objects to their digital twins via fiducial markers designed for invisibility to humans”. In: *Multifunctional Materials* 4.2 (2021), p. 022002.

[50] M Humar and I Muševič. “3D microlasers from self-assembled cholesteric liquid-crystal microdroplets”. In: *Optics express* 18.26 (2010), pp. 26995–27003.

[51] Rhutesh K Shah et al. “Designer emulsions using microfluidics”. In: *Materials Today* 11.4 (2008), pp. 18–27.

[52] J Cooper McDonald et al. “Fabrication of microfluidic systems in poly (dimethylsiloxane)”. In: *Electrophoresis: An International Journal* 21.1 (2000), pp. 27–40.

[53] George M Whitesides. “The origins and the future of microfluidics”. In: *nature* 442.7101 (2006), pp. 368–373.

[54] Jessamine Ng Lee, Cheolmin Park, and George M Whitesides. “Solvent compatibility of poly (dimethylsiloxane)-based microfluidic devices”. In: *Analytical chemistry* 75.23 (2003), pp. 6544–6554.

[55] Najiya Najiya et al. “Continuous flow microfluidic production of arbitrarily long tubular liquid crystal elastomer peristaltic pump actuators”. In: *Small* 19.13 (2023), p. 2204693.

[56] Andrew S Utada et al. “Monodisperse double emulsions generated from a microcapillary device”. In: *Science* 308.5721 (2005), pp. 537–541.

[57] Bharadwaj RK Mantha and Borja Garcia de Soto. “Investigating the fiducial marker network characteristics for autonomous mobile indoor robot navigation using ROS and gazebo”. In: *Journal of Construction Engineering and Management* 148.10 (2022), p. 04022115.

[58] Christopher Getschmann and Florian Echtler. “Seedmarkers: Embeddable markers for physical objects”. In: *Proceedings of the Fifteenth International Conference on Tangible, Embedded, and Embodied Interaction*. 2021, pp. 1–11.

[59] Naila Ayala et al. “Does fiducial marker visibility impact task performance and information processing in novice and low-time pilots?” In: *Computers & Graphics* 119 (2024), p. 103889.

[60] Mustafa Doga Dogan et al. “Infraredtags: Embedding invisible ar markers and barcodes using low-cost, infrared-based 3d printing and imaging tools”. In: *Proceedings of the 2022 CHI Conference on Human Factors in Computing Systems*. 2022, pp. 1–12.

[61] Mustafa Doga Dogan et al. “BrightMarker: 3D Printed Fluorescent Markers for Object Tracking”. In: *Proceedings of the 36th Annual ACM Symposium on User Interface Software and Technology*. 2023, pp. 1–13.

[62] Dingzeyu Li et al. “Aircode: Unobtrusive physical tags for digital fabrication”. In: *Proceedings of the 30th annual ACM symposium on user interface software and technology*. 2017, pp. 449–460.

[63] Tarun Kumar Agrawal, Christine Campagne, and Ludovic Koehl. “Development and characterisation of secured traceability tag for textile products by printing process”. In: *The International Journal of Advanced Manufacturing Technology* 101 (2019), pp. 2907–2922.

[64] Bastien Venzac et al. “PDMS curing inhibition on 3D-printed molds: why? Also, how to avoid it?” In: *Analytical chemistry* 93.19 (2021), pp. 7180–7187.

[65] Sajad Razavi Bazaz et al. “Rapid softlithography using 3D-printed molds”. In: *Advanced materials technologies* 4.10 (2019), p. 1900425.

[66] Kati Piironen et al. “Cell adhesion and proliferation on common 3D printing materials used in stereolithography of microfluidic devices”. In: *Lab on a Chip* 20.13 (2020), pp. 2372–2382.

[67] Werner Martienssen and Hans Warlimont. *Springer handbook of condensed matter and materials data*. Springer Science & Business Media, 2006.

[68] Vivek Sharma et al. “Structural origin of circularly polarized iridescence in jeweled beetles”. In: *science* 325.5939 (2009), pp. 449–451.

[69] Michel Mitov. “Cholesteric liquid crystals in living matter”. In: *Soft matter* 13.23 (2017), pp. 4176–4209.

[70] Michinari Kohri et al. “Bright structural color films independent of background prepared by the dip-coating of biomimetic melanin-like particles having polydopamine shell layers”. In: *Colloids and Surfaces A: Physicochemical and Engineering Aspects* 532 (2017), pp. 564–569.

[71] Wei Hong, Zhongke Yuan, and Xudong Chen. “Structural color materials for optical anticounterfeiting”. In: *Small* 16.16 (2020), p. 1907626.

[72] Miki Sakai, Takahiro Seki, and Yukikazu Takeoka. “Bioinspired color materials combining structural, dye, and background colors”. In: *Small* 14.30 (2018), p. 1800817.

[73] Lucas DC de Castro et al. “Sticky multicolor mechanochromic labels”. In: *ACS Applied Materials & Interfaces* 16.11 (2024), pp. 14144–14151.

[74] Alberto Belmonte et al. “Patterned full-color reflective coatings based on photonic cholesteric liquid-crystalline particles”. In: *ACS applied materials & interfaces* 11.15 (2019), pp. 14376–14382.

[75] E Beltran-Gracia and OL Parri. “A new twist on cholesteric films by using reactive mesogen particles”. In: *Journal of Materials Chemistry C* 3.43 (2015), pp. 11335–11340.

[76] Charles H Barty-King et al. “Mechanochromic, structurally colored, and edible hydrogels prepared from hydroxypropyl cellulose and gelatin”. In: *Advanced Materials* 33.37 (2021), p. 2102112.

[77] Cyan A Williams et al. “Inkjet printed photonic cellulose nanocrystal patterns”. In: *Advanced Materials* 36.1 (2024), p. 2307563.

[78] Hakam Agha et al. “Pixelating structural color with cholesteric spherical reflectors”. In: *Advanced Photonics Research* 4.4 (2023), p. 2200363.

[79] AC Neville and S Caveney. “Scarabaeid beetle exocuticle as an optical analogue of cholesteric liquid crystals”. In: *Biological Reviews* 44.4 (1969), pp. 531–562.

[80] Matthew D Shawkey and Liliana D’Alba. “Interactions between colour-producing mechanisms and their effects on the integumentary colour palette”. In: *Philosophical Transactions of the Royal Society B: Biological Sciences* 372.1724 (2017), p. 20160536.

[81] Kevin J McGraw and GE Hill. “Mechanics of melanin-based coloration”. In: *Bird coloration* 1 (2006), pp. 243–294.

[82] Michel Mitov. “Cholesteric liquid crystals with a broad light reflection band”. In: *Advanced Materials* 24.47 (2012), pp. 6260–6276.

[83] Hailin Cong et al. “Preparation of iridescent colloidal crystal coatings with variable structural colors”. In: *Optics Express* 21.15 (2013), pp. 17831–17838.

[84] Tarik Čamo et al. “Optical crack detection and assessment using cholesteric liquid crystal elastomers”. In: *Structural Health Monitoring* (2024), p. 14759217241296831.

[85] Yong Geng, Rijeesh Kizhakidathazhath, and Jan PF Lagerwall. “Robust cholesteric liquid crystal elastomer fibres for mechanochromic textiles”. In: *Nature Materials* 21.12 (2022), pp. 1441–1447.

[86] Alexandre Guimaraes de Almeida Barros et al. “Analyses of C. elegans fat metabolic pathways”. In: *Methods in cell biology*. Vol. 107. Elsevier, 2012, pp. 383–407.

[87] Abel GM Ferreira et al. “The viscosity of glycerol”. In: *The Journal of Chemical Thermodynamics* 113 (2017), pp. 162–182.

[88] Frank S Crawford. *Waves, Berkeley Physics Course Volume 3*. McGraw-Hill, 1968.

[89] Jun Li et al. “Refractive-index matching between liquid crystals and photopolymers”. In: *Journal of the Society for Information Display* 13.12 (2005), pp. 1017–1026.

[90] MS Zakerhamidi et al. “Refractive indices and order parameters of some tolane-based nematic liquid crystals”. In: *Journal of Molecular Liquids* 157.2-3 (2010), pp. 119–124.

[91] Bernard Desbat and Sabine Castano. “Brewster Angle Microscopy and Imaging Ellipsometry”. In: *Encyclopedia of Biophysics*. Ed. by Gordon C. K. Roberts. Berlin, Heidelberg: Springer Berlin Heidelberg, 2013, pp. 196–200.

[92] Cristian Bahrim and Wei-Tai Hsu. “Precise measurements of the refractive indices for dielectrics using an improved Brewster angle method”. In: *American Journal of Physics* 77.4 (2009), pp. 337–343.

[93] PJ Ouseph, Kevin Driver, and John Conklin. “Polarization of light by reflection and the Brewster angle”. In: *American Journal of Physics* 69.11 (2001), pp. 1166–1168.

[94] Rasheed MA Azzam and Nicholas Mitchell Bashara. *Ellipsometry and polarized light*. North-Holland Publishing Company, 1977.

[95] M Elshazly-Zaghloul and RMA Azzam. “Brewster and pseudo-Brewster angles of uniaxial crystal surfaces and their use for determination of optical properties”. In: *Journal of the Optical Society of America* 72.5 (1982), pp. 657–661.

[96] M. Polyanskiy. *SCHOTT D263 T eco – Refractive Index Data*. Online. Accessed: 2025-07-18. 2025. URL: https://refractiveindex.info/?shelf=specs&book=SCHOTT-misc&page=D263TECO.